SILVER (I) AND SILVER (I, III) OXIDE FORMATION VIA FEMTOSECOND LASER MICROMACHINING

DAVID GIRARD

Thesis submitted to the University of Ottawa
in partial fulfillment of the requirements for the
Master's degree in physics

Department of Physics
Faculty of Science
University of Ottawa

Abstract

Silver oxides have found numerous applications in catalysis, photocatalysis, data storage, energy storage and nanoparticle fabrication. Current methods of synthesising silver oxides include Pulsed Laser Deposition (PLD), oxygen plasma and ozone generator. Femtosecond laser micromachining has been used for precise surface texturing and to drive interesting chemical reactions on metals. In this thesis, silver (I) and silver (I, III) oxides are formed following femtosecond laser irradiation in ambient air. Numerous laser machining parameters, such as laser wavelength, pulse energy, number of shots and laser repetition rate are investigated to find sets of parameters that form each type of oxide. The laser machined silver is then studied using Raman spectroscopy to map the different silver oxides and to study their distribution on the machined surface. It is found that increasing the number of pulses and the pulse energy favours the formation of both AgO and Ag_2O. A mechanism of formation for AgO is then proposed and the decomposition of the oxides over time is studied.

Keywords: Silver oxide, Laser machining, Raman spectroscopy

Acknowledgements

First, I would like to thank my supervisor, Dr. Arnaud Weck, for his help, his guidance, and his feedback throughout the whole project. His suggestions and the discussions we have had during weekly meetings have helped me progress on my project in the right direction. He has also given me valuable feedback during the writing of this thesis.

I would also like to thank Dr. Pierre Berini for his help and suggestions that he would give during weekly meetings. His constructive feedback was immensely helpful during the course of this project.

I am also grateful for the tremendous help Dr. Jaspreet Walia has provided me in getting started on this project and for showing me how to use the Raman microscope. Without his guidance, learning the relevant concepts would have been much more difficult.

I want to thank Graham Killaire for showing me how to use the femtosecond laser. He has always been available to answer my questions and concerns regarding the laser.

I would like to thank Xitong Xie for being available in answering questions regarding laser machining in general, for his help in gathering data regarding laser fluence and for showing me how to use the chromatic point sensor.

I want to express my gratitude to Dr. Fabio Variola for letting me use his Raman microscope. This spectrometer has been a central part of the work presented here and has been extremely helpful in performing chemical analysis.

Lastly, I would like to thank my family and my friends for supporting me during my studies.

Contents

List of Figures

List of Tables

List of Abbreviations

BBO Barium Borate. x, xviii, 37, 40, 55, 56

CCD Charge-Coupled Device. viii, xi, 21, 22, 30, 41, 42, 89

EDS Energy-Dispersive Spectroscopy. iv, viii, ix, 2, 23, 24

FESEM Field Emission Scanning Electron Microscope. 41

FTIR Fourier-Transform Infrared. iv, ix, 2, 12, 23, 26, 28, 29, 30

HSFL High-Spatial Frequency LIPPS. 19

LEO Low-Earth Orbit. 1, 14, 15

LIPSS Laser-Induced Periodic Surface Structure. viii, 18, 19, 20, 46

LSFL Low-Spatial Frequency LIPPS. 18, 19, 46

PLD Pulsed Laser Deposition. ii, 7, 10, 11, 15, 20, 70, 93

PSO Position-Synchronised Output. 38

QCM Quartz Crystal Microbalance. 9, 23

SEM Scanning Electron Microscope. v, xi, 2, 23, 34, 41, 42, 44, 45, 46

SERS Surface-Enhanced Raman Spectroscopy/Scattering. 1, 14, 93

super-RENS Super-Resolution Near-Field Structure. 14

XPS X-Ray Photoelectron Spectroscopy. iv, ix, 2, 23, 25, 26, 27

XRD X-Ray Diffraction. 12

Yb:KGW Ytterbium Doped Potassium Gadolinum Tungstate. 37

Chapter 1

Introduction

Silver oxides have many applications, which make them interesting materials to study. They have been researched extensively for their applications, methods of synthesis as well as general properties. They can be formed by ultrafast laser ablation of silver, and the formation of silver oxides from this method is the main subject of this work. The number of pulses and pulse energy threshold should both control the types of silver oxide being formed by laser machining.

Silver oxides are commonly used in zinc-silver oxide button cell batteries that are typically used in small electronic devices. Their high energy density make them a good choice to create small batteries that can power devices such as watches. Silver oxides have been studied in the literature mainly for energy storage applications. They also have applications in optical data storage. There has been a few studies of silver nanoparticle formation from silver oxides, for which their plasmonic properties have interesting application such as Surface-Enhanced Raman Spectroscopy/Scattering (SERS). The mechanisms of silver oxide formation have also been studied in the context of Low-Earth Orbit (LEO) activities.

Silver ultrafast laser machining has been studied in the literature, however most publications on this subject focus on the morphological changes of the silver from laser machining and do not report any results regarding changes in the surface chemistry. One article by

Walia *et al.* shows the formation of nanotextured silver (I) oxide from femtosecond laser machining, along with rapid reaction of atmospheric carbon dioxide with the silver oxide [1]. The aim of this thesis is to expand on the work already done on femtosecond laser-machined silver and report on the types of silver oxides that are formed from ultrafast laser machining. The effects of laser parameters on silver oxide formation as well as the stability of the silver oxides are studied.

In Chapter 2, a review of the literature on silver oxides, ultrafast laser machining and some popular characterisation techniques for metal oxides is presented. The types of oxides (more particularly Ag_2O and AgO) are presented, their properties are discussed, and formation mechanisms are explained. The main fabrication techniques for silver oxides are then listed and summarised. Decomposition of silver oxides both in ambient environment and high temperature is summarised, then applications for both oxides are listed. The ultrafast laser machining section starts with a quick introduction to the fundamentals of ultrafast laser machining, then explains changes in morphology and the oxidation induced by the laser. The main characterisation techniques described in this chapter are Energy-Dispersive Spectroscopy (EDS), X-Ray Photoelectron Spectroscopy (XPS), Fourier-Transform Infrared (FTIR) and Raman spectroscopy. Finally, the main research objectives for this project and how they are related to the literature are presented.

In Chapter 3, the equipment and the methodology for every experiment conducted are explained. This includes the optical setup for laser machining, as well as a description of the silver samples and how they are prepared, the laser, the Raman spectroscopy setup, the Scanning Electron Microscope (SEM) and the optical microscope. The fabrication of a silver oxide sample using an oxygen plasma etcher is also briefly described.

In Chapter 4, results from laser machining of silver are presented. Laser dot matrices are used to find silver oxide formation thresholds and Raman scans show how oxides are distributed on each laser machined sample. The effects of pulse energy, number of pulses, laser wavelength, repetition rate and presence of oxides prior to laser machining are discussed.

The results are then summarised, and a mechanism of silver oxide formation is proposed.

In Chapter 5, the decomposition of the silver oxide over time and by a continuous wave laser is discussed. The timescale of decomposition of AgO, the formation of other silver corrosion products apart from oxides and the effect of the continuous wave laser needed to perform Raman spectroscopy are studied. The results are then summarised.

Chapter 6 concludes this work by summarising the methodology and the most important results. Future experiments are proposed and potential applications of silver oxides from femtosecond laser machining are listed.

Chapter 2

Literature Review

In this section, previous work regarding the various silver oxides is summarised and discussed. The physical properties of silver oxides, methods to fabricate them, their decomposition and their applications are brought up. Femtosecond laser machining and its relevant characteristics such as the morphological and chemical changes are described. Relevant characterisation techniques used to study metal oxides that often appear in literature are summarised. Finally, the main research objectives for this project are presented.

2.1 Silver Oxides

In this thesis, two types of oxides were detected after laser machining: Ag_2O and AgO. Their physical properties are highlighted in this section, as well as methods of fabrication found in the literature. Decomposition conditions reported are also discussed. Finally, a few of their current and potential applications are underlined.

2.1.1 Types of Oxides

In the literature, AgO is also commonly referred to as Ag_2O_2, Ag_4O_4, $Ag^{I}Ag^{III}O_2$, or $Ag_3O_2{\cdot}AgO_2$. This is because this silver oxide is in a mixed valence state and contains

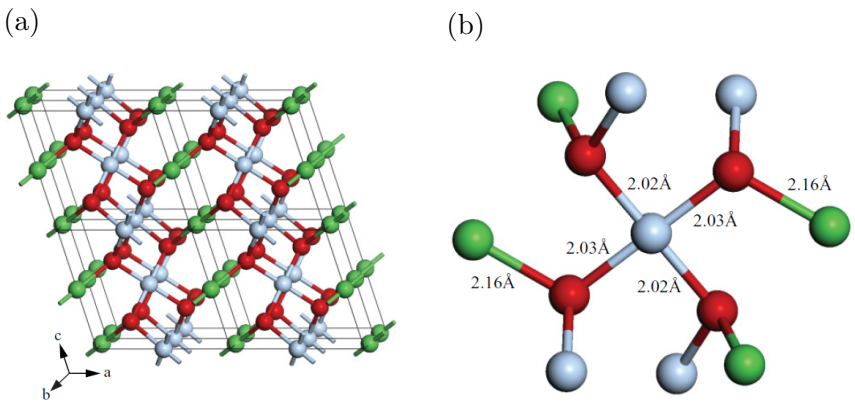

Figure 2.1: (a) Unit cell for AgO and (b) bond lengths and coordination environment of AgO, (c) Unit cell for Ag_2O and (d) bond lengths and coordination environment of Ag_2O. Green spheres are Ag(I) atoms, grey spheres are Ag(III) atoms and red spheres are oxygen atoms. Taken from [8].

chemically inequivalent Ag atoms [2–6]. There exists many more Ag compounds, such as Ag_2O, Ag_2O_3 and Ag_3O_4 [4, 7]. The focus here is on Ag_2O and AgO, which are commonly referred to as silver (I) oxide and silver (I,III) oxide, the numbers in bracket referring to the oxidation states of the silver atoms. These are the most commonly observed oxides, as they are the most stable ones. Figures 2.1 and 2.2 show the unit cell for AgO and Ag_2O respectively.

The oxidation state (total number of electrons missing from an atom for positive oxidation states) of the Ag atoms in Ag_2O is solely +1, while it is a mixed state of +1 and +3 in AgO. Both the Ag atoms in Ag_2O and the Ag^{I} atoms in AgO are linearly coordinated with oxygen, while the coordination geometry is square-planar with the Ag^{III} atoms [4–6, 9]. The Ag^{+} and Ag^{+3} ions make both Ag_2O and AgO diamagnetic [4, 5]. Ag_2O and AgO are both available commercially as powders; Ag_2O has a dark brown color and AgO has a dark grey color.

Studies on the formation and growth mechanisms of Ag_2O and AgO thin films show that oxidation of silver to silver (I, III) oxide occurs in two steps, silver (I) oxide being the intermediate step [10]. In fact, reaction of a silver sample with oxygen atoms (from an O_2 plasma or from ozone dissociation, for example) can form a silver oxide (AgO and Ag_2O) film on the surface of the Ag sample [10–12]. That silver oxide film can then crack and spall

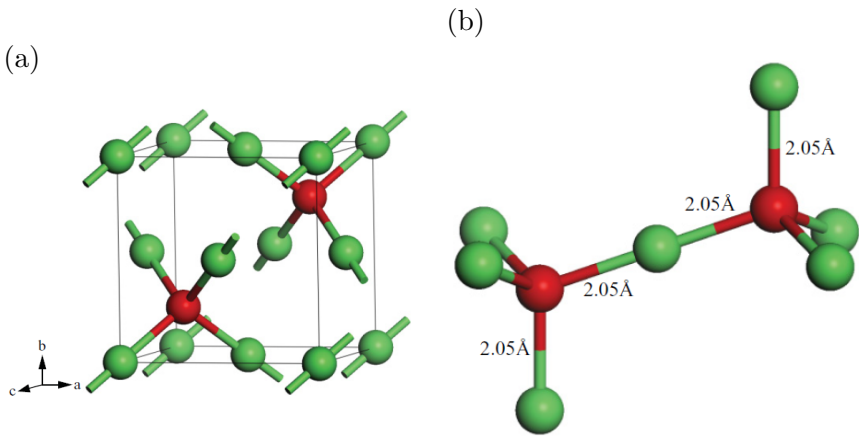

Figure 2.2: (a) Unit cell for Ag_2O and (b) bond lengths and coordination environment of Ag_2O. Green spheres are Ag(I) atoms and red spheres are oxygen atoms. Taken from [8].

as a result of a volume expansion during its formation. The AgO film formed in this process is porous [10, 13, 14]. Ag_2O that is slightly below the surface is formed from the diffusion of oxygen atoms through the surface oxide (AgO) layer [10]. The following reactions explain the Ag oxidation to Ag_2O and AgO from atomic oxygen [12, 15]:

$$2\,Ag_{(s)} + 2\,O \longrightarrow Ag_2O_{2(s)} \tag{2.1}$$

$$2\,Ag + O \longrightarrow Ag_2O \tag{2.2}$$

$$Ag_2O + O \longrightarrow 2\,AgO \tag{2.3}$$

Ozone gas also reacts with silver to produce silver oxides at room temperature, likely from the ozone dissociating into O_2 and atomic oxygen adsorbed on silver [11, 16]:

$$2\,Ag_{(s)} + O_{3(g)} \longrightarrow Ag_2O_{(s)} + O_{2(g)} \tag{2.4}$$

$$Ag_2O_{(s)} + O_{3(g)} \longrightarrow Ag^{I}Ag^{III}O_{2(s)} + O_{2(g)} \tag{2.5}$$

$$O_{3(g)} \longrightarrow O_{2(g)} + O_{(ads)} \tag{2.6}$$

2.1.2 Fabrication

Silver oxide has been manufactured via several methods, as found in the literature. While it has been synthesised by chemical reactions in the past [17–19], more attention will be given to methods in which ozone and atomic oxygen are involved, such as reactive sputtering, ozone gas flow, oxygen plasma treatment and Pulsed Laser Deposition (PLD). Depending on the fabrication technique, many parameters can be tuned to achieve the desired silver oxides with specific structure. Studies on these parameters as well as description of the oxides formed are discussed here.

Reactive Sputtering

For reactive sputtering, the main concept is very similar to regular sputtering, except that a mix between an inert gas (such as argon) and a reactive gas (such as oxygen) is used as the sputtering gas. This method of deposition is convenient for creating silver oxide thin films, since oxygen can be used as the reactive gas. During sputtering, high energy gas atoms or plasma eject atoms from a target. These atoms are then deposited on a substrate, creating a film, and the sputtering time can be adjusted to control the film thickness. Creating silver oxide thin films requires the reactive gas to be O_2 and the target to be pure silver. Argon and oxygen gas flow as well as sputtering power (power of the AC, DC or RF power supply) can be adjusted as needed.

Reactive sputtering has often been used, as reported in the literature to create silver oxide thin films [20–30]. Among the parameters that have been studied, increasing the ratio of O_2 to Ar turns the main oxide formed from purely Ag_2O to a mix between Ag_2O and AgO to purely AgO [20, 25]. Asgary & Esmaili showed that a low oxygen to argon ratio gives a mixed Ag/Ag_2O material and increasing the ratio yields a pure Ag_2O film [30]. The oxygen ratio determines the amount of oxygen atoms in the film, but it also has an effect on the film morphology (particle size and porosity) [30]. Sputtering power has also been shown to affect the film porosity, roughness and grain size [27–29]. The sputtering time may also be

increased to make the deposited silver oxide film thicker [27].

Reactive sputtering is an attractive technique for silver oxide fabrication because it allows great control over the oxidation state of the film as well as the oxide composition by adjusting oxygen flow rate. The morphology of the surface may also be finely tuned by adjusting the sputtering power as well as the gas flow rate, allowing for rougher and more porous films.

Ozone Generator

Ozone treatment of silver forms both Ag_2O and AgO. It is performed by flowing O_2 gas in an ozone generator, then the silver sample is exposed to the ozone formed by the generator. The resulting composition of the gas mixture may be adjusted, and the reaction with the silver sample may be set for a certain amount of time. This oxidation reaction is explained by equations 2.4 to 2.6.

In the literature, Ag_2O and AgO have successfully been grown from both silver powder and silver foil samples by ozone treatment [11, 16, 31]. Studies discuss the effect of temperature on the formation of both Ag_2O and AgO, and report formation of both oxides at temperatures below or equal to roughly 500 K when silver was exposed to ozone, Ag_2O exclusively at temperatures between 600 K and 775 K and no oxides at above 900 K [16, 31]. Waterhouse *et al.* describe the oxidation process of silver foil from ozone as following the two steps described in section 2.1.1 [11]. This oxidation process is illustrated in figure 2.3. The oxides were confirmed by various spectroscopic techniques. Waterhouse *et al.* also report the surface morphology affecting the rate of oxidation [11].

Ozone treatment of silver is a potential method to form Ag_2O and AgO. Reaction time has been shown to promote the formation of AgO, while still forming Ag_2O on bulk silver by means of cracking and flaking. The thickness of the silver oxide films is difficult to control because of this flaking, as well as the fact that ozone will only react with the material at the surface. The temperature of the treatment also plays a role because AgO and Ag_2O are thermodynamically stable at different temperatures, Ag_2O being more stable than AgO at

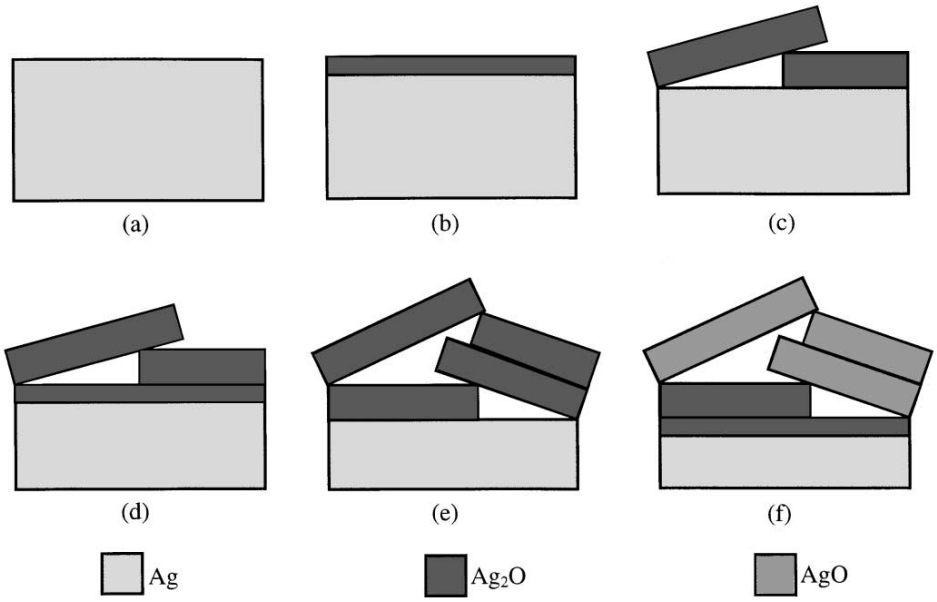

Figure 2.3: Formation of silver oxides from ozone. A silver foil (a) is exposed to an O_2-O_3 gas mixture, which oxidises Ag (b). Flaking of the oxide occurs from stresses caused by the volume change of the oxidation to Ag_2O (c), which exposes more silver to be oxidised (d). While the silver is oxidised and keeps flaking and cracking (e), surface layer Ag_2O further oxidises into AgO (f). Adapted with permission from reference [11] (the original paper has a mistake: the legend for AgO is coloured white instead of grey).

a high temperature. This will be discussed more thoroughly in section 2.1.3.

Oxygen Plasma

Oxygen plasma treatment of silver samples is another method of synthesising both Ag_2O and AgO. In this case, the atomic oxygen from the plasma oxidises the silver in a similar way as does ozone. The mechanisms of oxidation are also similar to the ones discussed for ozone.

In literature, oxygen plasma etching has been used to prepare silver oxide films from pure silver samples [3, 7, 12–15, 32, 33]. A few articles indicate the use of this method along with a Quartz Crystal Microbalance (QCM) to study the ratio of oxygen to silver after oxidation by measuring the change in the thin film's mass [3, 13, 14, 32, 33]. Oakes *et al.* have used a CO_2 laser to dissociate the O_2 to create oxygen plasma, which is then pulsed on the silver sample [33]. This allows the control of the oxygen atom speed by increasing or decreasing

the time between the O_2 pulses and the laser ionisation. Oakes *et al.* show that AgO was primarily formed, with the oxidation rate having no dependence on oxygen velocity from 8 to 12 km/s and no dependence on temperature from 273 to 385 K [33]. Zheludkevich *et al.* report only Ag_2O being formed at higher temperatures [12]. Bhan *et al.* report that increasing the atomic oxygen flux increases the rate of oxidation [15]. Articles using oxygen plasma for oxidation often focus on the kinetics and mechanisms of oxide formation [12–14, 32, 33]. It was found that the rate of oxidation is at first linear due to oxidation of the surface layer, but then decreases due to the oxidation being limited by the diffusion of O atoms through the oxide layer [12, 14, 33]. At high temperatures, this mechanism is no longer accurate [12]. This will be discussed further in section 2.1.3.

Oxygen plasma has been shown to form both Ag_2O and AgO. The thickness of the silver oxide film cannot be controlled as much as with other fabrication techniques. Like in ozone treatment, it has been reported that oxide films formed this way undergo cracking and flaking, which exposes more silver to be oxidised [15].

Pulsed Laser Deposition (PLD)

Pulsed Laser Deposition (PLD) combines the ablation capabilities of nanosecond pulsed lasers on a metal target along with their abilities to induce chemical changes in the air (such as the dissociation of oxygen). A silver target is irradiated by a nanosecond laser resulting in silver ablation and dissociation of the oxygen around the sample. This process is generally done in a vacuum chamber containing a controlled amount of oxygen. The ejected silver reacts with the ozone (formed from the reaction between oxygen molecules and dissociated oxygen atoms) and atomic oxygen to form silver oxides through reactions 2.1 to 2.6. The silver oxide then reaches the substrate in the chamber forming a silver oxide thin film. This method allows the tuning of many parameters such as the laser power, the gas composition in the chamber containing the target and the distance between the target and the substrate on which the oxide is to be deposited.

PLD has been used extensively in literature to deposit Ag_2O and AgO thin films on substrates in an oxygen-containing medium [34–40]. It has been shown that the oxygen pressure affects which oxide gets formed from pulsed laser deposition; a low oxygen pressure yields Ag_2O films and increasing the O_2 pressure increases the concentration of AgO in the deposited film [34, 36, 40]. The grain size of the deposited oxides may be modified by either the deposition temperature or the laser energy, and both these parameters increase grain size when increased [38, 39]. The distance between the target and the substrate along with the pressure may be adjusted to change the morphology of the deposited film. This affects the kinetic energy of the ablated material. A short distance (or low pressure) creates compact silver oxide with a columnar structure and a long distance (or a high pressure) creates a foamy silver oxide film [34, 35, 40]. It has also been shown that PLD is also able to create silver oxide films in air rather than pure oxygen [34, 35].

PLD is an attractive silver oxide fabrication technique because of the wide range of parameters that can be tuned to create precisely structured silver oxide films. The oxygen pressure may be adjusted to get Ag_2O, AgO, or a mix between the two. The temperature along with the laser power may be adjusted to control the grain size of the silver oxide film. The distance between the sample and the target can be increased or decreased, depending on whether a compact column-like structure or a foam-like structure is desired.

2.1.3 Decomposition

In this section, the thermodynamic stability of Ag_2O and AgO at various temperatures is discussed, along with some of the products of decomposition of both oxides. There are many experiments in the literature where silver oxide samples have been decomposed by annealing or even at ambient conditions.

Ag_2O is more thermodynamically stable than AgO. Decomposition of AgO into Ag_2O under ambient conditions has been reported in the literature [3, 13, 15]. The decomposition in air, at room conditions takes place over a few days typically [3, 13]. The temperature of

decomposition of AgO to Ag_2O is also much lower than the temperature of decomposition of Ag_2O to metallic silver. It has been observed via FTIR, Raman spectroscopy and X-Ray Diffraction (XRD) that the decomposition of AgO into Ag_2O would occur in the temperature range 373 K-473 K, that Ag_2O would completely transform back into metallic silver at 673 K, and that AgO decomposes into metallic silver via the Ag_2O intermediate via the following reactions [41]:

$$Ag^{I}Ag^{III}O_{2(s)} \xrightarrow{T > 373\,K} Ag_2O_{(s)} + 0.5\,O_{2(g)} \tag{2.7}$$

$$Ag_2O_{(s)} \xrightarrow{T > 623\,K} 2\,Ag_{(s)} + 0.5\,O_{2(g)} \tag{2.8}$$

Thermal decomposition of AgO into Ag_2O and Ag_2O into metallic silver has been studied as reported in more articles [24, 42–45]. Zheludkevich *et al.* discuss relevant reactions in the Ag-O system, including reaction 2.2 and the following two reactions [12]:

$$Ag_2O \longrightarrow 2\,Ag + \frac{1}{2}O_2 \tag{2.9}$$

$$Ag_2O + O \longrightarrow 2\,Ag + O_2 \tag{2.10}$$

The authors mention that as the temperature increases, the Gibbs energy of the reaction 2.2 increases, it decreases for reaction 2.9 and it stays constant for reaction 2.10, as shown in figure 2.4. Thus, there is a temperature where decomposition reactions occur faster than formation reactions, meaning the formation of Ag_2O stops. The mechanisms of formation are disturbed by the decomposition of silver oxides [12].

Smith & Brown also reported on the instability of AgO affecting the capacity of silver/zinc batteries. The capacity loss is caused by a reaction between AgO and metallic silver forming Ag_2O. The capacity loss when stored at room ambient temperature for long periods of time is insignificant but becomes more prevalent when stored at high temperature. The reaction is as follows [47]:

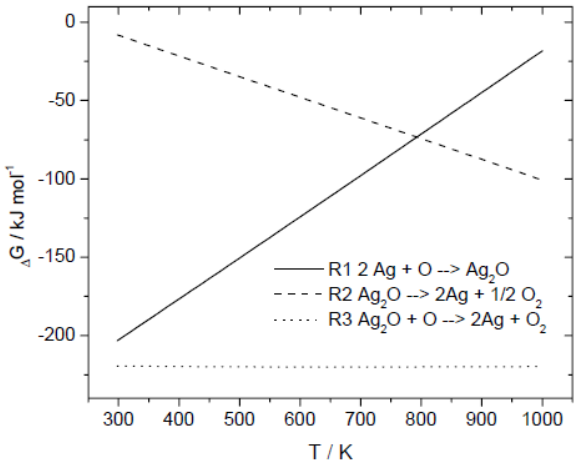

Figure 2.4: Gibbs energies with respect to temperature for reaction 2.2, 2.9 and 2.10. As temperature increases, decomposition reactions have smaller Gibbs energies than formation reactions, meaning the formation of Ag_2O stops. Taken from [46].

$$AgO + Ag \longrightarrow Ag_2O \tag{2.11}$$

Ag_2O forms silver carbonate in presence of carbon dioxide in ambient conditions [1, 44, 48]. The chemical reaction is as follows [1, 48]:

$$Ag_2O_{(s)} + CO_{2(g)} \longrightarrow Ag_2CO_{3(s)} \tag{2.12}$$

It was found that Ag_2O nano-textured surfaces from femtosecond laser machining silver (ablating the surface) was more reactive towards CO_2 in the atmosphere than film-like oxide. The laser machined area underwent rapid hydroxylation and the Ag_2O reacts with H_2O and CO_2 to form Ag_2CO_3 via the mechanism shown in figure 2.5 [1].

2.1.4 Applications of Silver Oxides

Silver oxides are extensively studied as indicates the literature, as they have many applications. Among these are applications in energy storage and capacitors, data storage, photocatalysis, antibacterial surfaces and the formation of silver nanoparticles, which are often

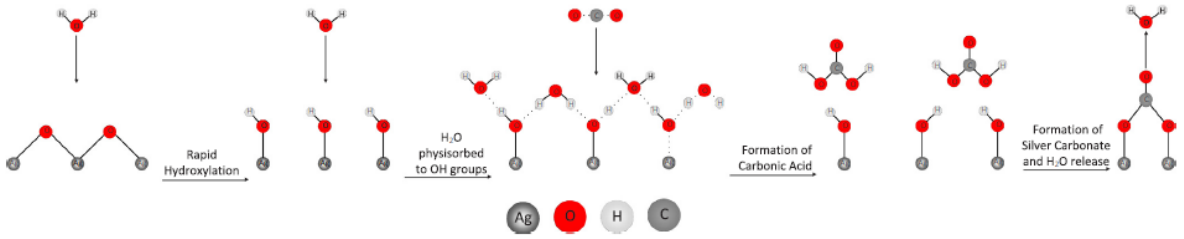

Figure 2.5: Mechanism of formation of Ag_2CO_3 in laser machined area. The nanotextured Ag_2O undergoes rapid hydroxylation. The hydroxylated surface forms hydrogen bonds with water vapor, which reacts with CO_2 to form carbonic acid. The carbonic acid then reacts with the hydroxylated surface to form Ag_2CO_3 and water. Taken from [1].

used in SERS and other plasmonic applications. The mechanisms of oxidation from atomic oxygen (section 2.1.2) has also been studied to better understand the oxidation on equipment in LEO.

AgO and Ag_2O have been extensively studied for energy storage purposes. Silver/zinc reserve batteries offer high energy and power density [47, 49]. Long-term storage is a problem since the AgO in those batteries may decompose into Ag_2O. There has been more research in silver-oxide based electrodes for rechargeable energy storage, which show promising results in charge/discharge rate [17]. Silver oxide thin films prepared by reactive sputtering have also been found to be promising for supercapacitor applications [27–29].

Silver oxides have been studied in the past for data storage applications, particularly for Super-Resolution Near-Field Structure (super-RENS) [20, 22, 24, 25]. Silver oxides are used as a mask layer for high-density optical data storage. The decomposition of silver oxide into metallic silver forms silver nanoparticles, for which there are strong near-field effects. This enables readout beyond the diffraction limit [24]. The silver oxide mask layer is protected by a protective layer. There has not been any recent progress on super-RENS using silver oxides. There are a few more articles describing the formation of silver nanoparticles from silver oxides, either by annealing [23] or by leaving the silver oxide in a H_2 and O_2 gas mixture [50]. Some work has been done with silver oxides regarding SERS [21, 37, 51]. Silver oxide thin films may be decomposed into silver nanoparticles via thermal annealing, which due to their plasmonic effects induce a strong enhancement in Raman scattering signals [21, 51].

Nanotextured Ag_2O has been proposed as a potential material for artificial photosynthesis. It reacts strongly with carbon dioxide in ambient air at ambient condition to create Ag_2CO_3, which has interesting possibilities for carbon capture and storage and photocatalytic reduction of CO_2. This material and surface morphology can be made in a single step by femtosecond laser machining [1].

It has been found that AgO formed by PLD presents interesting anti-bacterial properties towards gram-negative and gram-positive bacteria [34, 35]. This is the case since Ag ions with high oxidation number get released and react with the bacteria. It has also been shown that the high-valence silver oxide has superior anti-bacterial properties to nanostructured silver surfaces [34].

LEO activities have promoted the study of silver oxide formation via atomic oxygen [10, 12, 15, 33]. Silver is often used in spacecrafts, which must operate very high in the atmosphere. At high altitudes (>85 km), oxygen atoms are found in high concentrations. These atoms have a high capacity to oxidise the silver used in space equipment, which affects the mechanical strength and other properties [15]. The ability to treat silver with oxygen plasma in a laboratory environment allows the study of how equipment that contains silver might be affected by the high atomic oxygen concentration at high altitudes.

2.2 Ultrafast Laser-Matter Interaction

Femtosecond laser machining has a wide range of applications for surface texturing. The high pulse energy offered also presents interesting applications when chemically modifying surfaces. To understand why chemical reactions and certain morphology changes are taking place while laser machining silver, it is important to know what processes are taking place when laser machining metals, in general.

2.2.1 Fundamentals of Ultrafast Laser-Matter Interaction

Ultrafast lasers are pulsed lasers with a duration of a few picoseconds or less. Such a short pulse time presents unique properties when laser machining materials. During the laser machining of metals, the main components absorbing the laser light are the electrons. Electrons that are excited interact with non-excited electrons and an equilibrium is reached very quickly (in less than a picosecond). The lattice only gets heated up by collisions with the hot electrons, and this process, called electron-phonon relaxation, takes much longer than the time it takes the electrons to go to an excited state (or the time of the ultrafast laser pulse) [52, 53].

Each material has an ablation threshold, i.e., the laser fluence (deposited energy per unit area) at which material starts to be removed from the surface. The threshold for metals depend on the number of pulses, following this equation [54]:

$$F_{th}(N) = F_{th}(1)N^{S-1} \tag{2.13}$$

$F_{th}(N)$ is the ablation threshold for N pulses, $F_{th}(1)$ is the ablation threshold for a single pulse and S is the incubation coefficient. Incubation in metals denotes the fact that as laser pulses are applied on the material, its absorption behaviour will change. This change in absorption may be due to chemical or structural changes on the surface [55]. The dependency of number of pulses over the ablation threshold is explained by the accumulated stresses from the laser even with a fluence below the single-pulse ablation threshold [54]. This equation is only relevant up to a certain number of pulses since there is a limit on how low the laser fluence can be to affect the metal in any way. Figure 2.6 shows a least-squares fit of the threshold fluence with respect to the number of pulses. A lower limit of fluence is clearly reached beyond 200 pulses.

There are many mechanisms that drive the ablation process. For ultrafast lasers ablating metals, those are primarily spallation and phase explosion. Spallation happens at

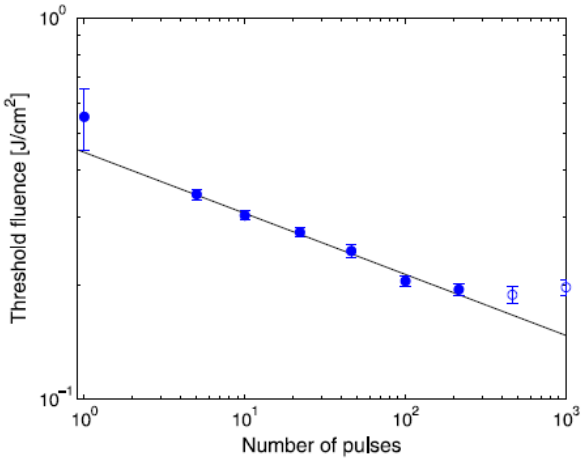

Figure 2.6: Least-squares fit (solid line) for ablation threshold fluence of tungsten with respect to number of pulses. A lower limit is reached beyond $N = 200$ pulses. Only the filled data points are used for fitting. The calculated incubation coefficient is 0.84 ± 0.01. Taken from [56].

relatively low fluence and is the result of random voids forming under the surface following the formation of stress waves from the fast energy deposition of the laser. When these voids achieve percolation, the surface layer detaches from the bulk material [54]. Phase explosion happens at a higher laser fluence. In this mechanism, the surface is rapidly melted at very high temperatures, nearing the critical temperature for metals. This causes the material to become a mix vapour and nano droplets. This mechanism also ablates material very efficiently: for nanosecond lasers, the threshold at which phase explosion starts is marked by a rapid increase in the size of the ablation crater per pulse [55]. Figure 2.7 shows thermal processes typical for a wide range of laser pulse lengths and fluences. In the ultrafast range, the dominant mechanisms are spallation and phase explosion.

2.2.2 Morphological Changes Induced

Ultrafast laser machining causes particular morphological changes on metallic surfaces. The craters formed by ultrafast laser systems compared to fast laser systems are formed by different mechanisms. Since nanosecond lasers have longer duration pulses, there is more time for electrons to transfer heat to the lattice so more thermal effects have a role in

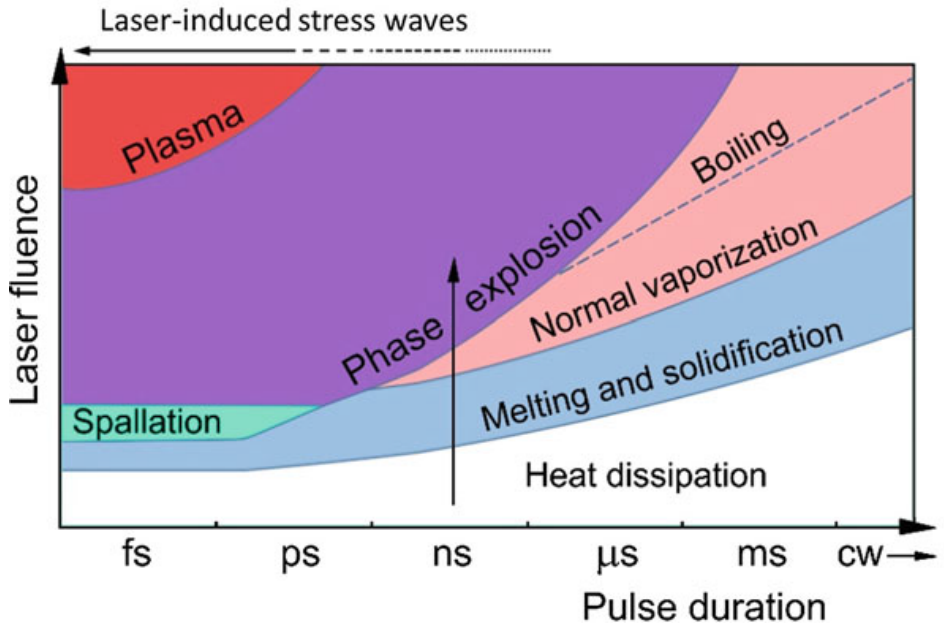

Figure 2.7: Thermal processes when irradiating materials with lasers. The upwards arrow shows that a certain pulse length may undergo a few mechanisms with laser fluences varying over time. Taken from [55].

the ablation of materials and more molten material can be seen at the edge of the crater. Figure 2.8 shows the difference between a crater drilled by an ultrafast laser and a fast laser. Random nanocavities and nano protrusions may form when the number of pulses from an ultrafast laser is low. Increasing laser fluence increases the area of these nanocavities and nano protrusions up to a certain point, where some traces of melting and cooling are seen [54].

The phase explosion mechanism of ablation for ultrafast lasers at high fluence may form nanoparticles from the particles being ejected from the surface, coalescing in the plume and then falling down on the surface. Vapours from the bulk material may also condense into particles in the air and redeposit on the surface. Such nanoparticles are shown in figure 2.9 c, d, g and h.

Laser-Induced Periodic Surface Structures (LIPSSs) are often observed when laser machining materials with any kind of laser. They are periodic lines seen on materials irradiated by a linearly polarised laser. LIPSSs are classified in two categories: Low-Spatial Frequency

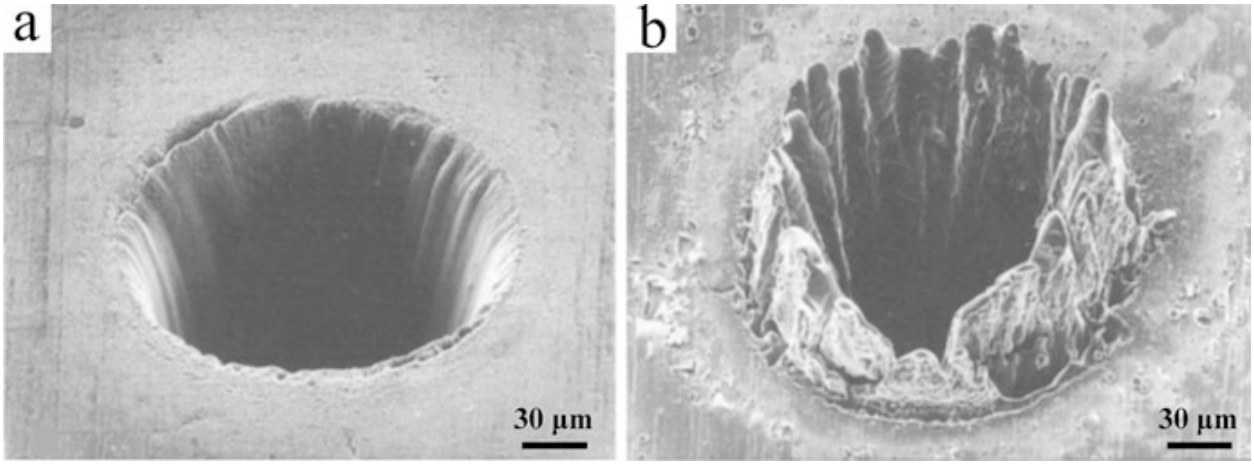

Figure 2.8: Ablated craters from (a) a 250 fs, 2.5 J/cm^2 laser and (b) a 3.3 fs, 4.2 J/cm^2. The crater drilled by the ultrafast laser has much smoother morphology. Taken from [57].

LIPPSs (LSFLs) and High-Spatial Frequency LIPPSs (HSFLs). LSFLs typically have a period that is comparable to the wavelength of the laser, while HSFLs have a much shorter period [58]. LIPSSs are shown in figure 2.9 a, b, e and f. The LSFLs in metals have a periodicity that is given by the following equation, provided that the LIPSSs are not too deep [58]:

$$\Lambda_{LSFL} = \lambda \times \mathrm{Re}\left\{\sqrt{\frac{\epsilon+1}{\epsilon}}\right\} \tag{2.14}$$

where λ is the wavelength of the incident laser and ϵ is the permittivity of the metal. HSFLs have a periodicity that is less than half of the incident laser wavelength.

It is generally agreed upon that LSFLs are the result of interference between surface electromagnetic waves and the laser light. The interference leads to the energy being periodically distributed on the surface, leading to modulated heating, melting or even ablation of the surface [58]. HSFLs appear in metals when irradiating them with a fluence that is close to the ablation threshold [58].

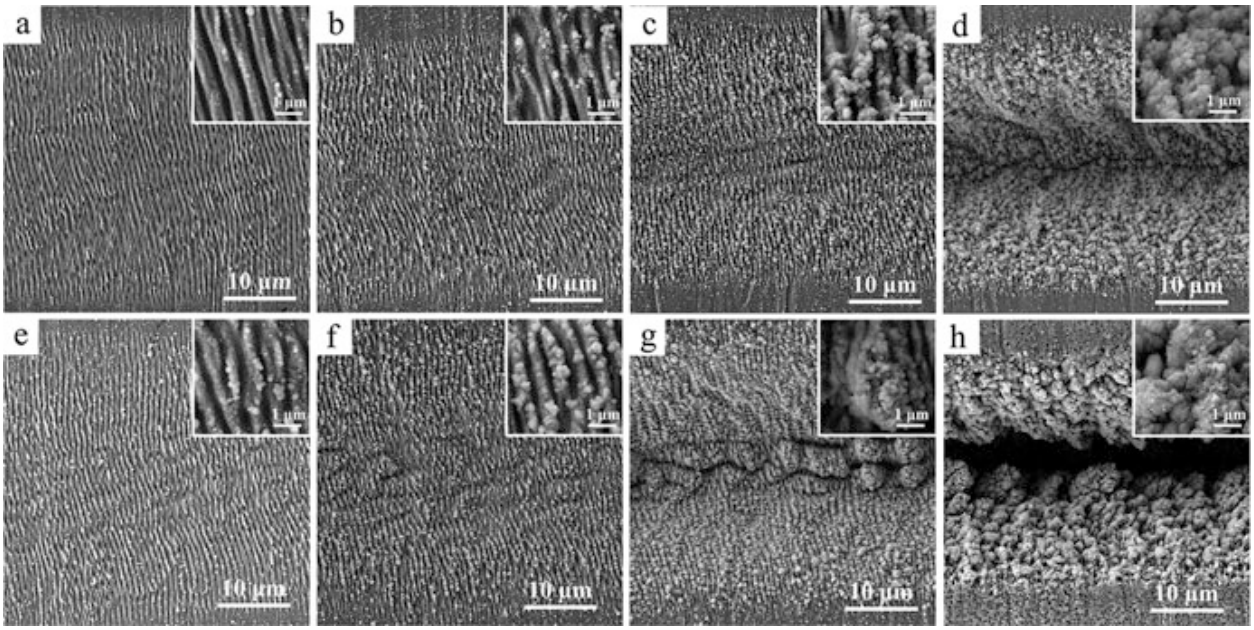

Figure 2.9: Morphology of laser-irradiated areas with different laser parameters, as follows: Fluence = 1.2 J/cm^2 (a-d), 2.4 J/cm^2 (e-h), Effective number of pulses = (a, e) 50 , (b, f) 100, (c, g) 200, (d, h) 400. LIPSSs are seen in (a, b, e, f) and nanoparticles are seen in (c, d, g, h). Taken from [54].

2.2.3 Laser-Induced Oxides

Due to the high pulse energy of fast and ultrafast lasers, interesting phenomena happen in the ambient air during laser ablation which may cause chemical changes to the ablated material. Dissociation of oxygen molecules into atomic oxygen occurs near the laser beam. Ozone may form in the region where the oxygen is dissociated. The ozone and atomic oxygen are highly reactive and will oxidise the laser machined material. Laser-induced oxides are what allows the PLD fabrication technique to fabricate oxide thin films. Oakes *et al.* have also used a CO_2 laser to dissociate O_2 and create oxygen atoms for the oxidation of silver [33].

The ablation of the material is important to consider for the discussion of laser-induced oxidation processes. In the plume, there is a mix of nanoparticles, microparticles and a vapour phase. Vorobyev & Guo state that oxidation efficiently happens from nano chemical processes, both in the ablation plume and on the liquid/solid surface nanostructure. Their

study focuses on the femtosecond ablation of aluminium [59]. During ablation, the laser light is absorbed by the material, then particles and vapour are ejected from the bulk material in the irradiated area, which forms the ablation plume, and the material is then redeposited [60].

A crucial part of the laser-induced oxidation process is the formation of shockwaves in the air from the ablation of the material. The ablation of the material creates a plume that expands rapidly in the ambient gas. This plume compresses the ambient gas in front of it so much that a shockwave is formed. The highly compressed gas has a high temperature, for which a high percentage of O_2 molecules get dissociated. The oxygen atoms react with the ablated metal. Chen *et al.* studied this phenomenon by comparing the ablation plume shapes in O_2 and Ar [61]. The authors have imaged the plume via a Charge-Coupled Device (CCD) camera. Figure 2.10 shows the differences between the ablation plume from the target material in O_2 and Ar. The plume shape is similar for both gases for an ambient pressure of up to 20 Pa but differ for higher pressures. Chen *et al.* suggest that the differences in width and length arise from the scattering processes remaining elastic in Ar but becoming inelastic in O_2 since O_2 dissociation and chemical reactions take place. At lower pressures, dissociation processes in O_2 do not take place, explaining the similarity between the ablation plumes of O_2 and Ar [61]. Camposeo *et al.* have also studied the dissociation of O_2 molecules during pulsed-laser ablation by means of absorption spectroscopy of atomic and molecular oxygen. They have also found that a threshold pressure is needed for the dissociation of molecular oxygen [62].

Dissociation and ionisation of the air may also happen when the laser beam gets focused so that the intensity reaches a critical value. The required intensity for this to happen is very high and this phenomenon is accompanied with a bluish white spark. This threshold depends on many parameters from the laser itself (such as spot size and pulse length) and it depends on the surrounding gas and its pressure as well [63]. The plasma generated from gas breakdown may also form shockwaves which also dissociates oxygen molecules [64].

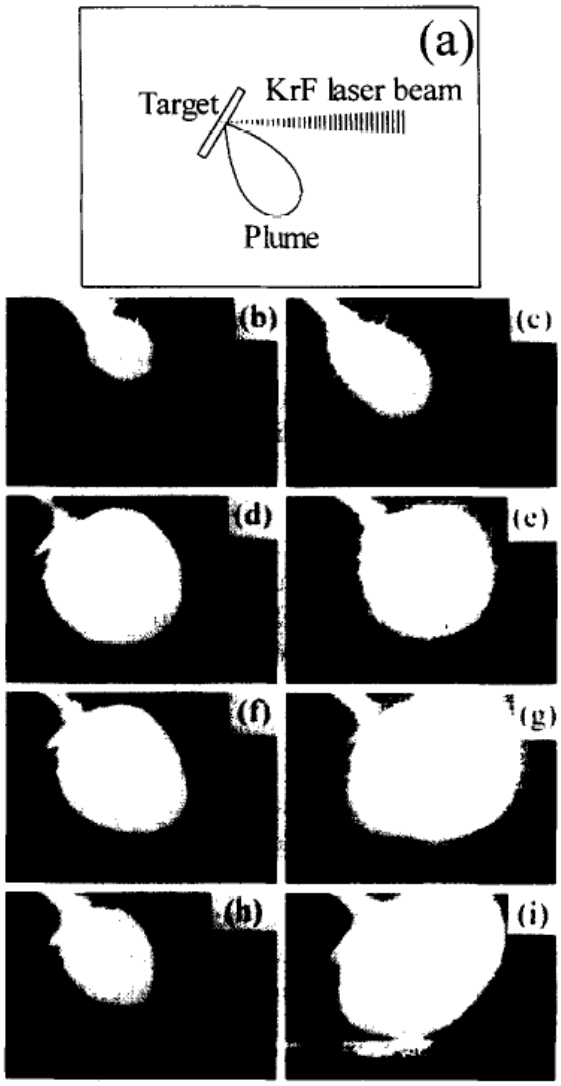

Figure 2.10: (a) Sketch showing a typical CCD image of an ablation plume. (b-i) Plume images from ablation in (b) vacuum, (c) 2 Pa O_2, (d) 20 Pa O_2, (e) 20 Pa Ar, (f) 40 Pa O_2, (g) 40 Pa Ar, (h) 150 Pa O_2, (i) 150 Pa Ar. Taken from [61].

2.3 Characterisation Techniques for Metal Oxides

Silver oxides have been characterised using many spectroscopic methods in the literature. These include (but are not limited to) EDS, XPS, FTIR and Raman spectroscopy.

There are also non-spectroscopic techniques used to detect the presence of silver oxides. The mass of a silver sample that has reacted to become silver oxide should increase, meaning that the change in mass may be studied to detect oxidation. QCM are used to study changes in mass as silver oxidation occurs. The silver is deposited directly on the QCM, then oxidised from atomic oxygen [3, 14, 32, 33]. The resistance of silver oxide samples is also higher than that of pure silver. Measuring the change in resistance is another way to study chemical changes on silver surfaces [32]. Both these methods indicate that some oxidation occurred, but they do not give any information regarding the type of oxide formed.

2.3.1 Energy-Dispersive Spectroscopy (EDS)

EDS is used to analyse the elemental composition of samples. It works by ejecting an inner shell electron from atoms, from which the electron vacancy gets filled by an upper shell electron. This forms a characteristic X-ray which gets detected. The process is shown in figure 2.11. Since every element has a distinct atomic structure, this allows for detection of the elements composing the sample. Electron beams are often used to eject the electron because of their smaller spot size. This method presents some good advantages that make it a good characterisation technique for metal oxides. It has a good spatial resolution, is used with SEM and spectra are efficiently acquired. Its main limitation is that it only gives information regarding the elemental composition of samples and gives no information regarding their molecular composition [65]. This means that while oxygen and silver atoms may be detected in silver oxide, the only information available regarding the oxidation state of the silver oxide is the relative intensity of the O atom signal compared to the Ag signal. This makes it difficult to differentiate between Ag_2O and AgO from EDS data. Another limitation

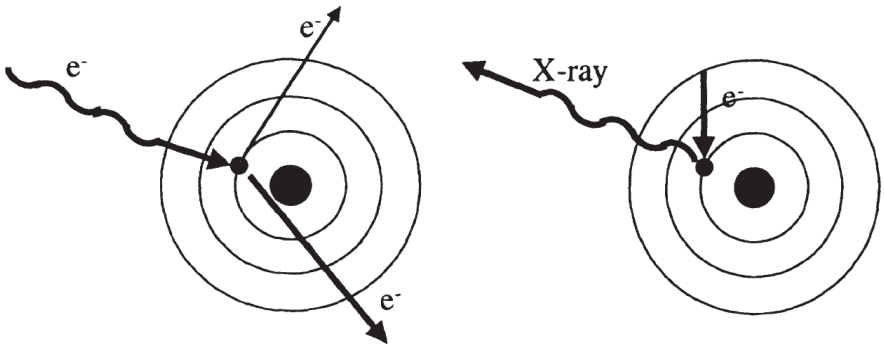

Figure 2.11: Principle of EDS, in which an upper shell electron takes the place of an ejected inner shell electron, generating an X-ray. Taken from [65].

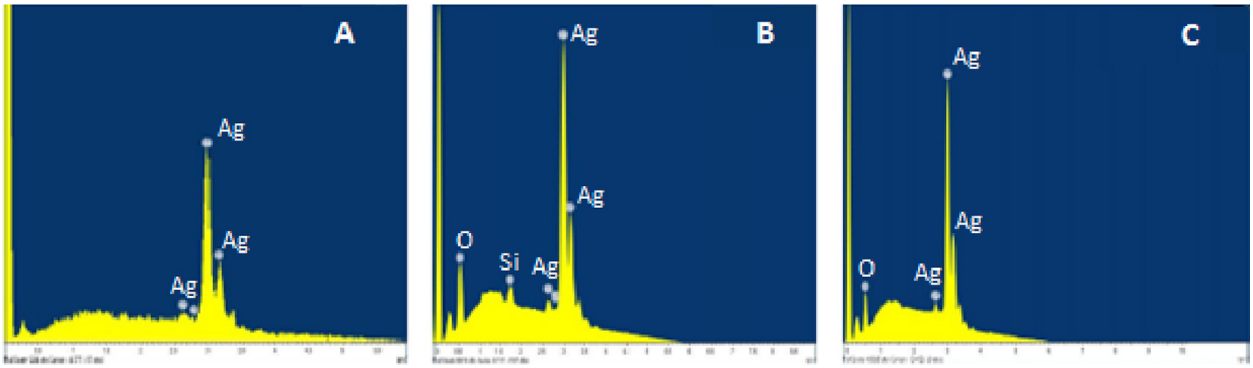

Figure 2.12: Example of EDS spectra of silver oxide thin films. The deposition parameters are: (A) 300 W sputtering power, 0 sccm O_2 flow rate, (B) 200 W sputtering power, 6 sccm O_2 flow rate, (A) 400 W sputtering power, 4 sccm O_2 flow rate. On the x axis is the energy in keV and on the y axis is the intensity. Taken from [27].

is the depth at which the material gets probed may be larger than desired, meaning this characterisation method may not be suitable for thin films [65].

EDS has been used as a mean to detect silver oxide in the literature [27, 39]. An example of an EDS spectra of silver films and silver oxide films is shown in figure 2.12. The Ag and O peaks confirm the presence of a silver oxide with unknown oxidation state. The silver oxide thin film is prepared using reactive sputtering, and each spectrum is of a thin film prepared with distinct sputtering powers and oxygen flow rates. The Si peak is from the glass substrate on which the silver oxide was deposited.

2.3.2 X-Ray Photoelectron Spectroscopy (XPS)

XPS works by detecting electrons ejected by X-rays. Measuring the kinetic energy of the ejected electron and knowing the energy of the X-ray photon, the binding energy can be calculated. The kinetic energy of the ejected electron, the energy of the X-ray photon and the binding energy are related by the following formula [66]:

$$\mathrm{KE} = h\nu - \mathrm{BE} - \phi_s \tag{2.15}$$

KE denotes the kinetic energy of the electron, $h\nu$ is the X-ray photon energy, BE is the binding energy of the orbital and ϕ_s is the detector work function. In addition to photoelectrons, Auger electrons are emitted from the energy shift of an upper-level electron to a lower level and the emission of another electron takes place. A sketch of the process is shown in figure 2.13. Electrons that leave the sample and are in a specific energy window are then detected. An electric field may be applied to shift the energy window. This method is advantageous in characterising surfaces because molecules can be identified based on small changes in the binding energies of the atoms [66]. For example, silver atoms in a silver oxide molecule have slightly different binding energies compared to pure atomic silver. The main limitation of this method is the low spatial resolution, which is in the order of tens of µm according to [66]. This resolution is too large for mapping laser micromachining surface chemistry from femtosecond laser machining.

XPS has been widely used in literature for the characterisation of silver oxides [3, 6, 7, 15, 16, 23, 27, 29, 40, 45, 67]. The $3d_{5/2}$ binding energies of Ag, Ag_2O and AgO are reportedly 368.1 eV, 367.7 eV and 367.4 eV respectively [2]. This small change in binding energy allows to differentiate between silver oxides. For example, figure 2.14 shows the shift in the $3d_{5/2}$ binding energy for a silver powder that was then oxidised by ozone at a few different temperatures. It is clear that the powder exposed to ozone at room temperature has a peak at 367.4 eV, showing that the main oxide is AgO. At a higher temperature, the

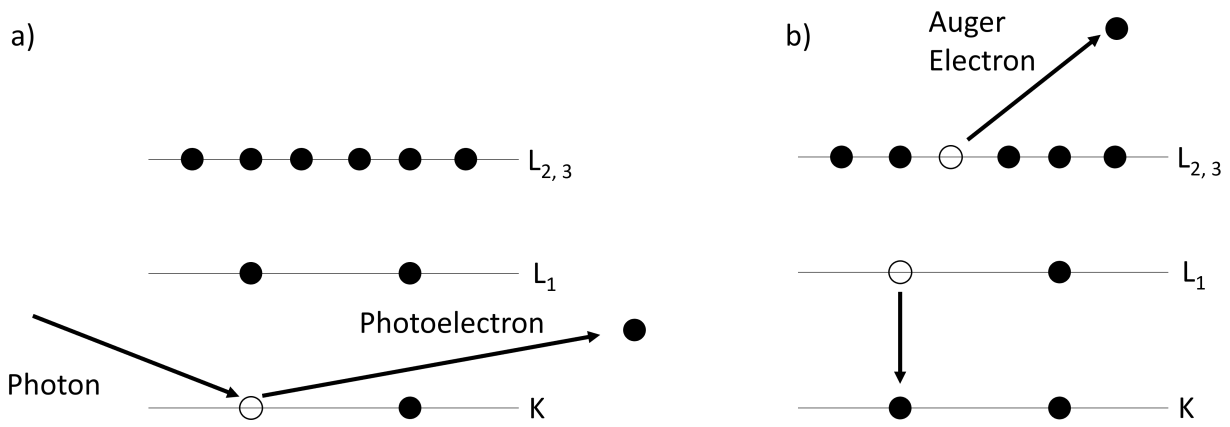

Figure 2.13: Principle of XPS. (a) An X-ray photon ejects a photoelectron from the atom, which will get detected. (b) An electron fills the vacancy left by the ejected electron while another electron (the Auger electron) is emitted.

peak is at 367.8 eV, which means Ag_2O is primarily there. At the highest temperature, the binding energy is at 368.2, the same as Ag, meaning the Ag powder did not oxidise [16].

2.3.3 Fourier-Transform Infrared (FTIR)

In FTIR spectroscopy, a sample is illuminated by an infrared source (non-monochromatic), and the absorption of the infrared radiation by the source is measured. The molecules composing the sample absorb the infrared radiation and vibrate. Vibrational states of molecules are quantised and will absorb precise energies of the infrared radiation. There are two types of normal vibrational modes: stretching modes and bending modes. For a vibrational mode to be detected by FTIR, its dipole moment must be changing during the vibrations. A sketch of vibrational modes for a linear molecule such as Ag_2O is shown in figure 2.15. The spectral distribution is found via the Fourier transform of the spectrograph given by an interferometer. In FTIR, the infrared source goes through an interferometer, is focused on the sample then the outgoing light is detected. Since the acquired data is in the time domain, a Fourier transform must be applied to get the data in the frequency domain. The chemical composition of samples is characterised by identifying spectra unique to a molecule or functional groups that give information about a part of the chemical species observed.

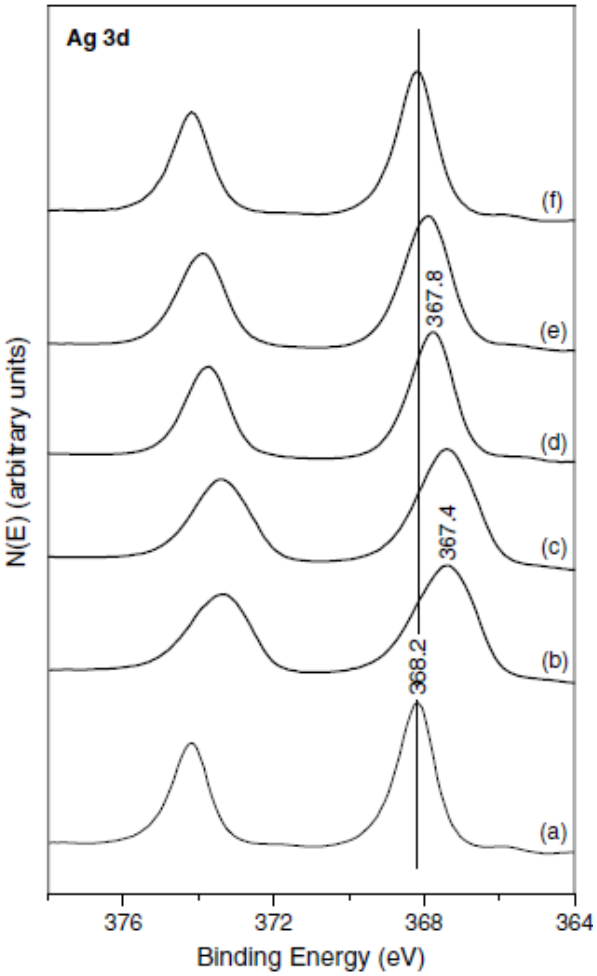

Figure 2.14: Examples of XPS spectra. The material is (a) pure Ag powder, then Ag powder exposed to O_3 for 30 minutes at: (b) at 300 K (c) 473 K (d) 673 K (e) 773 K (f) 923 K. The x axis is the binding energy, and the y axis is the number of electrons detected. Taken from [16].

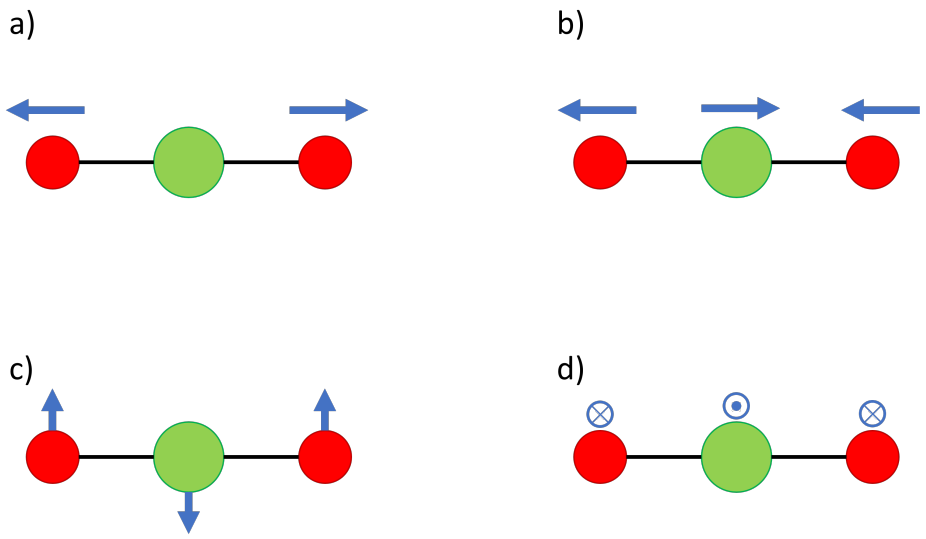

Figure 2.15: Modes of vibration of a linear molecule such as Ag_2O. There is the symmetrical stretch (a), the asymmetrical stretch (b), the in-plane bend (c) and the out-of-plane bend (d). The green circle represents the Ag atom and the red circles represent the oxygen atoms. Note that the symmetrical stretch will not be detected by FTIR since the dipole moment does not change. Adapted with permission from reference [68].

This characterisation method is widely used for organic chemical species since it gives great details regarding the structure of molecules. It also gives useful information regarding the absorptivity of molecules. While the light source can be focused via a microscope objective, this method presents a limitation on its spatial resolution due to the light not being monochromatic and diffraction limit due to the wavelength of radiation [68].

FTIR has been used to detect silver oxides, as reported in the literature [28, 29, 41]. Both silver oxides have a distinct infrared absorbance spectrum, with each band representing a vibrational mode. Ag_2O has been reported to have a band at 86 cm^{-1}, representing an O-Ag-O bending mode and a broad band at 525-540 cm^{-1} from an asymmetrical Ag-O stretching mode. AgO has many more bands: an asymmetric Ag-O stretching mode gives a band from 525-540 cm^{-1} from the Ag^{I} ion linearly coordinated with two oxygen atoms, and two bands should be assigned for the Ag-O stretching modes of the $Ag^{III}O_4$ unit [41]. The wavenumbers of the identified bands for AgO are: 60, 69, 130, 155, 194, 254, 384, 525-540, 951 and 986 cm^{-1}. Figure 2.16 shows an example of FTIR spectra for both Ag_2O and AgO.

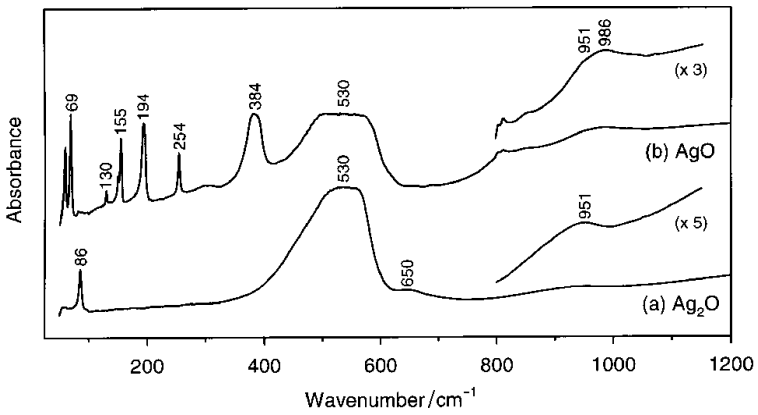

Figure 2.16: Example of the FTIR spectra of (a) Ag_2O and (b) AgO. The x axis is the incident light wavenumber in cm^{-1}, and the y axis is the absorbance of the sample. Taken from [41].

2.3.4 Raman Spectroscopy

Raman spectroscopy is similar to FTIR in that they are both vibrational spectroscopy techniques. The main difference of Raman spectroscopy, when compared to FTIR, is that it involves inelastic scattering of photons with molecules to probe the material instead of measuring the absorption of photons by the material. The scattered photons leave the molecule with their energy shifted by a small amount, via either Stokes (outgoing photon has lower energy) or anti-Stokes (outgoing photon has higher energy) scattering. The difference in energy is called the Raman shift and is what is reported by Raman spectra. Figure 2.17 shows the energy shifts of Stokes and anti-Stokes scattering. The Raman scattering only occurs if it induces a change in polarizability [69]. Another way to explain Raman spectroscopy is with phonons; when a photon interacts with a lattice, it will sometimes create (or destroy) a phonon. The frequencies and momenta of the incident and outgoing photons are related as follows:

$$\omega_s = \omega_p \pm \omega_{osc} \tag{2.16}$$

$$\vec{k}_s = \vec{k}_p \pm \vec{q} \tag{2.17}$$

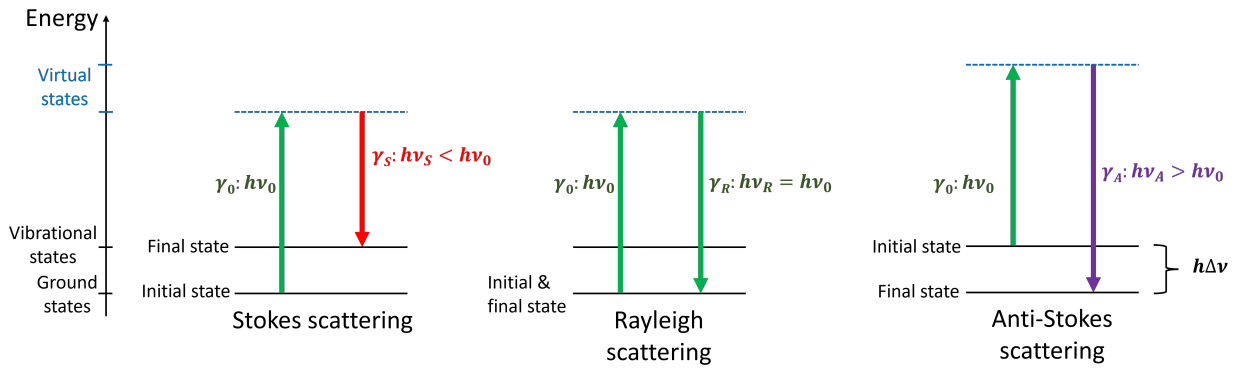

Figure 2.17: Diagram of the energy shifts in Stokes and anti-Stokes Raman scattering. Photons are denoted as γ with energies $h\nu$. γ_0 is the incident photon, γ_S is the photon after Stokes scattering, γ_R is the photon after Rayleigh scattering, and γ_A is the photon after Anti-Stokes scattering. The energy shift is denoted by $h\Delta\nu$.

where the subscripts s means the scattered photon, p means the incident photon, osc means the vibration of the lattice, and the vector $\vec{q}$ is the momentum of the created/destroyed phonon. The $\pm$ sign is positive in the case of Anti-Stokes scattering (destruction of a phonon) and negative in the case of Stokes scattering (creation of a phonon) [70]. A typical confocal Raman microscope includes a monochromatic light source, a diffraction grating (for dispersive Raman spectroscopy), and a detector (CCD) [71]. A sketch of such a setup is shown in figure 2.18. There also exists a setup (Fourier Transform Raman spectroscopy) which uses an interferometer to analyse the spectrum instead of a diffraction grating. Similar to the FTIR characterisation technique, a Fourier transform is applied to switch from the time-domain to the frequency domain [69].

A limitation of this method is the difficulty in doing quantitative analysis of the spectra. Raman scattering also happens much less often compared to Rayleigh scattering (outgoing photon has the same energy as the incoming one). An objective can be added to the setup shown in figure 2.18 to focus the laser on the sample, making the laser spot size much smaller and achieving excellent spatial resolution (in the order of 1 µm) [69]. This method, which is called micro-Raman spectroscopy, combined with the ability of Raman scattering to precisely characterise chemical species, make it a great choice to study the surface chemistry

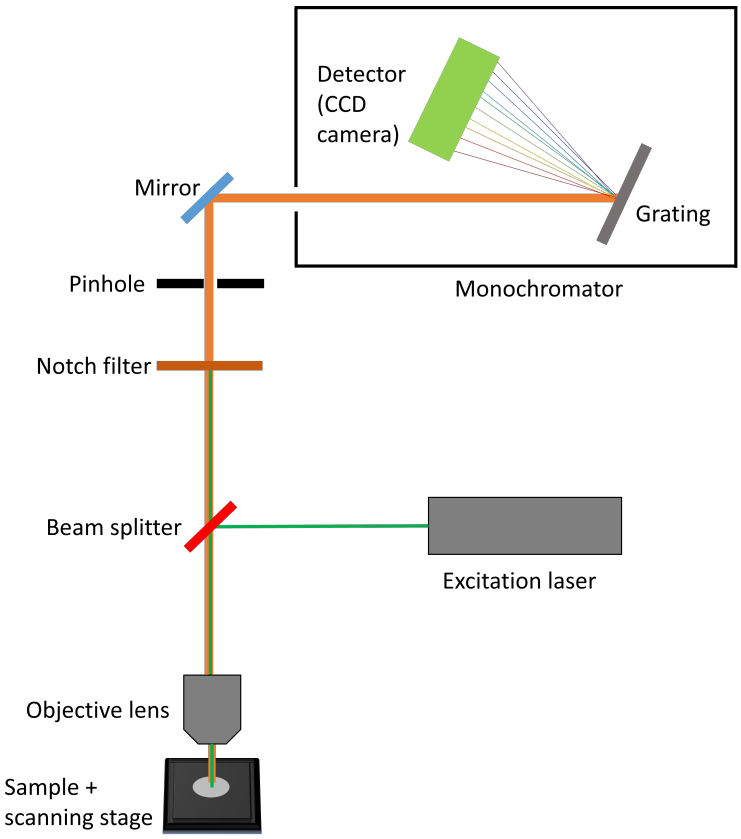

Figure 2.18: Typical confocal Raman spectroscopy setup.

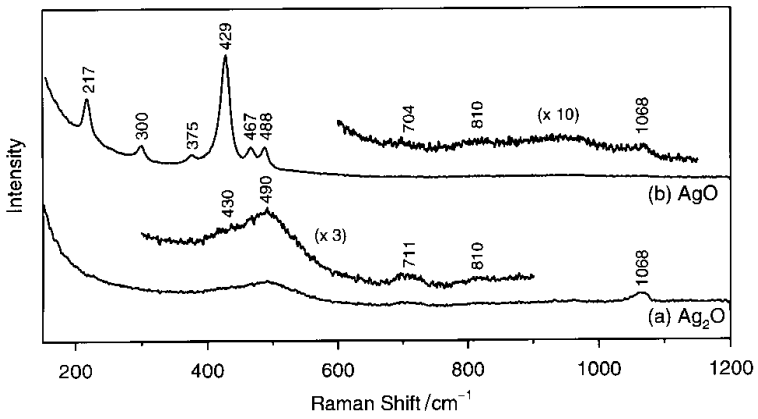

Figure 2.19: Raman spectrum of (a) Ag_2O and (b) AgO. Taken from [41].

of samples micro-machined by ultrafast laser.

Raman spectra have been reported in the literature for both silver oxides [1, 6, 16, 29, 34–37, 41, 43, 72, 73]. Ag_2O has a single broad band at 490 cm^{-1} [41]. AgO has reportedly six sharp bands corresponding to six Raman active modes: in-phase stretching of the $Ag^{I}O_2$ unit at 223 cm^{-1}, out-of-phase stretching of the $Ag^{I}O_2$ unit at 307 cm^{-1}, in-phase breathing at 480 cm^{-1}, asymmetric stretching at 483 cm^{-1}, out-of-phase breathing at 517 cm^{-1} and a twist mode at 419 cm^{-1} according to Grzelak *et al.* [6]. Figure 2.19 shows an example of Raman spectrum of Ag_2O and AgO.

Raman scans have also been reported in the literature to map chemical species on the surface of laser machined samples [1]. An example of a Raman map is shown in figure 2.20. In this example, Raman spectra are taken at each pixel of the image and then integrated over the Raman bands corresponding to Ag_2O and Ag_2CO_3. The total counts in each band are then plotted in a 2-D plot, where brighter colors correspond to a more intense Raman signal over the interval integrated over (some background subtraction is also applied). This allows to have a clear picture of where the chemical species are located.

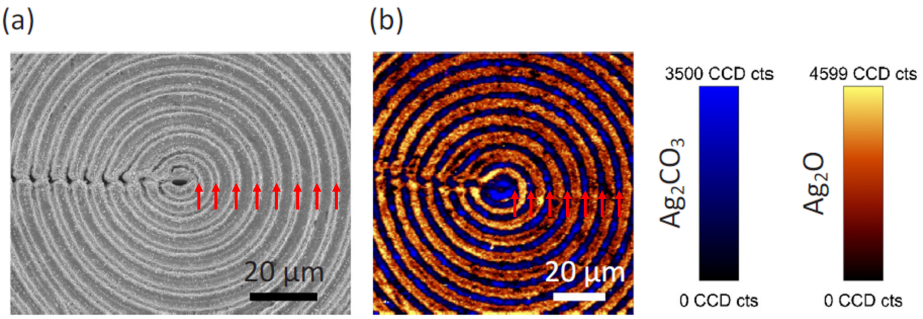

Figure 2.20: (a) SEM image of a sample laser machined in a concentric ring pattern. (b) Example of a Raman map. Here, the material that is directly laser machined show much more Ag_2CO_3 and less Ag_2O. The circles corresponding to the laser machined path are indicated by the red arrows. This shows that the laser machined silver and Ag_2O react much more with CO_2 to form Ag_2CO_3. Adapted with permission from reference [1].

2.4 Research Objectives

Most of the literature regarding the femtosecond laser ablation of silver focuses on morphology changes and ablation mechanisms [74–78]. Literature on the surface chemistry of silver after femtosecond ablation is very scarce; there is a paper from our group on the rapid formation of Ag_2CO_3 from nanostructured Ag_2O [1], but no work regarding the formation of AgO from femtosecond laser has been published yet.

The main objective of this work is to study chemical species that may be formed from femtosecond laser machining of silver via Raman spectroscopy. More precisely, silver oxides are studied here. The threshold number of pulses and pulse energy to form Ag_2O and AgO are found, the dependence of those fluences on laser wavelength and repetition rate are studied. The decomposition of the silver oxides from femtosecond laser ablation is studied.

Chapter 3

Methodology

Silver pellets, pressed in the shape of a disc, were laser machined using the femtosecond laser machining setup described in section 3.2. The surface chemistry of the laser machined samples was then studied using Raman spectroscopy, SEM and optical microscopy. A silver oxide sample made with an oxygen plasma etcher was also studied using Raman spectroscopy.

3.1 Sample Preparation

3.1.1 Silver Pellets

Silver pellets that were stored in vacuum were pressed into disks by a steel die cleaned with polycellulose wipes and acetone, isopropanol then deionised water. A picture of the steel die along with an unpressed and a pressed silver pellet are shown in figure 3.1. A picture of the press is shown in figure 3.2. Some silver pellets were then studied with the Raman setup described in section 3.3 to study how clean the samples are after pressing them. Raman spectroscopy is used to ensure that the silver surfaces are free of chemical impurities.

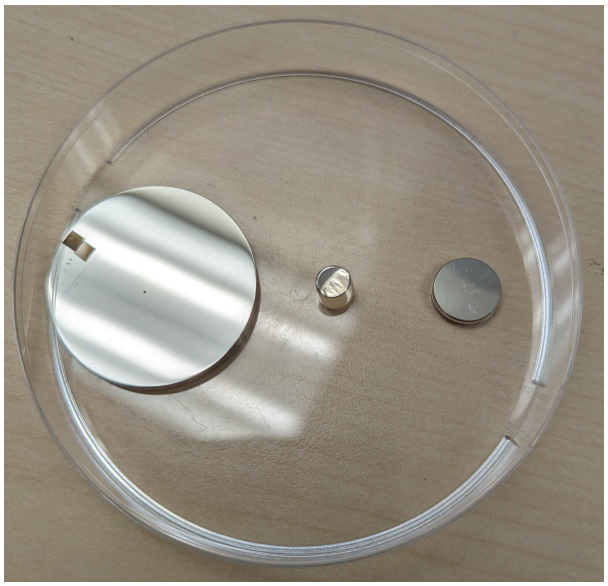

Figure 3.1: On the left side is the steel die, at the center is an unpressed silver pellet and on the right side is a pressed silver pellet. The steel die is about 4 cm in diameter and the pressed silver pellet is about 1 cm.

Figure 3.2: Press used to prepare the silver pellets.

3.1.2 Silver Oxide Pellet

In a brief set of experiments, a pressed silver pellet has been treated with oxygen plasma to yield a silver oxide pellet. For this, a pressed silver pellet is treated in an oxygen plasma generator (Plasma Etch PE-50 cleaner), set at 25 W, with the oxygen flow rate set to 10 sccm for 5 minutes. A picture of the equipment is shown in figure 3.3. The resulting pellet had a dark grey colour, as shown in figure 3.4.

Figure 3.3: Plasma Etch PE-50 cleaner used for the oxygen plasma treatment of a silver pellet.

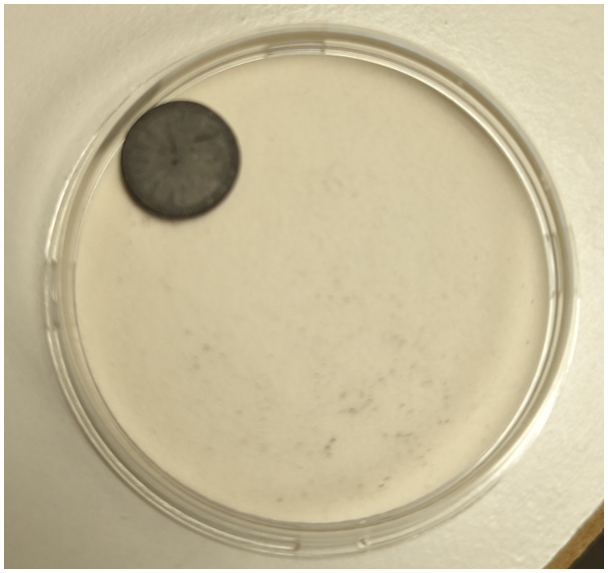

Figure 3.4: A silver oxide pellet fabricated by treating a pressed silver pellet with oxygen plasma.

3.2 Laser Machining Setup

Dot matrices were laser machined on the silver surface, with each dot being machined with a different set of parameters, as shown in figure 3.5. Other parameters were changed in subsequent experiments, such as the repetition rate and the laser frequency. The laser machined silver was then studied with Raman spectroscopy.

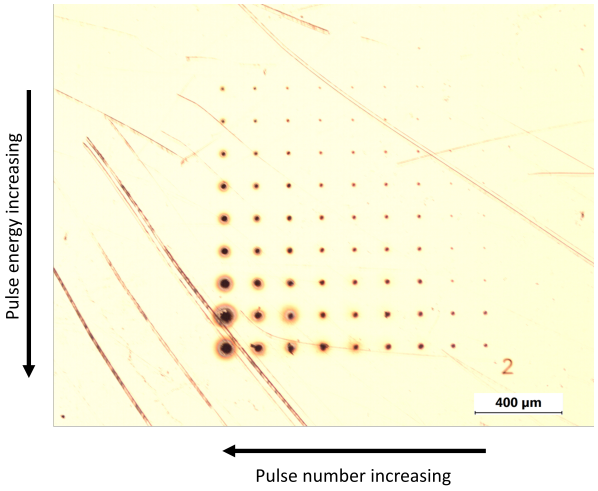

Figure 3.5: Example of a laser-machined dot matrix. The horizontal axis has decreasing number of pulses from left to right, and the vertical axis has increasing pulse energy (and power) from top to bottom.

For laser machining, an Ytterbium Doped Potassium Gadolinum Tungstate (Yb:KGW) femtosecond pulsed laser (PHAROS from Light Conversion Inc.) at various repetition rates (typically 1 kHz-200 kHz, although lower frequencies can be used), 1030 nm wavelength is used. For these experiments, the repetition rates used ranged from 1 Hz to 15 kHz. The laser is frequency-doubled using a Barium Borate (BBO) crystal, followed by a 1030 nm reflector to remove the remaining fundamental light. The laser path can be modified with a set of flip mirrors to bypass the BBO crystal. The pulse length is 300 fs. The laser beam goes through a half waveplate controlled by the computer which adjusts the power, then a polariser, then another half waveplate controlled by the computer to adjust polarisation. Table 3.1 shows an example of laser power with respect to pulse energy, and figure 3.6 shows the relation between polariser angle and pulse energy. The pulse energy is calculated using the following

formula:

$$E = \frac{P}{R} * \eta \tag{3.1}$$

where E is the pulse energy in Joules, P is the laser power in Watts, R is the set repetition rate of the laser in hertz and η is the efficiency of the microscope objective (42%). The angle values may vary from day to day due to laser fluctuation and changes in the optical setup. The laser then passes through a beam expander and finally through a 20x objective to yield a laser with a beam width of a few microns. The 20x objective transmits around 42% of the power. A detector may be placed in front of the 20x objective to measure the power. This setup creates a focused laser at the sample which can create craters with a diameter of around 6 µm according to D^2 measurements. The method is described in details in reference [79]. The sample is mounted on a 3-axis stage, moving in the x, y and z axis. For the x and y axis, an Aerotech ANT130-XY 2-axis nano positioning stage, with a resolution of 1 nm and a bidirectional repeatability of ±75 nm, is used. For the z axis, an Aerotech ANT130-V direct lift nano positioning stage, with a resolution of 2 nm and a bidirectional repeatability of ±150 nm, is used. A shutter controlled by the computer is used to block or allow the beam to pass as requested. A fume extractor device (from BOFA) is installed close to the sample to prevent ejected material from damaging the microscope objective and to remove any potential fumes from laser machining. The controller used to control the xyz stage, both half waveplates and the shutter are controlled by an Aerotech A3200 NPAQ, which has a feature called Position-Synchronised Output (PSO). PSO allows the NPAQ controller to request the laser to fire at specific events, such as when any axis moves a certain distance, or when specifically requested by the program. Other parameters can be specified using the PSO, such as the number of pulses to send per firing event (or the number of cycles), the time the laser is on per cycle and the total time of a cycle. A chromatic point sensor (CCS-PRIMA from Acuity) is used to calibrate the z axis, so that the laser is always focused on the sample in case it is not perfectly flat. Figure 3.7 shows the full machining setup.

Power [mW]	Pulse energy (after objective) [µJ]
5	0.21
10	0.42
25	1.05
50	2.10
75	3.15
100	4.20
150	6.30
200	8.40
227	9.53

Table 3.1: Pulse energies compared to laser powers for a repetition rate of 10 kHz.

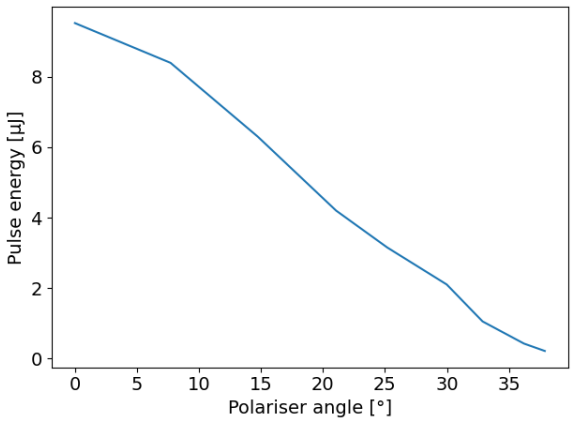

Figure 3.6: Relation between polariser angle and pulse energy (after the objective).

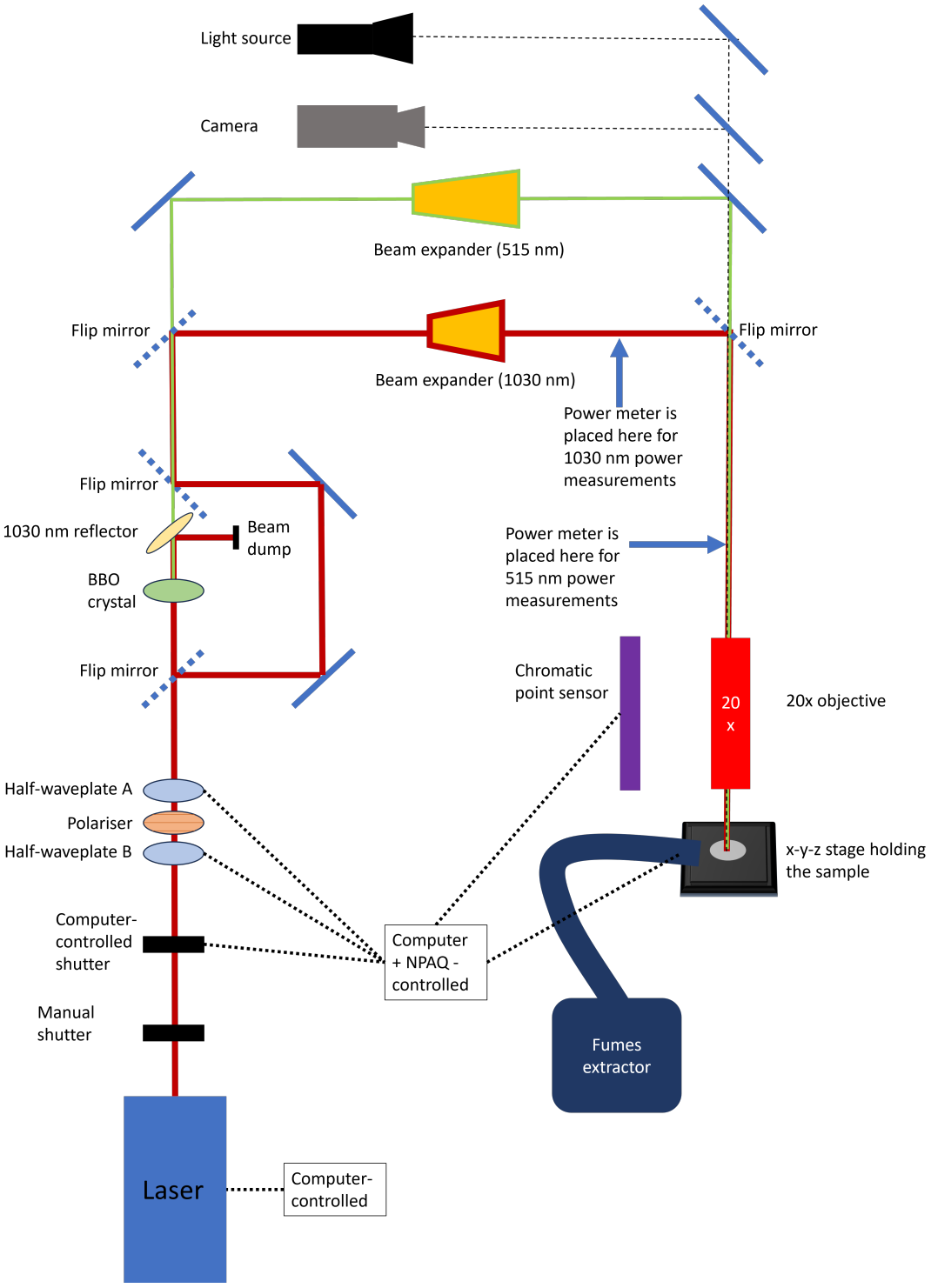

Figure 3.7: The optical setup used for femtosecond laser machining. The computer-controlled shutter allows the computer to open or close a shutter on request, half-waveplate A controls the polarisation of the beam, half-waveplate B allows the computer to control the outgoing power, a series of flip mirrors allow the selection of the laser wavelength (515 nm or 1030 nm when bypassing the BBO), and the x-y-z stage allows to position the sample under the laser beam.

3.3 Raman Spectroscopy

Raman spectroscopy is the method of choice to find chemical species formed on the silver after laser machining. As discussed in section 2.3.4, it is often used in literature to detect silver oxides and is a great choice to characterise chemical species formed by femtosecond laser ablation. To transport the machined sample from the laser to the Raman microscope, the sample was stored in ambient air in a container. It takes from 10 to 15 minutes to transport the sample between the femtosecond laser and the Raman microscope.

The Raman spectra from these experiments were recorded using a WITec a300, irradiating the sample with a 532 nm continuous wave laser source. The laser is focused with a 20x microscope objective, and low power is used to reduce the photodecomposition of the silver oxides. For the spectrograph, a Princeton Acton SP300 is used, with a CCD camera cooled to -60 °C, and a diffraction grating of 600 grooves/mm and blazed at 500 nm. Raman spectra were acquired every 2 µm, then wavenumber intervals were integrated over various areas of interest to construct a map of CCD counts highlighting areas with most counts. This produces an image that depicts areas with AgO and Ag_2O, and the two oxides can be differentiated since they have distinct (but similar) Raman responses (see figure 3.8). Each Raman spectrum is taken over an integration time of 0.3 seconds unless specified otherwise. This allows the spectrum to have low noise while still keeping the laser power low. Some background subtraction is applied when necessary to avoid Raman spectra with high background to be highlighted on the maps.

3.4 Scanning Electron Microscope (SEM)

An SEM is used to study the texture and morphology of the laser machined regions. A Gemini Zeiss 500 Field Emission Scanning Electron Microscope (FESEM) with an acceleration voltage set to 10 kV is used to take high-resolution images of the laser machined craters. These images are compared with the Raman scans and the bright field optical microscope

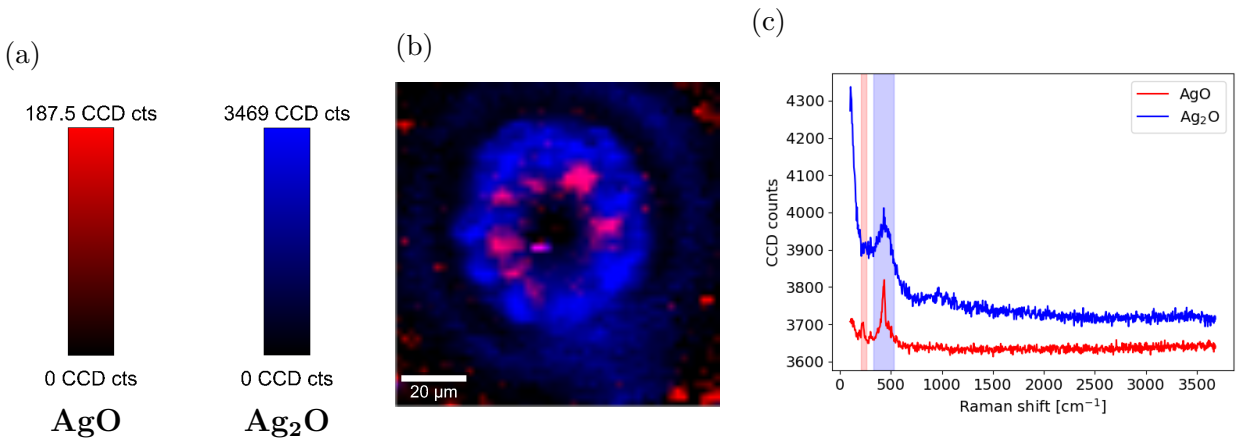

Figure 3.8: Example of a Raman scan for a laser machined dot. (a) Scalebars, (b) Raman image, (c) examples of Raman spectra for each oxide. The red shaded region in the spectra shows the area integrated for CCD counts highlighting AgO, and the blue shaded region indicates the area integrated for Ag_2O.

images. The images were taken with the in-lens detector, with an aperture of 20 µm. Due to the tendency of the Raman spectroscopy technique used in this thesis to damage the laser machined area, SEM images were taken on a different set of laser machined dots.

3.5 Optical Microscope

Most optical microscope images were taken with the optical microscope included with the WITec 300 described in section 3.3. Using this microscope presents a few advantages over using another one: the software included with the WITec allows image overlap and zoom synchronisation between images constructed via Raman spectra and images taken from the optical microscope, and optical microscope images can be quickly taken before and after a scan to see the damage caused by the continuous wave laser during the scan. All optical microscope images are taken with a 20x objective, under bright field and using reflection mode.

The only exceptions are figures 3.5, 4.1 and 4.2 which were taken with an Olympus BX51 optical microscope, under bright field, using reflection mode. This microscope was used in

cases where no Raman scans were needed to be done or when a larger area needed to be imaged.

Chapter 4

Laser Machining of Bulk Silver

In this section, silver oxide dependence on laser machining parameters is discussed. The parameters studied are pulse energy, number of pulses, repetition rate and laser frequency. An experiment is also conducted to find out the effect on AgO formation if Ag_2O is already present on the surface.

To make sure chemical impurities on the surface do not affect the results, two precautions are used in the experiments: the surfaces that look clean under an optical microscope are studied using Raman spectroscopy to make sure the surface does not contain chemical impurities. A Raman scan showing the appearance of carbon-contaminated surfaces is shown in appendix A. Also, each laser machined crater is machined a few times on different locations to characterise the reproducibility of the Raman response, and thus surface chemistry.

4.1 Morphology

Figures 4.1 and 4.2 show SEM images of two laser machined dots; figure 4.1 is a sample machined by 10000 shots at 10.08 µJ per pulse, and for figure 4.2 the sample is machined by 300 shots at 10.08 µJ per pulse. There are a few regions of interest here: a deep crater is found in the center, a slightly elevated rim is observed from 2 µm to around 10 µm from the center of the crater, followed by another region past 10 µm from the center of the crater.

(a)

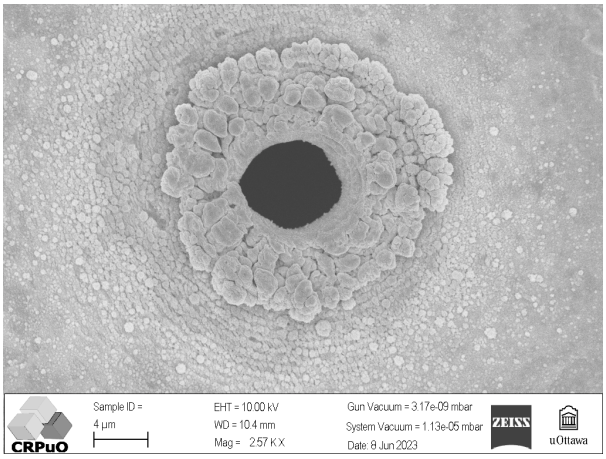

(b)

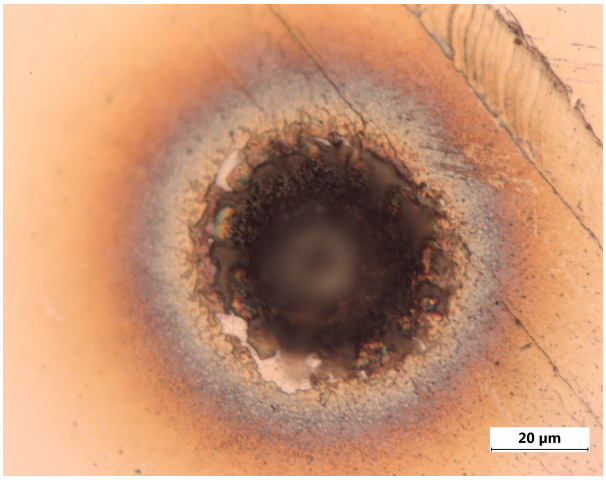

Figure 4.1: (a) SEM images of laser machined dots at 10.08 µJ per pulse and 10000 pulses (b) brightfield image of the corresponding dot.

The samples from which the SEM images are taken are different than the sample on which Raman scans were performed. This is because the continuous wave laser source illuminating the sample may affect the morphology of the sample and charging from the SEM could affect the sample chemically.

A few differences can be seen between these figures; in figure 4.1, the affected area is much larger than in figure 4.2. For the 10000 pulses case (figure 4.1), a lot of large particle-like structures that are slightly elevated are found from 2 µm to approximately 10 µm from the center of the crater. Beyond 10 µm, there are particles that are arranged in a periodic manner in concentric circles. Such an arrangement of nanoparticles may have interesting optical properties due to plasmons and diffraction effects, however it would be surprising if it were the reason for the greyish-blue circle often found in brightfield images, since the 300 pulses (figure 4.2) case should also have redeposited material of this color, yet it does not show such a periodic structure of particles. Far away from the crater (beyond 20 µm), the redeposited particles are randomly distributed for the 10000 pulses case. In the 300 pulses case, beyond 10 µm, there is a faint circle with a very slightly different surface morphology than unaffected silver, and the nanoparticles far from the crater are very scarce.

(a)

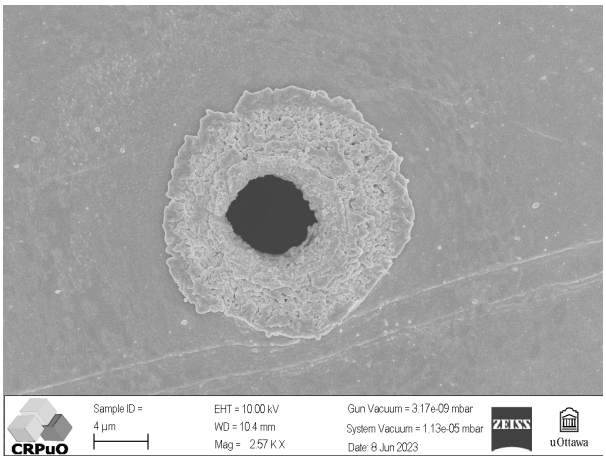

(b)

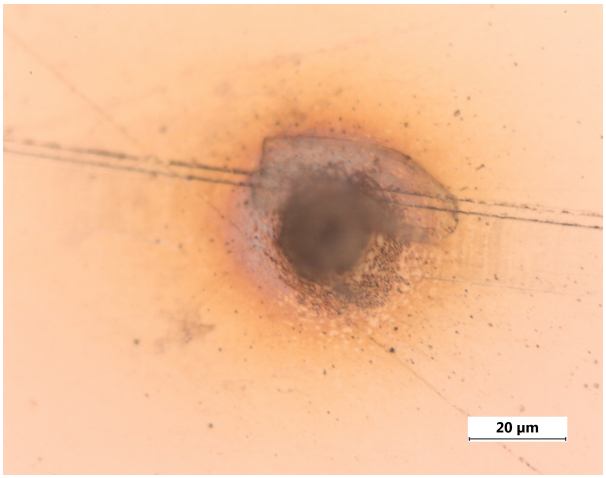

Figure 4.2: (a) SEM images of laser machined dots at 10.08 µJ per pulse and 300 pulses (b) brightfield image of the corresponding dot.

In both cases, the bottom of the crater is not visible; a rough structure from melting and re-solidification of the silver would be expected.

The periodic-like structure around the crater in figure 4.1 is characteristic of LIPSSs. It should be expected that LIPSSs appear after irradiation by repeated polarised laser pulses. The periodicity of the LIPSSs was found to be approximately 650 nm, which is comparable to the wavelength of the laser ablating the silver. The concentric nature of these LIPSSs is also quite interesting as one would expect linear LIPSSs when using linearly polarised light. The periodicity being larger than the laser wavelength is also surprising since the period of the LIPSSs should be lower than the laser wavelength even for LSFLs, although LIPSSs with a period larger than the wavelength have been reported when the number of pulses is relatively high [80].

4.2 Silver Oxide Dependency on Pulse Energy and Number of Pulses

To find the threshold in terms of number of pulses and pulse energy to start detecting Ag_2O and AgO using Raman spectroscopy, laser dot matrices were machined on bulk silver samples, as described in section 3, with each column representing a number of pulses and each row being machined with different laser pulse energies. The laser-machined silver sample is then brought to a Raman microscope to analyse the chemical composition of each machined crater as well as their surrounding area. Typically, it takes from 10 to 15 minutes to start performing Raman scans. It is important to start the chemical analysis as soon as possible due to the tendency of AgO to decompose at room temperature (see section 2.1.3). A few of those Raman scans are shown in figures 4.3 to 4.6. In these figures, the distribution of Ag_2O and AgO is shown, as well as a brightfield image of the crater in question and an example of Raman spectra of both Ag_2O and AgO. The brightfield images typically show a dark area, the crater itself, at the center (I), a dark grey area near the crater (II) which becomes lighter farther away from the crater (III), then a blue ring (IV) and finally a brown ring (V). Table 4.1 shows the parameters used for these experiments.

# of pulses	1	3	10	30	100	300	1000	3000	10000
Pulse energy [µJ] (after microscope objective)	0.21	0.42	1.05	2.1	3.15	4.2	6.3	8.4	(max power)

Table 4.1: Laser machining parameters to find silver oxide thresholds.

Figure 4.7 shows the distribution of detected silver oxides over the parameters tested. It was found that both silver oxides would start appearing when certain parameters were reached. Both an increase in pulse energy and number of pulses lead to formation of both oxides. However, each oxide starts appearing at distinct laser parameters. Generally, a higher total laser fluence will form AgO while still forming Ag_2O, and lowering the laser fluence, either by decreasing the total number of pulses or lowering the pulse energy, will

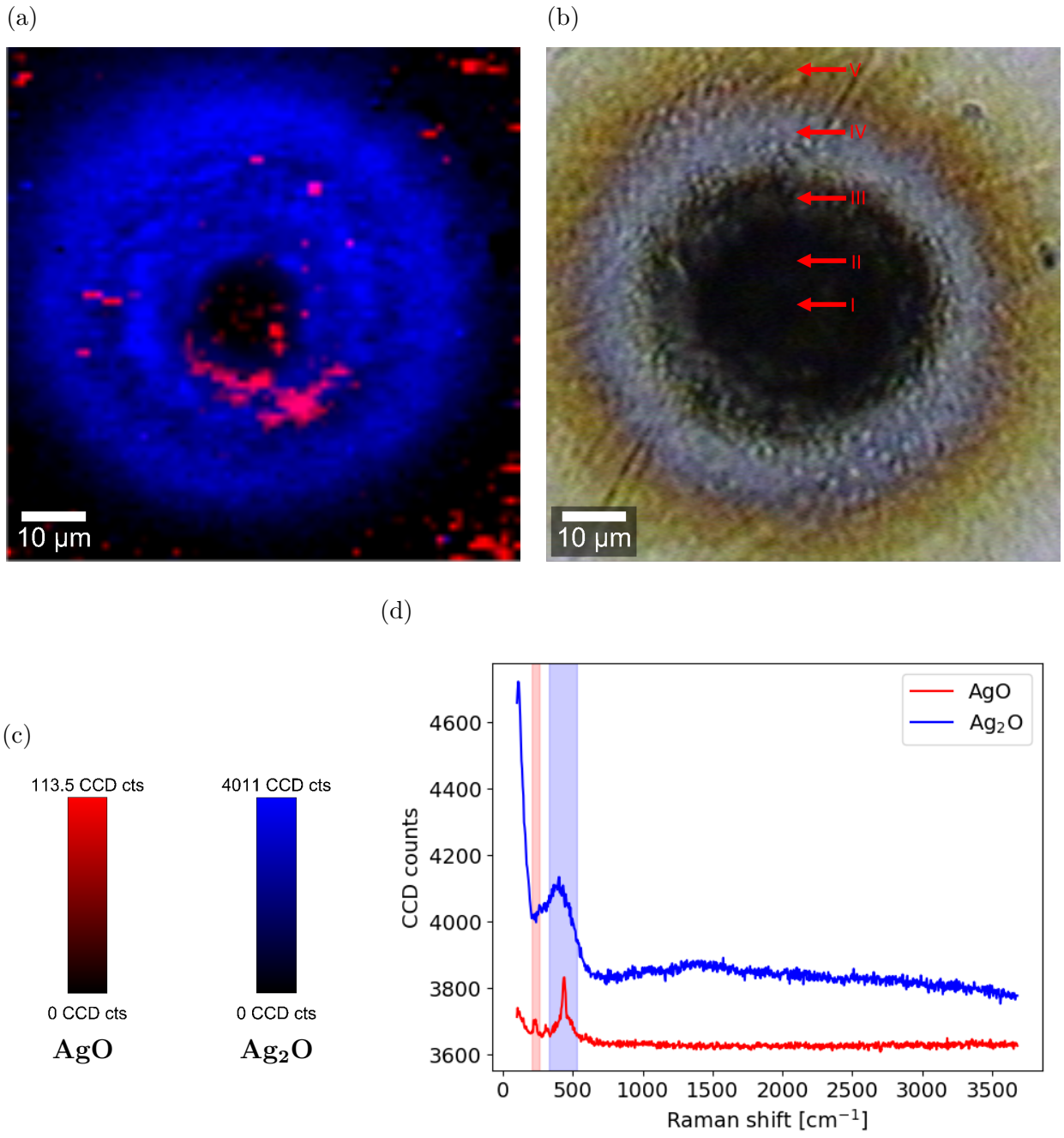

Figure 4.3: Raman scan of silver oxides, for 8.4 µJ pulse energy and 10000 pulses. (a) Raman scan, (b) corresponding brightfield image, (c) scale bars for Raman scan, (d) example of Raman spectra found in the scan, along with integrated area shaded in the color respective to the spectra.

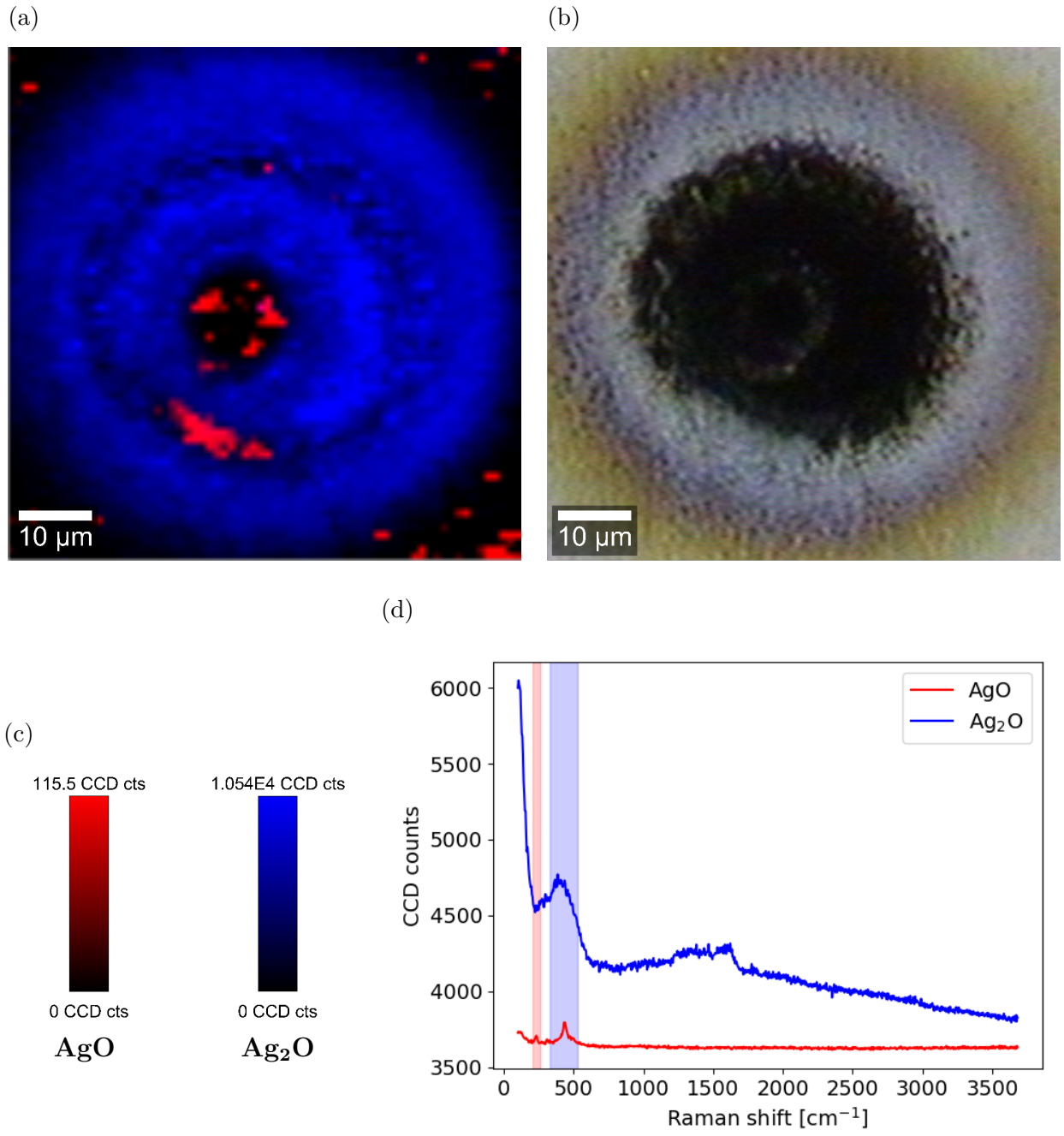

Figure 4.4: Raman scan of silver oxides, for 6.3 µJ pulse energy and 10000 pulses. (a) Raman scan, (b) corresponding brightfield image, (c) scale bars for Raman scan, (d) example of Raman spectra found in the scan, along with integrated area shaded in the color respective to the spectra.

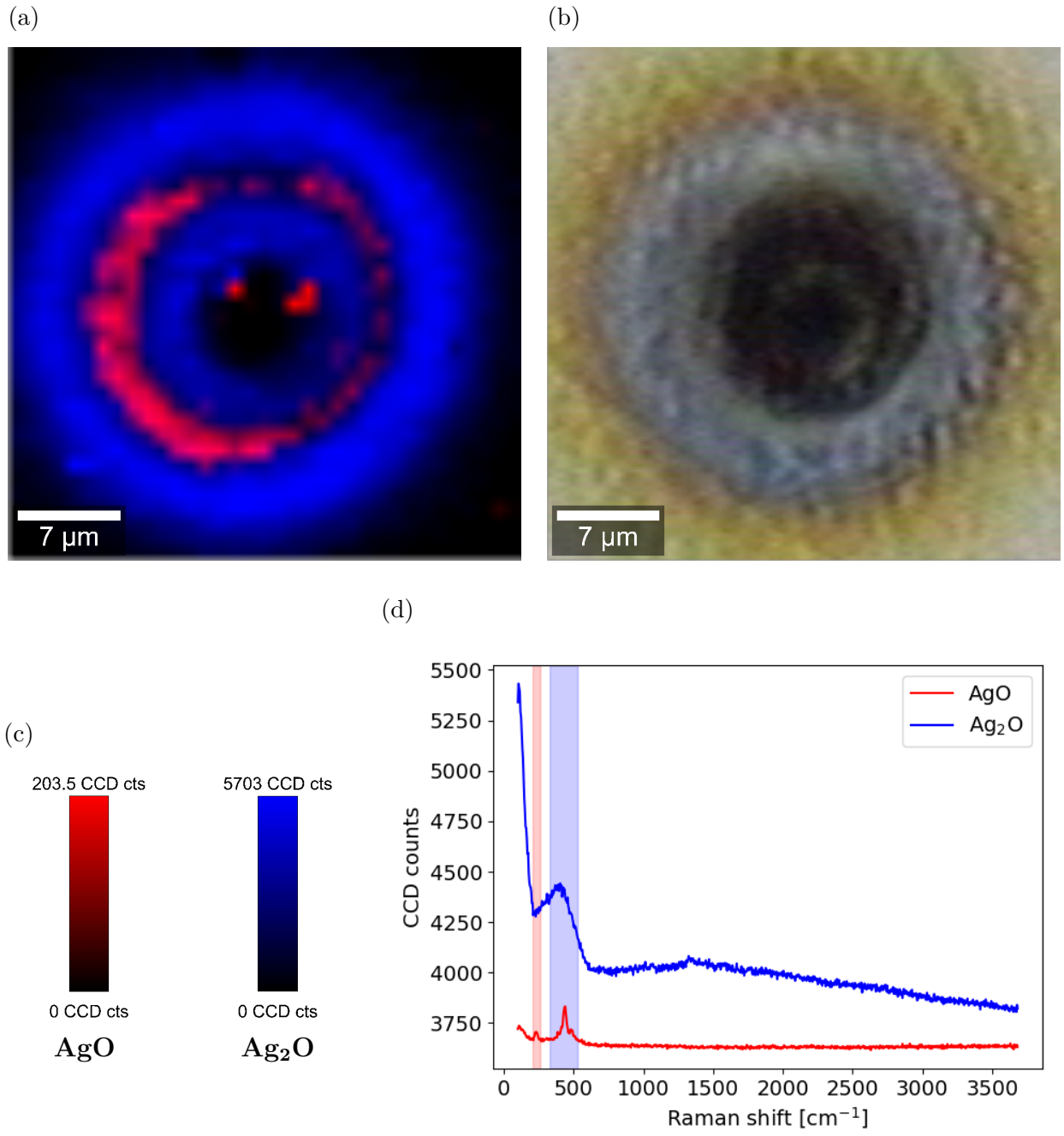

Figure 4.5: Raman scan of silver oxides, for 1.05 µJ pulse energy and 10000 pulses. (a) Raman scan, (b) corresponding brightfield image, (c) scale bars for Raman scan, (d) example of Raman spectra found in the scan, along with integrated area shaded in the color respective to the spectra.

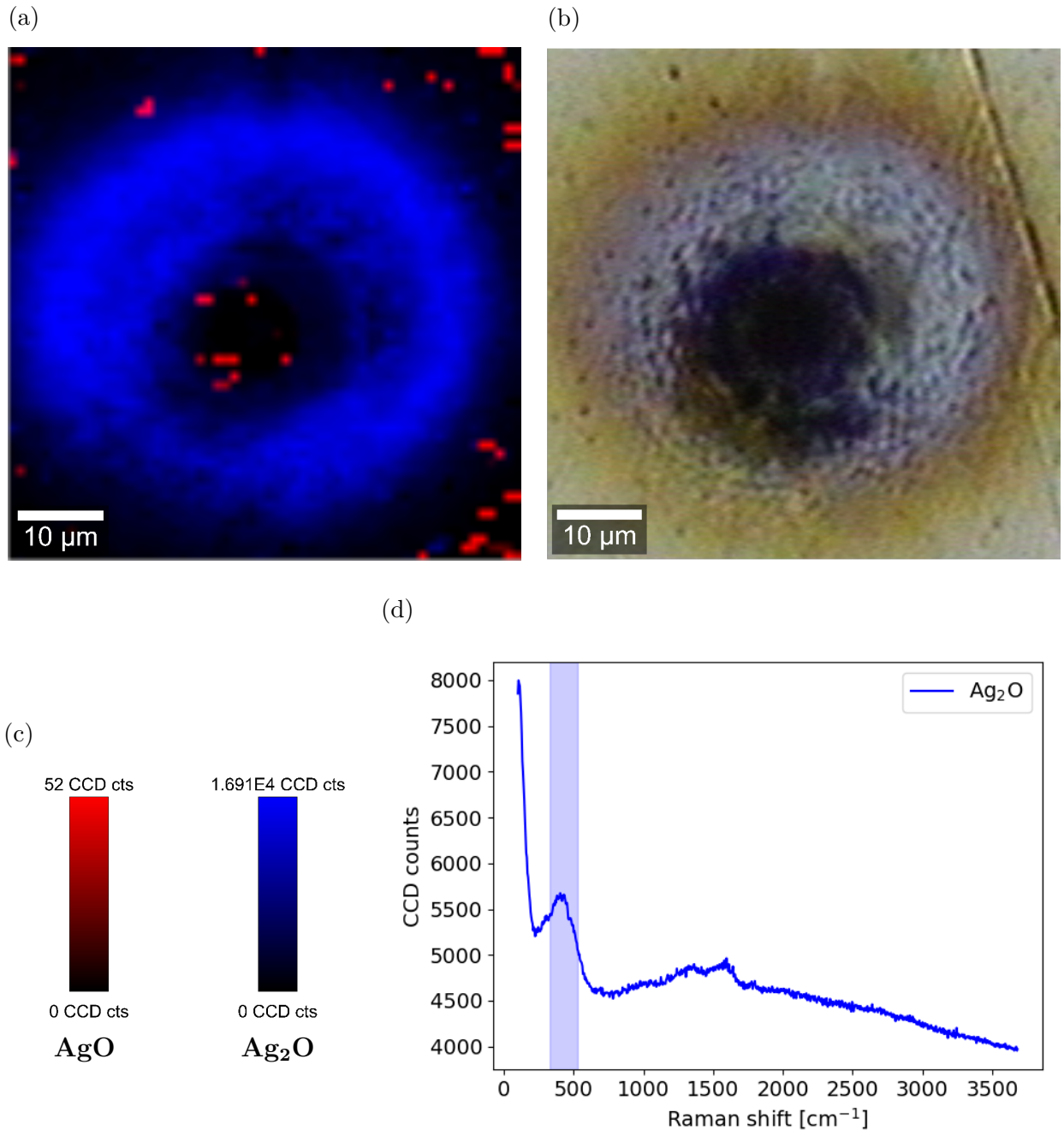

Figure 4.6: Raman scan of silver oxides, for 8.4 µJ pulse energy and 300 pulses. (a) Raman scan, (b) corresponding brightfield image, (c) scale bars for Raman scan, (d) example of a Raman spectrum found in the scan, along with the integrated area shaded.

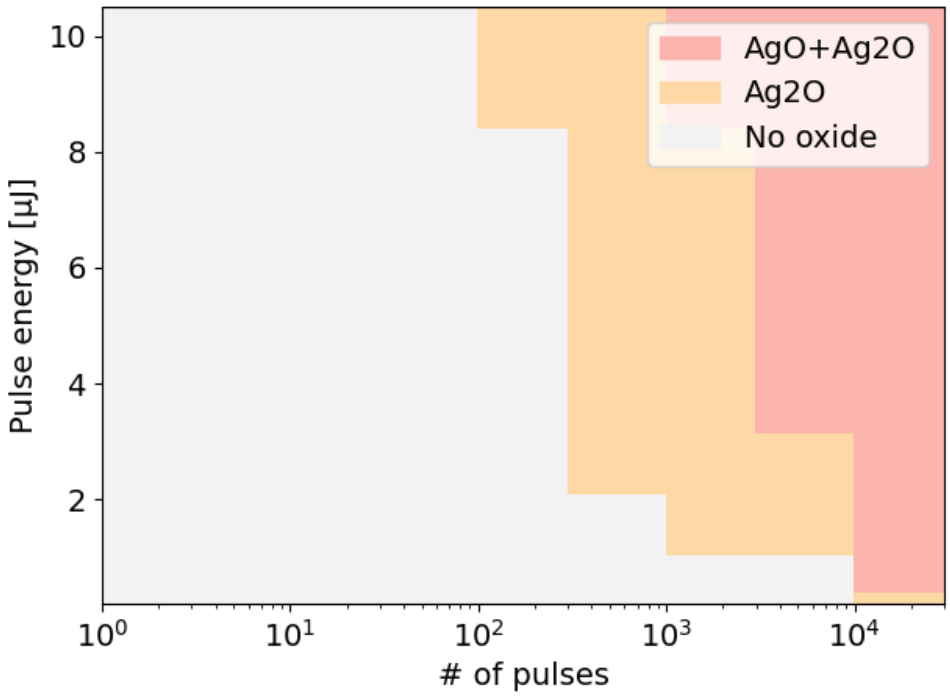

Figure 4.7: Silver oxides distribution for laser parameters tested. Higher pulse energies and higher number of pulses tend to favor the formation of silver oxides.

decrease the formation of AgO until only Ag_2O remains.

4.2.1 Ag_2O Formation

According to figure 4.7, Ag_2O starts forming at a moderately high total laser fluence but remains even at a high laser fluence. The minimum laser fluence required to get Ag_2O ranges from 20 kJ/cm^2 to 67 kJ/cm^2. In cases where both oxides appear, Ag_2O is detected close to and far from the crater, as shown in figures 4.3 to 4.6. In the laser machined crater, no Ag_2O is detected, however this could be due to the crater being too deep for the signal to be detected. The laser does not directly ablate the area on which the Ag_2O is found, meaning the oxide must be mostly redeposited material, and the silver must be oxidising as it is getting ablated and ejected in the air or evaporated. Since the Ag_2O must be redeposited material, it should be expected that some of the material will return to the laser machined crater.

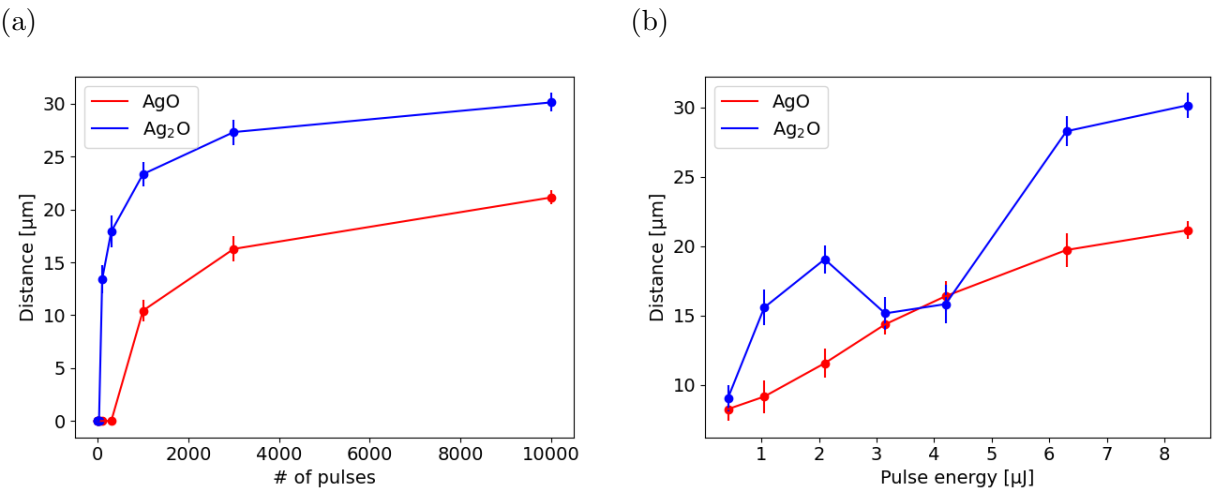

Figure 4.8: Distance of Ag_2O found furthest from the center of the laser machined dot with respect to (a) number of pulses, keeping the pulse energy at 8.4 µJ and (b) pulse energy, keeping the number of pulses at 10000.

In addition to the oxide content being modified by the laser parameters, the size of the crater as well as the redeposited material are generally affected by the total fluence; increasing the number of pulses and the pulse energy slightly increases the size of the crater and greatly increases the maximum distance from the crater for which material gets redeposited. Ag_2O makes up a significant portion of the redeposited material in most cases where the radius becomes larger than the diameter of the crater. Figure 4.8 shows the relationship between the number of pulses or the pulse energy and the maximum distance at which Ag_2O is found from the center of the laser machined crater. This data was taken from another set of experiments where matrices of dots were machined, with the number of shots and the pulse energy being the varied parameters. For this set of experiments, Raman images were taken for a horizontal thin cross-section of the craters to save time.

The Ag_2O distance seemingly scales logarithmically with the number of pulses. This data indicates that the more the silver surface gets ablated, the more redeposited Ag_2O is present on the surface. It is also worth mentioning that since the size of the crater increases as well, and no silver oxide is typically detected in the crater, the radius at which silver oxides start appearing also increases. Regarding the dependence of Ag_2O distance with

pulse energy, figure 4.8b shows that a higher pulse energy increases the maximum distance at which Ag_2O appears, however a few points do not follow this trend. It is not clear as to why these points do not follow the trend, however scans for the laser machined craters from which these data points originate from are shown in appendix B and are clearly unusual when compared with other similar scans (e.g. figures 4.3 to 4.5). Figures 4.3 to 4.5 show an interesting phenomenon when laser machining dots using many pulses: there is a ring centered on the crater where the Raman signal from Ag_2O is lower, around halfway between where the Ag_2O starts and finishes. This will be discussed further in section 4.2.2, where the formation of AgO from this set of experiments is studied.

The brightfield images of figures 4.3 to 4.6 show many rings of different colors. In all cases where silver oxides are present as redeposited material, there is a dark circle surrounding the crater, which becomes brighter, then a greyish-blue ring surrounds the area, followed by a brown circle at the outermost region. These regions are labeled as II, III, IV and V in figure 4.3. It is easy to relate Ag_2O content to redeposited material color; most of the Ag_2O appearing on these sample coincide quite well with the outer brown circle from the brightfield image. The circular area of low-Ag_2O signal could also be related to the blue area from the brightfield image. The radius of the brown circles also match the maximum radius of redeposited Ag_2O shown in figure 4.8. It is also worth mentioning that some Ag_2O signal appear in the dark area near the crater.

4.2.2 AgO Formation

Figure 4.7 shows that AgO starts forming when the laser fluence is generally high. The laser fluence required according to this figure ranges from 134 kJ/cm^2 to 668 kJ/cm^2 depending on the pulse energy and number of pulses combination. There is also always Ag_2O alongside AgO when laser machining dots with many pulses or with high pulse energy. As shown by the red regions in figures 4.3 to 4.6, AgO appears much closer to the laser machined craters and covers a much smaller area than Ag_2O. Like Ag_2O, AgO does not typically get detected

in the crater for presumably similar reasons as discussed in section 4.2.1.

It is interesting that AgO starts appearing at higher laser fluences only, and that it always appears alongside Ag_2O. This may suggest that both oxides get created at the same time when laser machining at high fluence or that AgO gets created from the Ag_2O already on the surface when machining with a high number of pulses.

Another interesting fact is that the location of the AgO around the laser machined craters coincides very well with the locations of the low-Ag_2O locations. AgO start appearing at a slightly smaller radius than this low-Ag_2O signal circle. The AgO around the crater sometimes does and sometimes does not form a complete circle (see figure 4.5 compared to figures 4.3 and 4.4). The radius of the AgO ring (and the area with less Ag_2O) scales similarly to the size of the Ag_2O area described in section 4.2.1. It scales in a logarithmic manner with the number of pulses for a pulse energy of 8.4 µJ, and it increases with the pulse energy when keeping the number of pulses at 10000.

Contrary to Ag_2O, the colors from the brightfield images in figures 4.3 to 4.6 do not show a clear correlation between colors and AgO presence. While AgO does appear near the dark regions close to the crater, it does not appear everywhere in these regions. This makes it difficult to find a relation between redeposited material color and AgO content.

4.3 Silver Oxide Dependency on Wavelength

Section 4.2 describes a set of experiments to find the threshold parameters for the presence of silver oxides near laser machined craters. This section aims to explain the effects of laser machining wavelength on these thresholds. Also, the BBO crystal must be removed from the laser path to get the 1030 nm wavelength, which means the maximum power that can be used is much greater. The focus needs to be slightly adjusted to take into account the different optics (see figure 3.7). Table 4.2 shows the parameters used for these experiments.

For these experiments, the minimum pulse energy tested is 8.4 µJ, which is equal to

# of pulses	1	3	10	30	100	300	1000	3000	10000
Pulse energy [µJ] (after microscope objective)	8.4	12.6	16.8	21	25.2	29.4	33.6	37.8	(max power)

Table 4.2: Laser machining parameters to find silver oxide thresholds, without BBO crystal.

the second-highest pulse energy in the experiment described in section 4.2. These two experiments are compared to assess the effect of laser wavelength on laser-induced chemical reactions. Figures 4.9 and 4.10 show the equivalent experiments as figures 4.3 and 4.6, the only parameter changed being the wavelength of the laser. Here, the 10000 pulses case, which contains AgO and Ag_2O, and the 300 pulses case, which only contains Ag_2O, are compared for a machining wavelength of 515 nm and 1030 nm.

For similar powers, the threshold parameters do not change significantly, but there are still a few differences. Comparing figures 4.7 and 4.11 shows that Ag_2O starts forming at approximately 100 pulses when machining with a 8.4 µJ pulse energy no matter the wavelength, however AgO starts forming at 1000 pulses in the 515 nm laser case (in low amounts) while it took 3000 pulses to start forming it for the 1030 nm laser case. This is not a big difference; however, it is still worth keeping in mind.

The following observations remain true for both laser wavelengths: there are thresholds of pulse energy and number of pulses at which AgO and/or Ag_2O start appearing, AgO will not appear alone from laser machining and is always accompanied by Ag_2O, both oxides that are detected by Raman spectroscopy are almost exclusively from redeposited material, increasing the number of pulses will increase the maximum distance from the crater at which AgO and Ag_2O appear and there is often a circular region surrounding the crater in which the Raman signal from Ag_2O becomes less intense that coincides quite well with the region in which AgO appears.

The absence of a BBO crystal for this setup allows much higher powers to be used when machining, up to 42 µJ. Figure 4.11 shows the detected oxides for all possible combinations of pulse energies and number of pulses shown in table 4.2. It can be seen as a continuation

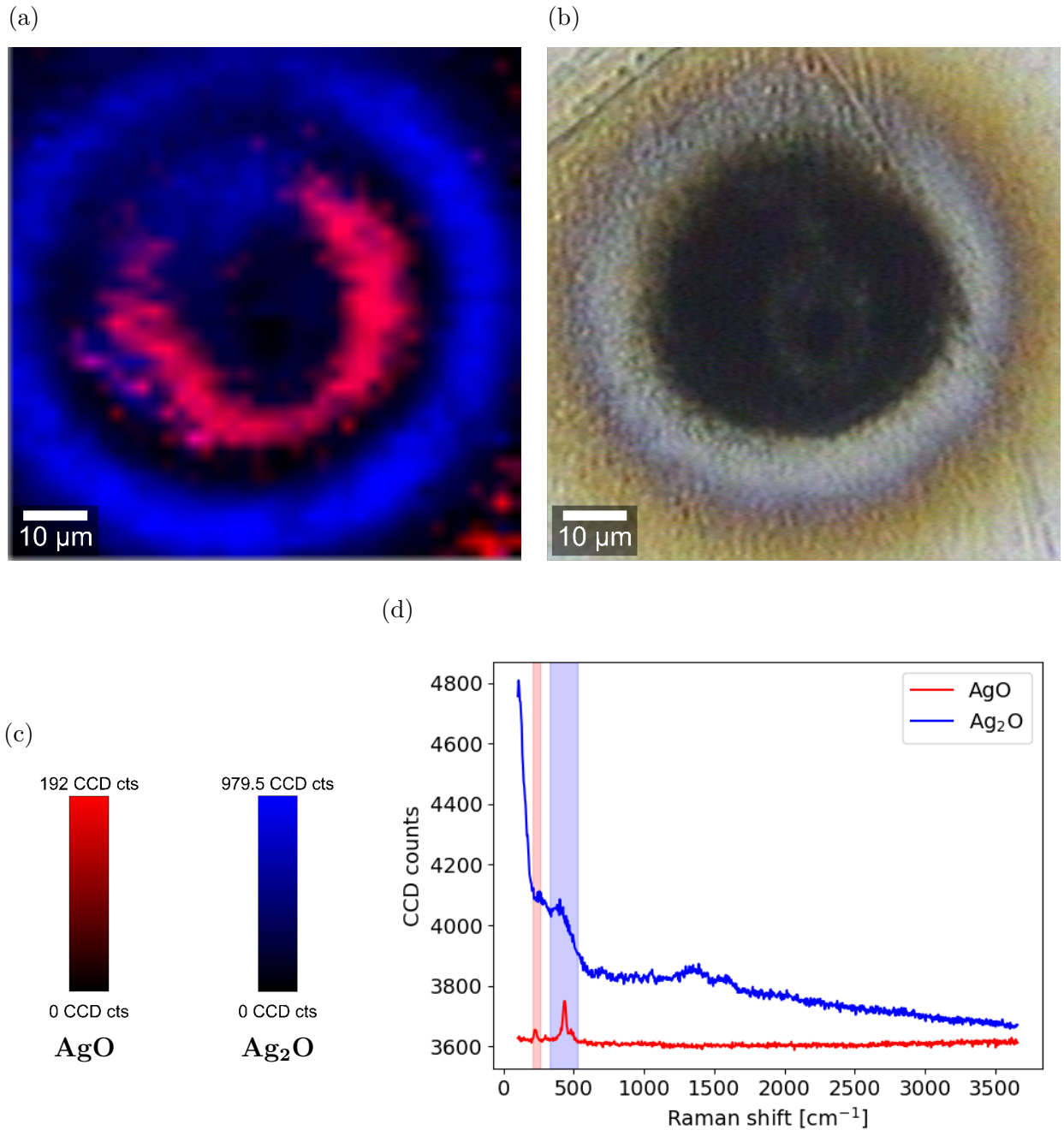

Figure 4.9: Raman scan of silver oxides, for 8.4 µJ pulse energy and 10000 pulses, using a laser wavelength of 1030 nm. (a) Raman scan, (b) corresponding brightfield image, (c) scale bars for Raman scan, (d) example of Raman spectra found in the scan, along with integrated area shaded in the color respective to the spectra.

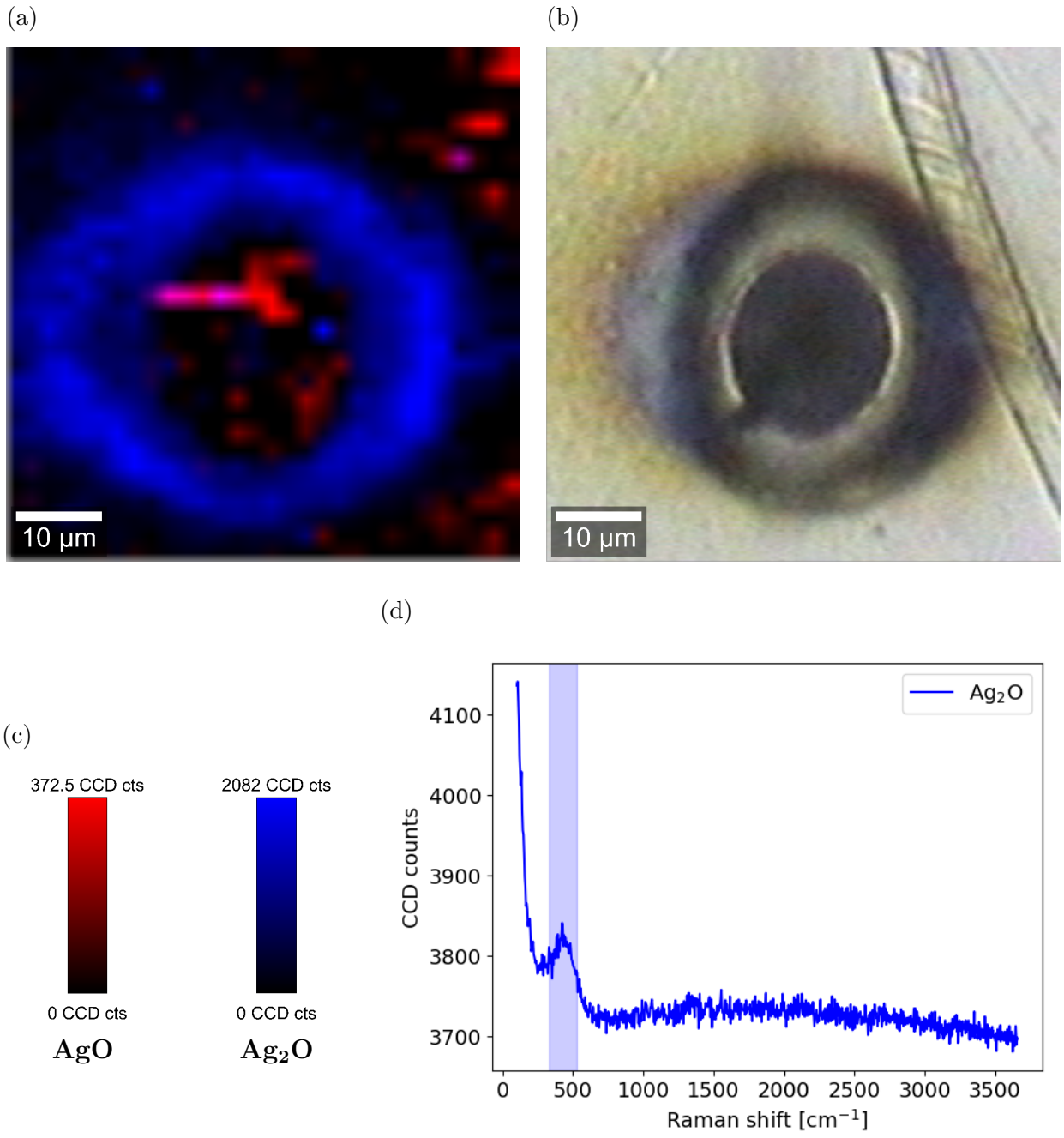

Figure 4.10: Raman scan of silver oxides, for 8.4 µJ pulse energy and 300 pulses, using a laser wavelength of 1030 nm. (a) Raman scan, (b) corresponding brightfield image, (c) scale bars for Raman scan, (d) example of a Raman spectrum found in the scan, along with the integrated area shaded.

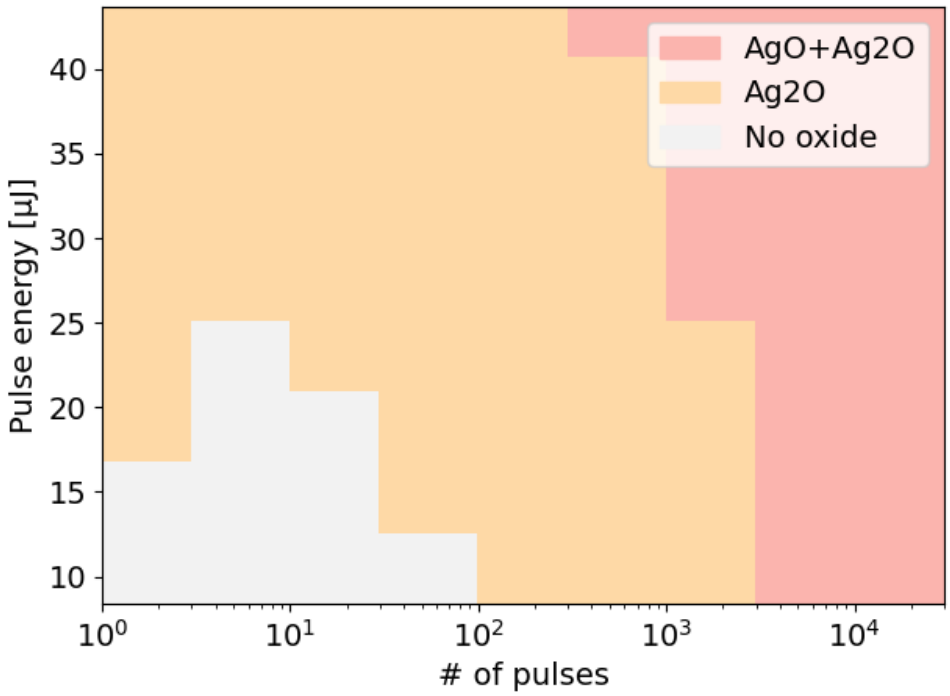

Figure 4.11: Silver oxides distribution for laser parameters tested. Higher pulse energies and higher number of pulses tend to favor the formation of silver oxides. The wavelength used is 1030 nm.

of figure 4.7, although there are discontinuities in the threshold to get AgO, as mentioned previously. The number of pulses threshold to get AgO also gets to 300 pulses for very high pulse energy (the maximum pulse energy provided by the laser).

Figures 4.12 to 4.14 show scans for laser-machined dots with higher powers. The number of pulses is 1000 in all three cases, since the size of the area covered in redeposited material becomes too large for the Raman microscope scan area in the 3000 and 10000 pulses at high pulse energies. This is already the case for figure 4.14, however the relevant features were captured in this case; namely there is negligible signal in the crater itself, there is a Raman signal attributed to AgO, which coincides with a lack of Ag_2O signal (in the top right of the Raman scan) and Ag_2O is typically found farther from the crater than AgO.

The redeposited material's center deviates from the laser machined crater for very high pulse energies and very high pulse counts. This is most likely simply due to the fume

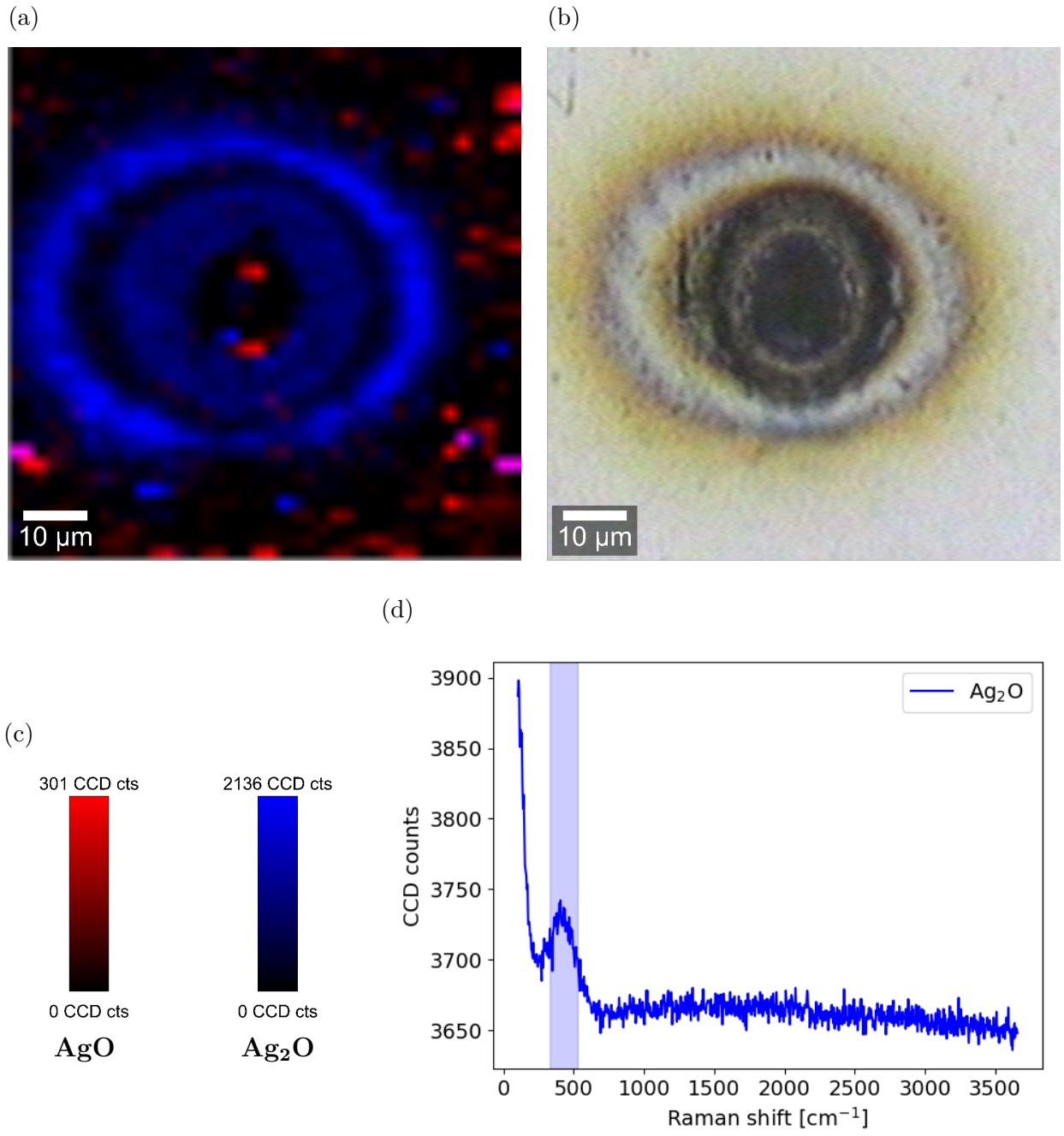

Figure 4.12: Raman scan of silver oxides, for 8.4 µJ pulse energy and 1000 pulses, using a laser wavelength of 1030 nm. (a) Raman scan, (b) corresponding brightfield image, (c) scale bars for Raman scan, (d) example of a Raman spectrum found in the scan, along with the integrated area shaded.

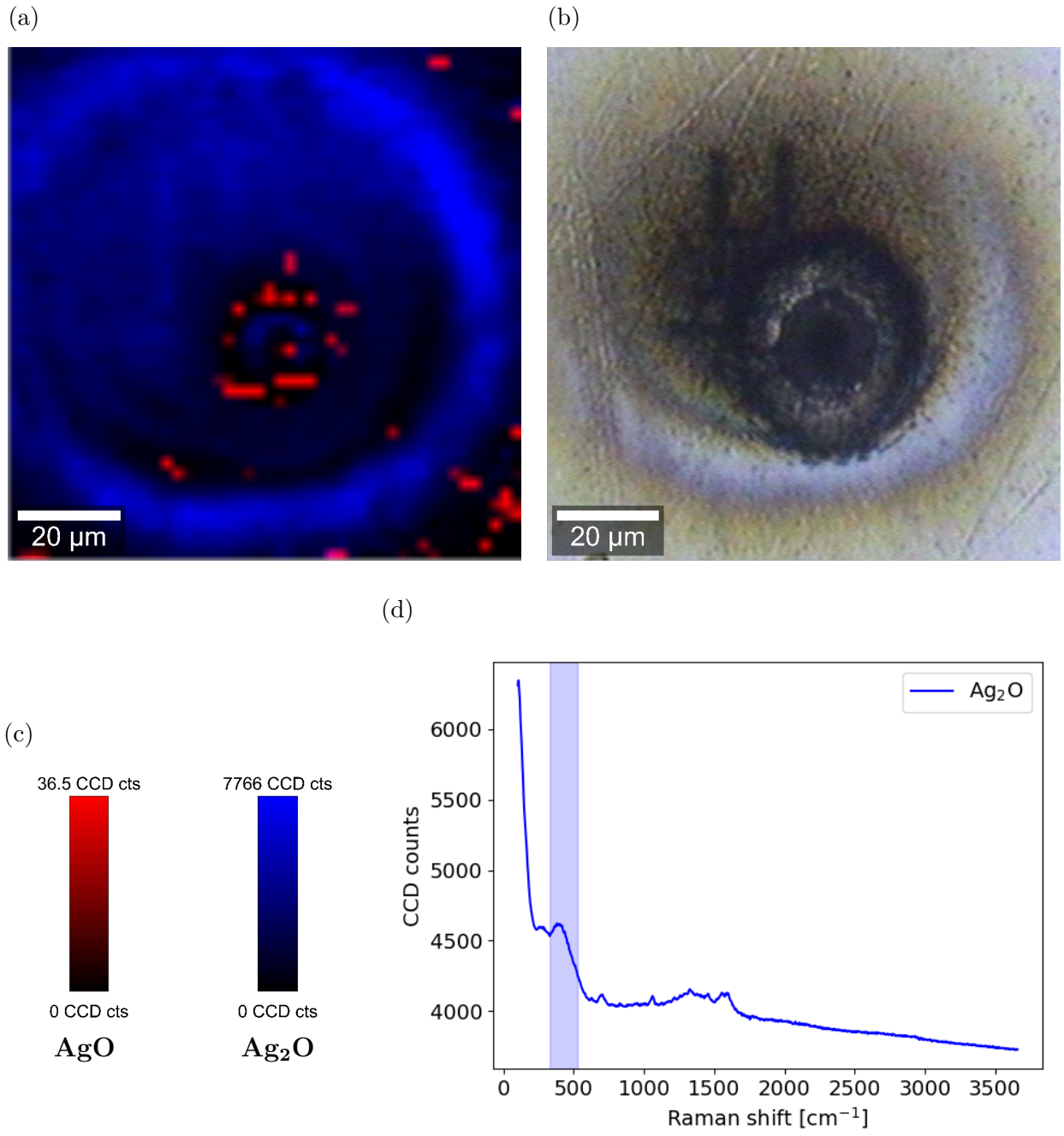

Figure 4.13: Raman scan of silver oxides, for 25.2 µJ pulse energy and 1000 pulses, using a laser wavelength of 1030 nm. (a) Raman scan, (b) corresponding brightfield image, (c) scale bars for Raman scan, (d) example of a Raman spectrum found in the scan, along with the integrated area.

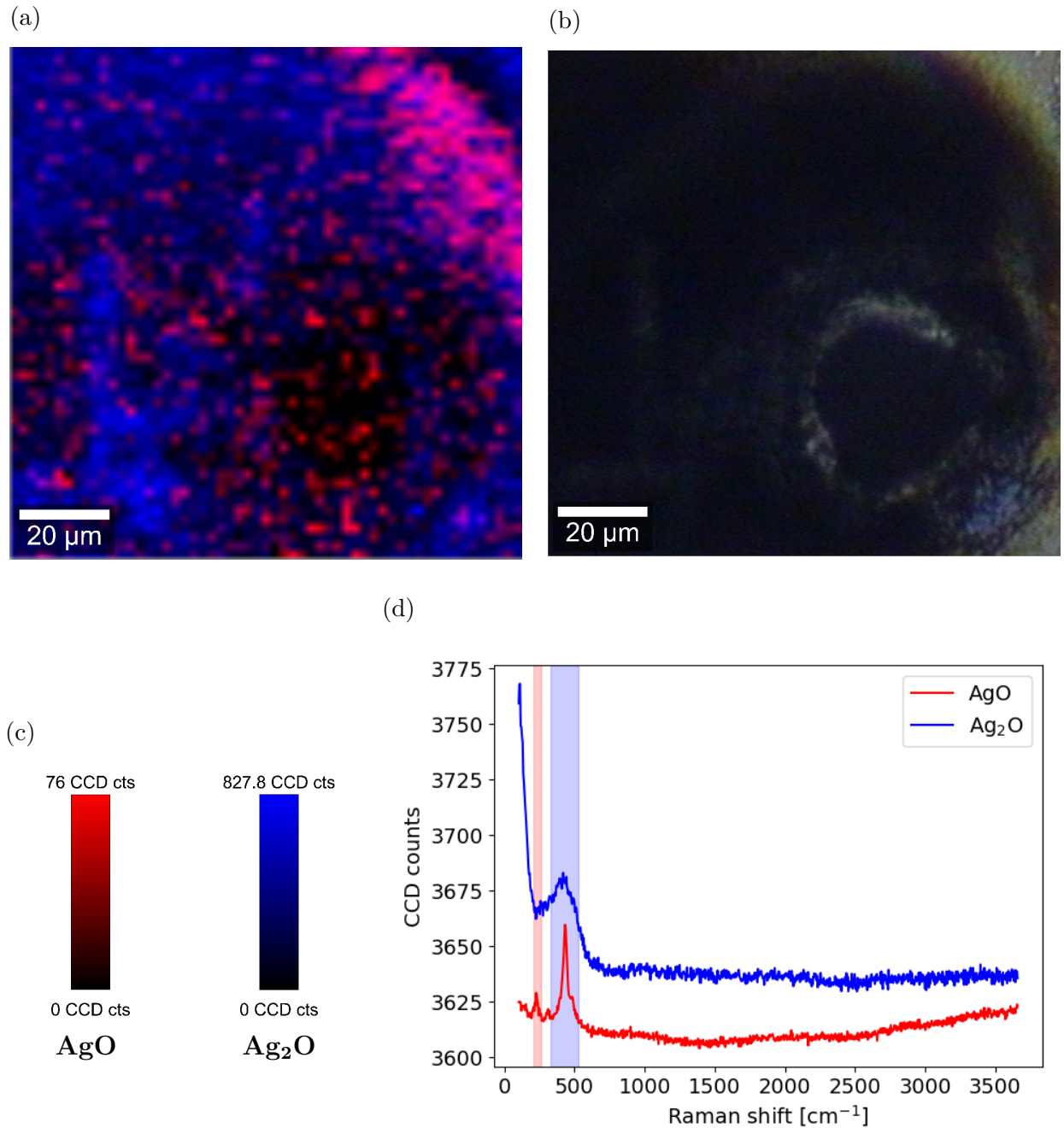

Figure 4.14: Raman scan of silver oxides, for 37.8 µJ pulse energy and 1000 pulses, using a laser wavelength of 1030 nm. (a) Raman scan, (b) corresponding brightfield image, (c) scale bars for Raman scan, (d) example of Raman spectra found in the scan, along with integrated area shaded in the color respective to the spectra.

extractor removing fumes which also displaces the laser machining products in the air before being redeposited. The redeposited material center is always on the right and slightly above the crater when looking at brightfield images of the machined dots. This is mostly apparent in figures 4.13 and 4.14 because of the higher pulse energies ejecting more silver into the air. It follows that one must take the effect of the fume extractor into consideration when studying the oxides appearing from laser machining.

Figures 4.9 to 4.14 often show dark straight lines, which also show up in the corresponding Raman scans. These lines appear from the laser irradiating the sample when pre-emptively looking at the sample to make sure the laser power is not too high before scanning the sample. Figure 4.13 also shows small peaks at roughly 700 cm^{-1} and 1070 cm^{-1}. Both these points are discussed further in section 5.

While it is interesting that, according to Fig. 4.11, Ag_2O may be formed from single-shot or very low number of pulses, it should be mentioned that the amount of Ag_2O found in these cases is very small and that next to no redeposited material is seen in brightfield images.

4.4 Silver Oxide Dependency on Repetition Rate

To get a better understanding on the AgO formation process, a dot matrix with varying repetition rate and number of pulses was machined. A sketch of the experiment is shown in figure 4.15. The goal is to see whether the time between each pulse affects the number of pulses threshold to start forming AgO. The repetition rates as well as numbers of pulses used are listed in table 4.3. The laser wavelength and pulse energy used for every dot are 515 nm and 7.14 µJ respectively. To keep pulse energy the same, the power needed to be adjusted for each repetition rate. For example, to keep the same pulse energy between a 10 kHz repetition rate and a 1 kHz repetition rate, the power should be 10 times higher in the 10 kHz case than in the 1 kHz case. Since the laser power cannot go over 5500 mW, repetition rates over 30 kHz will have lower pulse energies, meaning pulse energies cannot

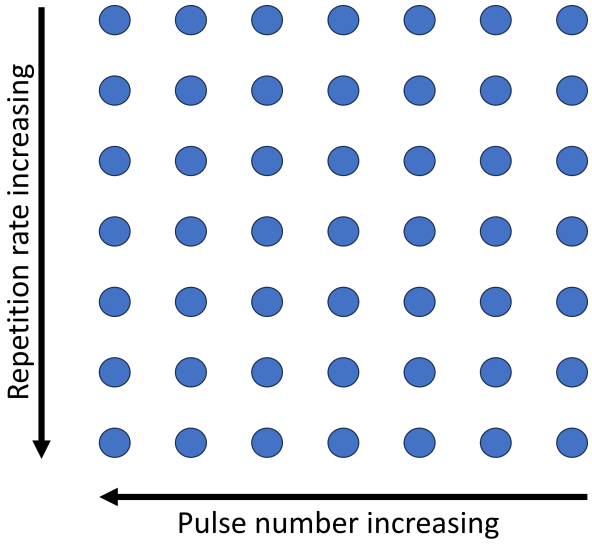

Figure 4.15: Sketch of the repetition rate dot matrix experiment.

# of pulses	1	3	10	30	100	300	1000
Repetition rates (Hz)	1	10	100	500	2500	5000	15000

Table 4.3: Laser machining parameters to study silver oxide thresholds dependence on repetition rate.

be kept as high as for cases at 30 kHz or lower repetition rates.

Figure 4.16 shows the silver oxide thresholds found for the repetition rate experiments. The thresholds are not affected by a change in repetition rate; AgO will be formed on the surface as redeposited material, no matter if the time between pulses is 1 second or 66.67 microseconds, for instance. This suggests that the formation of AgO or Ag_2O as redeposited material is not driven by accumulated heating effects. This also suggests that a certain amount of Ag_2O must be present on the surface for AgO to start forming by laser machining. A series of experiment done to test this hypothesis is described in section 4.5. It is possible that accumulated effects may have a role at much higher repetition rates, however the highest repetition rate available without affecting pulse energy is 30 kHz.

Figure 4.17 shows the furthest distance from the center of the crater at which redeposited Ag_2O is found. It is not affected by the repetition rate, meaning that in addition to the thresholds not being affected by repetition rate, the redeposited oxide distribution around

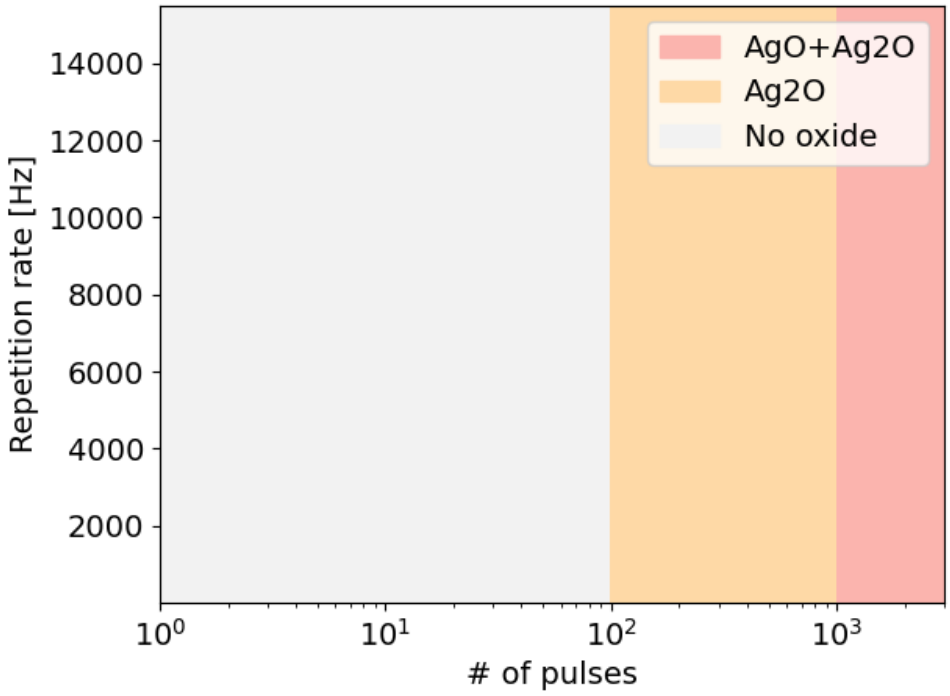

Figure 4.16: Silver oxides distribution for laser parameters tested. Formation of silver oxides is not dependent on repetition rate. The laser wavelength used is 515 nm and the pulse energy is 7.14 µJ.

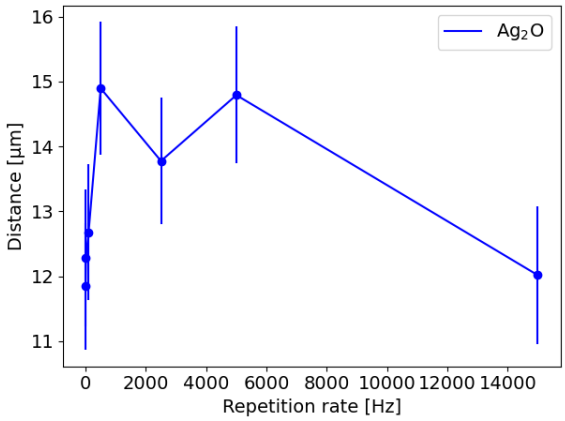

Figure 4.17: Distance of Ag_2O found furthest from the center of the laser machined dot with respect to repetition rate, keeping the number of pulses at 300.

the crater is not affected either. Figures 4.18 and 4.19 show the similarities between the redeposited material from the 15 kHz dot and the 1 Hz dot.

4.5 Laser Machining on Ag_2O

In the previous section (4.4), it was found that repetition rate does not affect the threshold at which AgO or Ag_2O forms. This could mean that AgO only starts forming when there is a certain amount of Ag_2O present on the surface, which would undergo a chemical reaction from laser machining forming AgO. To confirm this hypothesis, two arrays of dots were laser machined at a wavelength of 515 nm, a repetition rate of 5000 Hz and a pulse energy of approximately 9.66 µJ. One array had its number of pulses varied from 400 pulses to 1000 pulses, and the other array was kept at a constant number of pulses (300 pulses). These parameters were chosen since the first array mentioned should contain the threshold to start forming AgO. Both arrays were then studied via Raman spectroscopy. For the first one, Raman scans were done to find the threshold to form AgO, and for the second one, the Raman spectra were quickly looked at to make sure there was Ag_2O as expected from previous experiments. Spots with numbers of pulses ranging from 100 to 700 pulses were machined directly over the 300 pulses dots from the second array, then the second array was

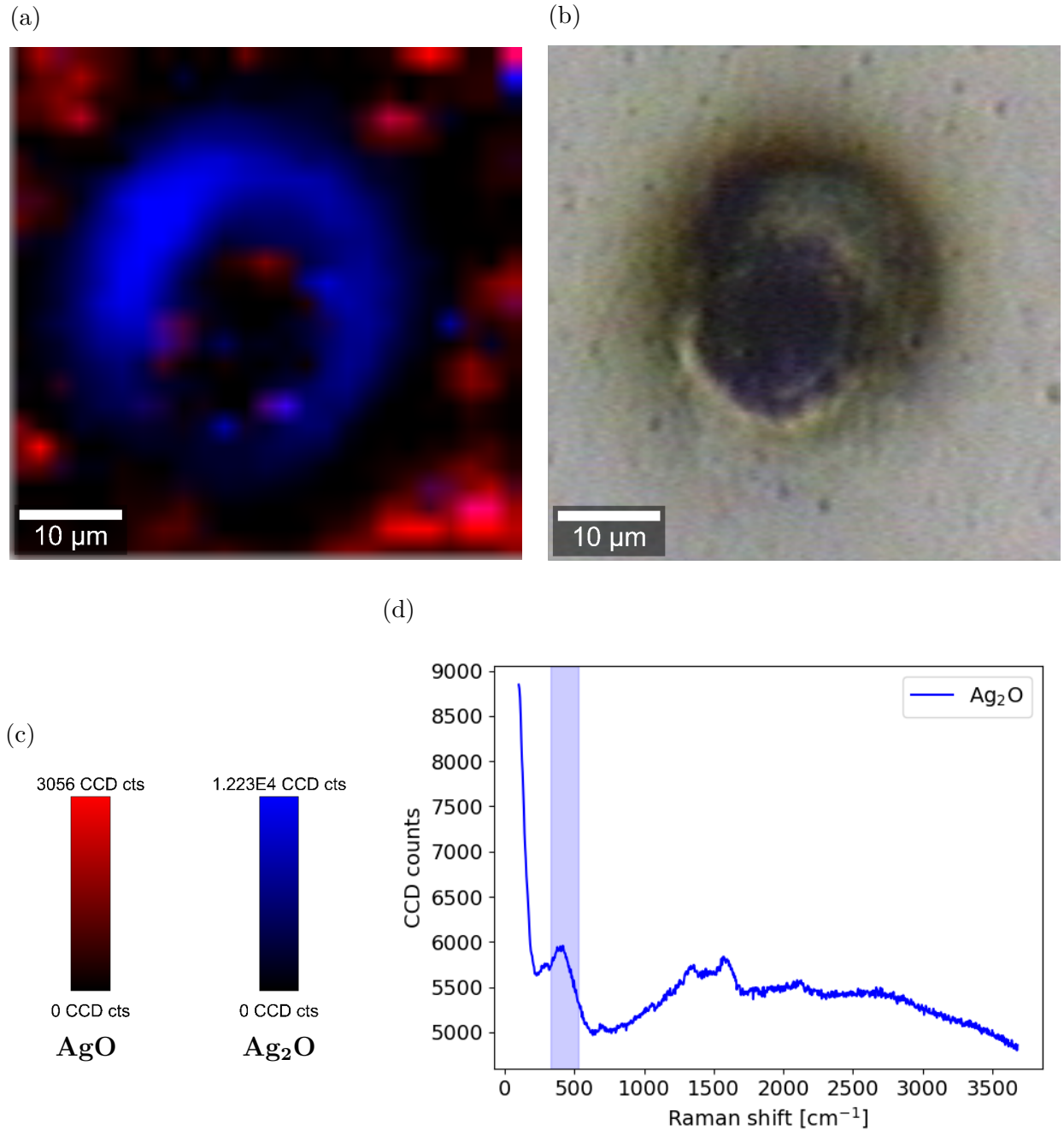

Figure 4.18: Raman scan of silver oxides, for 7.14 µJ pulse energy, 300 pulses and a repetition rate of 15 kHz. (a) Raman scan, (b) corresponding brightfield image, (c) scale bars for Raman scan, (d) example of a Raman spectrum found in the scan, along with the integrated area shaded.

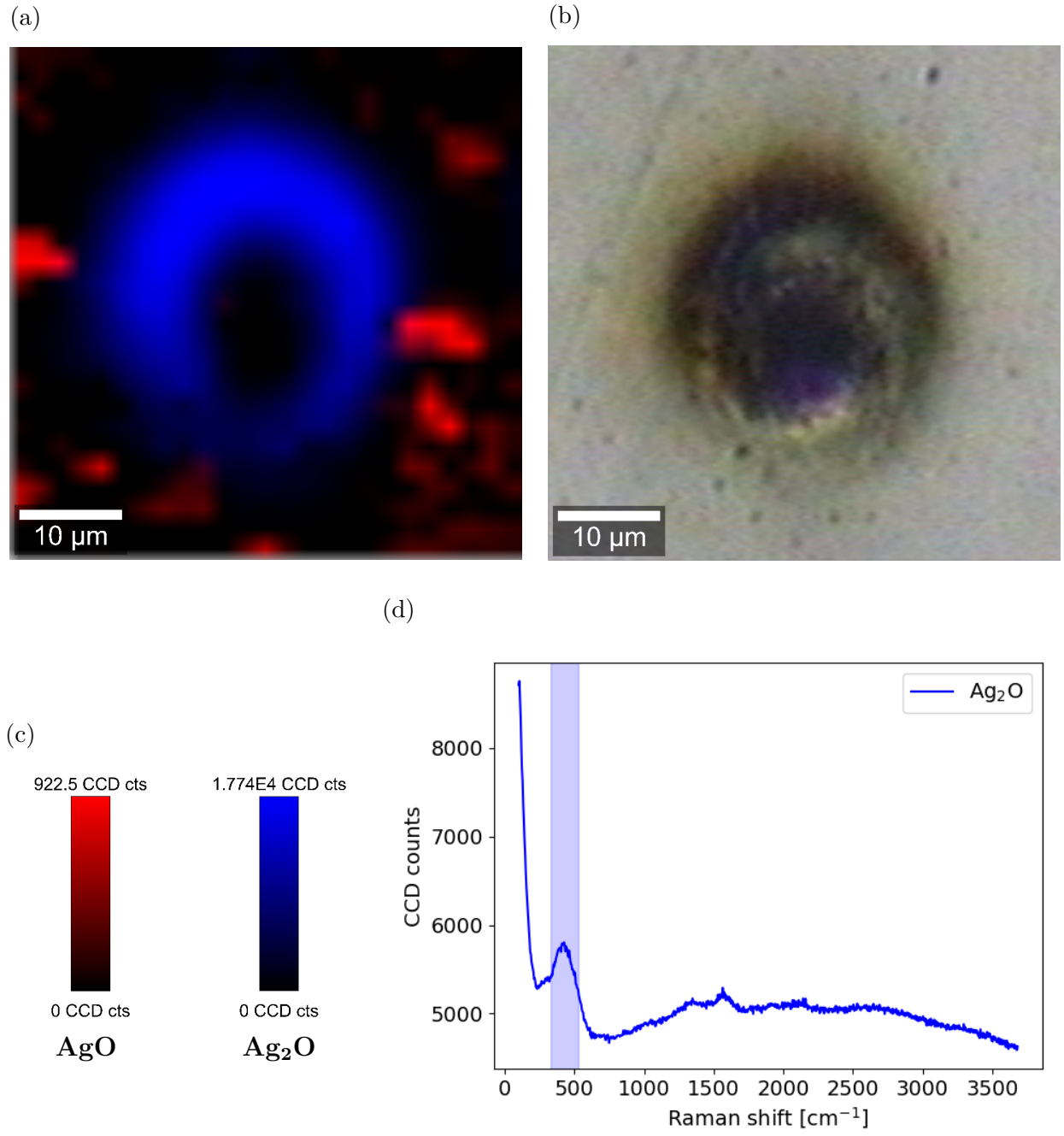

Figure 4.19: Raman scan of silver oxides, for 7.14 µJ pulse energy, 300 pulses and a repetition rate of 1 Hz. (a) Raman scan, (b) corresponding brightfield image, (c) scale bars for Raman scan, (d) example of a Raman spectrum found in the scan, along with the integrated area shaded.

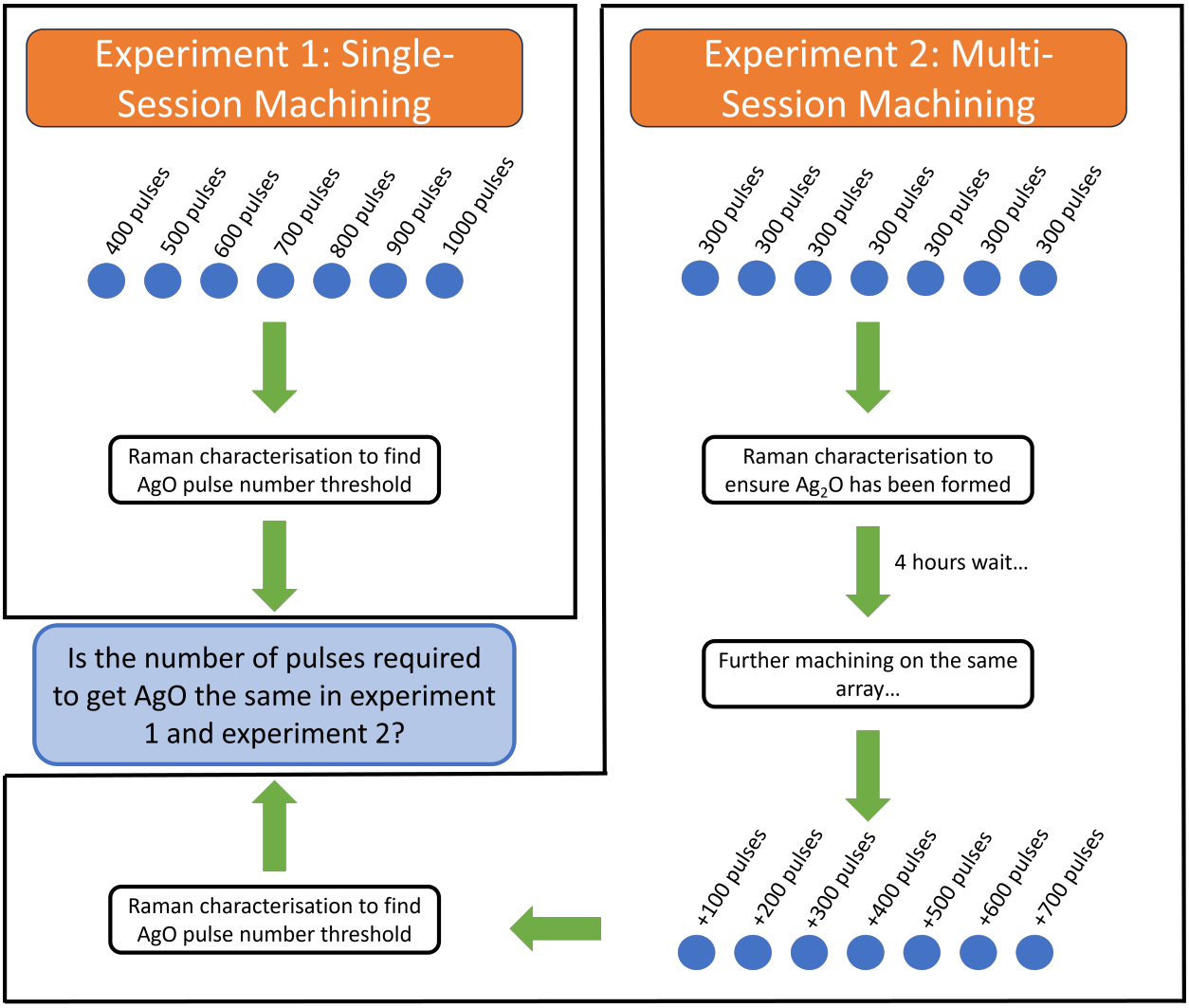

Figure 4.20: Sketch of the dual dot array experiment. The time elapsed between the first machining session and the second machining session in Experiment 2 is approximately 4 hours.

measured again to see at what parameter AgO starts forming. The time between machining sessions is approximately 4 hours. A sketch of the experiment is shown in figure 4.20. Table 4.4 shows the parameters used for this experiment.

It was found from this experiment that the threshold to form AgO for both arrays is 600 pulses in total, and that machining 600 pulses in one session or machining 300 pulses to form Ag_2O then 300 pulses four hours later does not change the oxide composition significantly. This means that the first 300 pulses were forming the Ag_2O as redeposited material, then the next 300 pulses were re-ablating the silver, sending silver and Ag_2O in the air, and the

# of pulses, first array	400	500	600	700	800	900	1000
# of pulses, second array	300 + 100	300 + 200	300 + 300	300 + 400	300 + 500	300 + 600	300 + 700

Table 4.4: Number of pulses of both arrays, in the experiment described in section 4.5. For the second array, the "+" denotes that the sample was measured by Raman spectroscopy to ensure there is Ag_2O between the first number and the second number of pulses (for example, 300+200 pulses means 300 pulses were machined, the machined dot was checked for Ag_2O via Raman spectroscopy, then 200 more pulses were machined directly on the crater).

Ag_2O forms AgO from the laser machining. As more pulses get fired from the laser, silver reacts to become Ag_2O, and further machining turns some Ag_2O into AgO, rather than silver reacting directly to become AgO.

Figures 4.21 and 4.22 show Raman scans for both experiments at a total of 700 pulses. 700 pulses was chosen rather than 600 pulses since the AgO is more easily visible. While the threshold for AgO is similar in both cases, the 300+400 pulses scan show a greater area of Ag_2O. This may be attributed to the Raman scan conditions not being the same since the colour scales for AgO are quite different. Looking at the brightfield images in both cases, the size of the redeposited material area as well as the colors are very similar.

4.6 Summary and Discussion

In summary, it was found that a given threshold in terms of number of pulses and pulse fluence promotes the formation of Ag_2O or AgO. It is always the case that Ag_2O is formed at a lower pulse energy or number of pulses than AgO, and that the AgO is formed from Ag_2O created by previous laser irradiations. This is in agreement with the literature which states that the oxidation of silver into AgO happens in two steps (reactions 2.2 and 2.3) [10, 11]. The formation of silver oxides in ambient air is also reported in literature, albeit using nanosecond lasers in the context of silver oxide fabrication by PLD [35].

The wavelength does not have a significant effect on threshold fluences. For the 515 nm

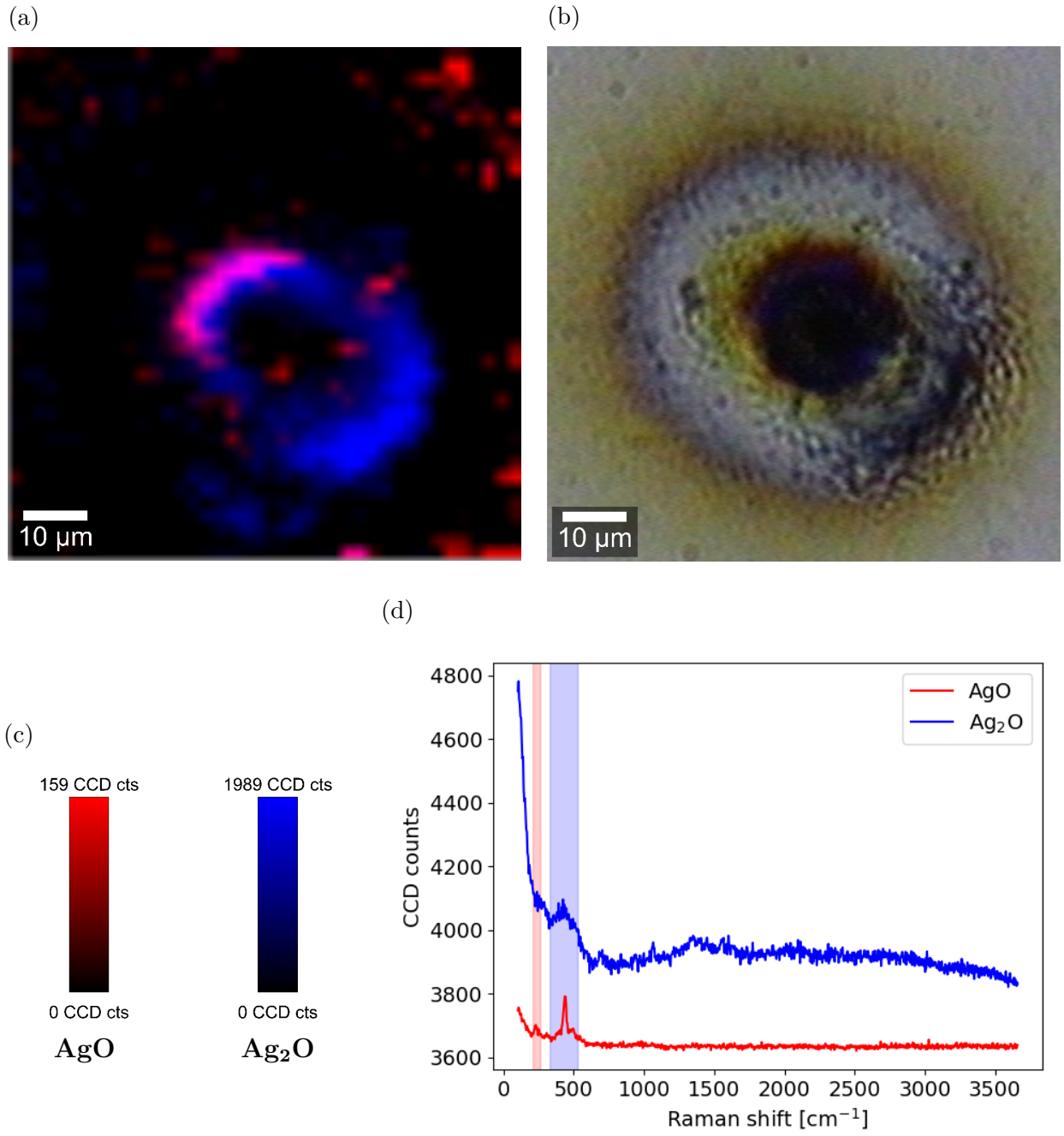

Figure 4.21: Raman scan of silver oxides, for 9.66 µJ pulse energy and 700 pulses. (a) Raman scan, (b) corresponding brightfield image, (c) scale bars for Raman scan, (d) example of Raman spectra found in the scan, along with integrated area shaded in the color respective to the spectra.

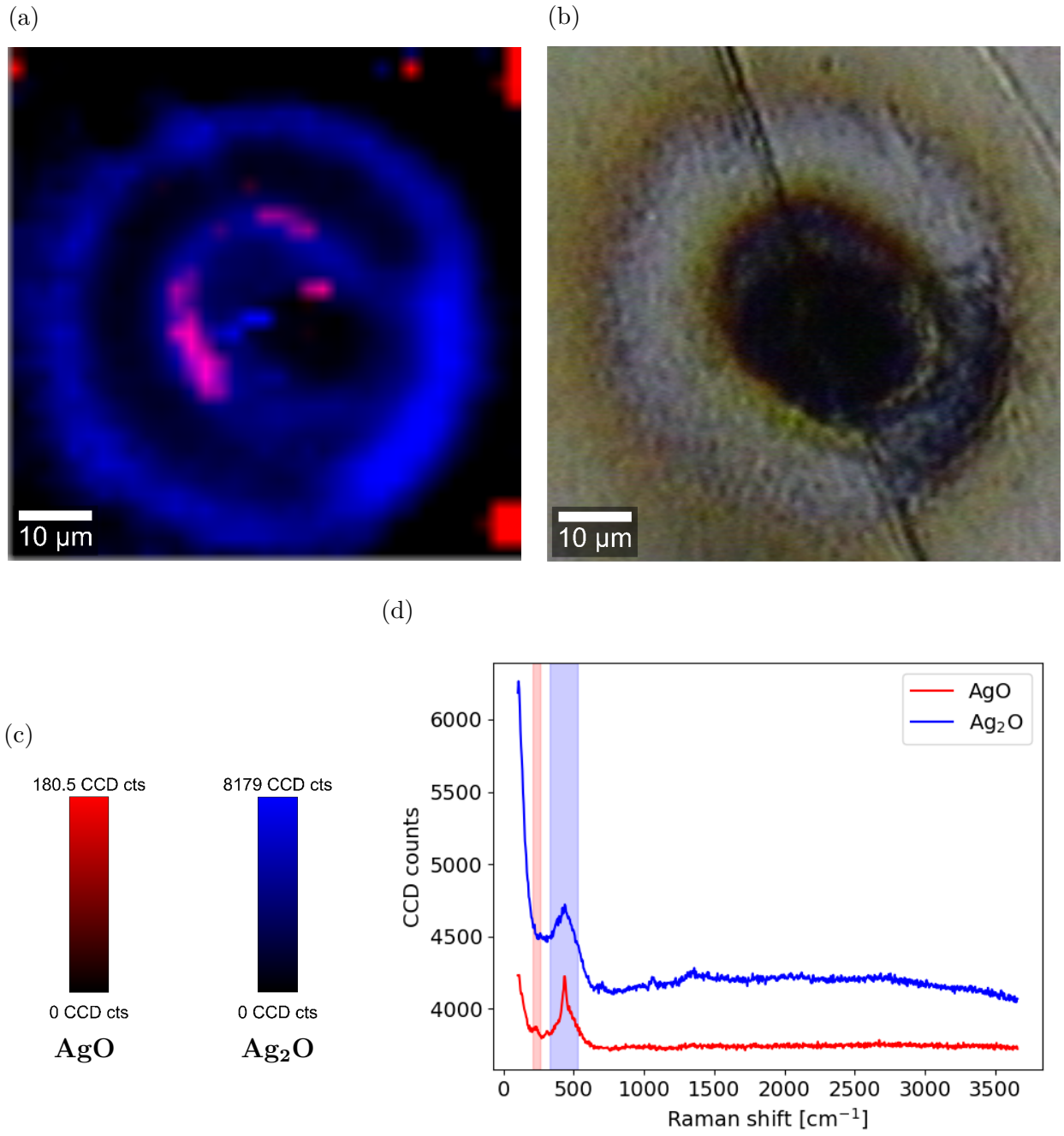

Figure 4.22: Raman scan of silver oxides, for 9.66 µJ pulse energy and 300 pulses then 400 pulses after a 4 hour wait between laser machining. (a) Raman scan, (b) corresponding brightfield image, (c) scale bars for Raman scan, (d) example of Raman spectra found in the scan, along with integrated area shaded in the color respective to the spectra.

laser, and a pulse energy of 8.4 µJ, a number of pulses on the order of 1000 are needed to start detecting AgO, while for the 1030 nm, 3000 pulses are needed for AgO. The results for the detection of Ag_2O are very similar for both wavelengths, where approximately 100 pulses are required to form Ag_2O.

It was also shown that neither the repetition rate of the laser nor the fact that a certain number of pulses was delivered in two laser machining sessions matters regarding Ag_2O and AgO formation. This shows that formation of silver oxides is not driven by heat accumulation on the sample for these repetition rates. However, it is unknown if repetition rate starts to have an effect at higher values, either due to more heat accumulation or due to the oxygen near the point of impact of the laser (where the chemical reactions take place) starting to deplete.

A mechanism for the formation of Ag_2O and AgO is proposed here. Figures 4.23 and 4.24 show sketches of the proposed mechanisms. The dissociation of oxygen molecules takes place via shockwaves from the ablated material that travel through the air. First, Ag_2O is formed by the silver vapour and droplets reacting with the dissociated oxygen and/or ozone and then redepositing on the surface. AgO is then formed when there is enough Ag_2O in the surface that can react with the dissociated O_2. Another source of oxygen atoms could be from the laser directly ionising the oxygen in the air due to the high intensity of the laser, creating atomic oxygen that could also react with the silver.

There are discrepancies with the literature in the laser fluence needed to form Ag_2O [1]. It was found prior to this work that a fluence of only 63.65 J/cm^2 was sufficient to start the formation of Ag_2O. It should be mentioned that in the experiments found in the article, rather than laser machining a dot, a bullseye pattern was machined instead, so it would be more appropriate to compare an experiment where a line is laser machined instead. A brief set of experiment where lines are laser machined instead of dots is described in appendix C.

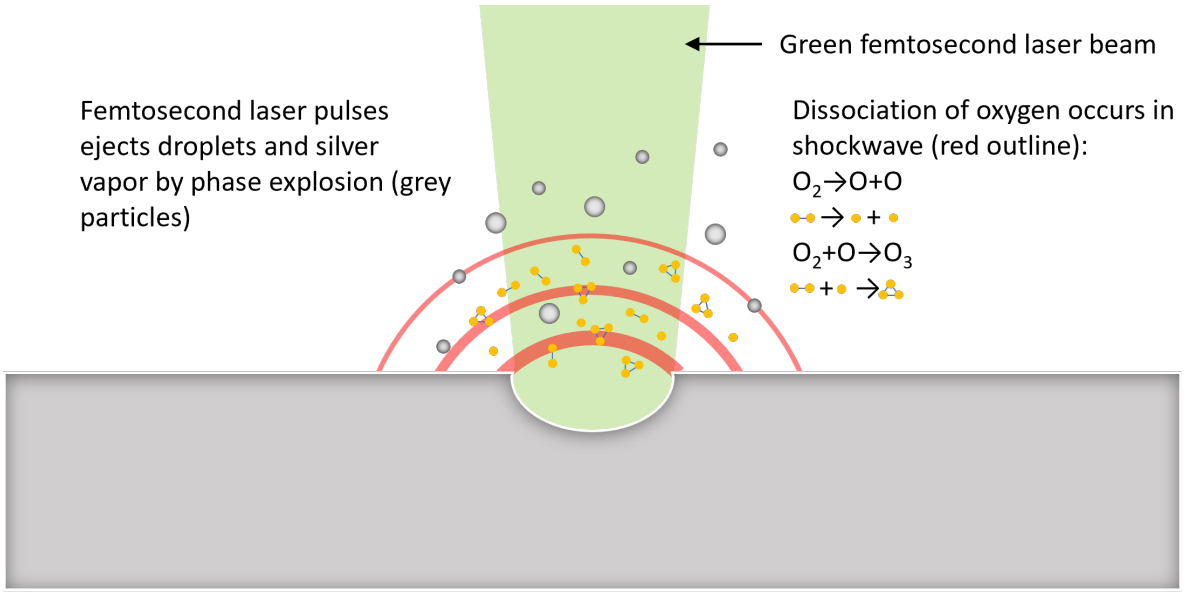

Silver reacts with atomic oxygen and/or ozone to form Ag_2O (grey and yellow particles):
$2Ag+O \rightarrow Ag_2O$
$2Ag+O_3 \rightarrow Ag_2O+O_2$

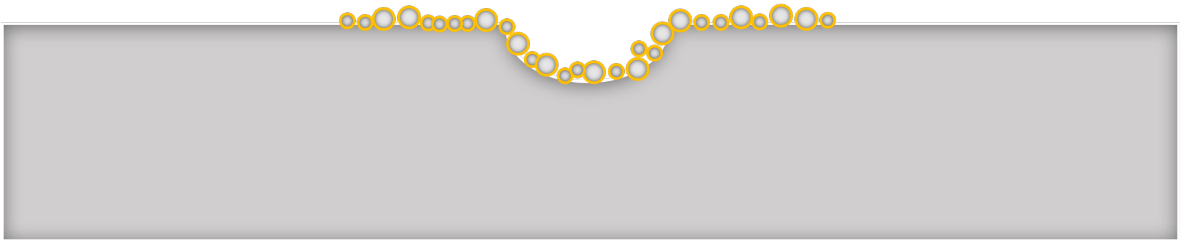

Figure 4.23: Proposed mechanism for the formation of Ag_2O. Silver is ejected from the material by phase explosion. Oxygen molecules are dissociated to form atomic oxygen from shockwaves. Ozone may be formed also. The silver vapour and droplets react with the oxygen atoms and/or the ozone and redeposit as Ag_2O on the surface.

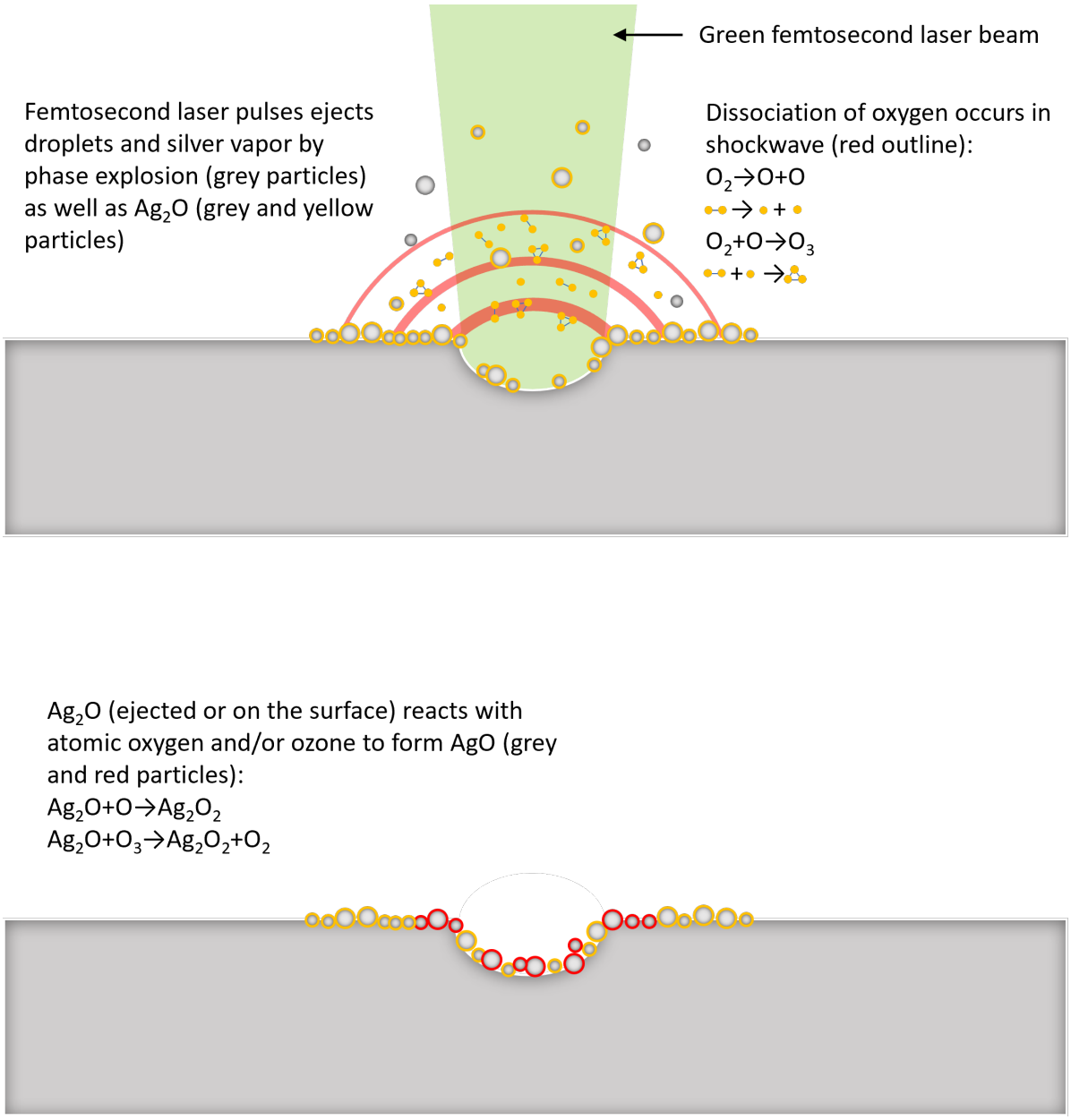

Figure 4.24: Proposed mechanism for the formation of AgO. Silver is ejected from the material by phase explosion. There may also be some Ag_2O ejected on the surface. Reactive atomic oxygen and ozone are formed by shockwaves. The atomic oxygen reacts with the Ag_2O to form AgO.

Chapter 5

Silver Oxide Decomposition After Laser Machining

In this section, the rate of decomposition of each oxide formed by laser machining as well as the products of decomposition in ambient conditions and by photodecomposition by the continuous wave laser are discussed. They are compared with the decomposition of a sample of silver oxide formed via oxygen plasma treatment of a bulk silver sample.

5.1 Decomposition in Ambient Conditions

The experiments described in section 4 were studied after leaving the samples in ambient air for time periods ranging from a day to over a month after laser machining. The samples are stored in a drawer in lab conditions, and no light reaches them. The goal is to assess the stability of the silver oxides on the surface as well as find out potential chemical reactions that may involve AgO on nanotextured silver. Raman scans from different days are made on distinct matrices to prevent the continuous wave laser from affecting the results, except for the 2-month-old sample (section 5.1.2), where one of the already-scanned matrices was scanned once again instead.

5.1.1 Short Term Changes

Figures 5.1 and 5.2 show brightfield images of same-parameter dots machined on distinct matrices at pulse energies of 10.5 µJ, 3000 pulses and 10.5 µJ, 100 pulses respectively. Both experiments were done with a laser wavelength of 515 nm and a repetition rate of 5 kHz. The scans as well as the brightfield images were taken the same day, one day after and 8 days after laser machining. Those values were chosen since it shows a situation where both oxides appear and where Ag_2O only appears. The corresponding scans are shown in figures 5.3 to 5.8.

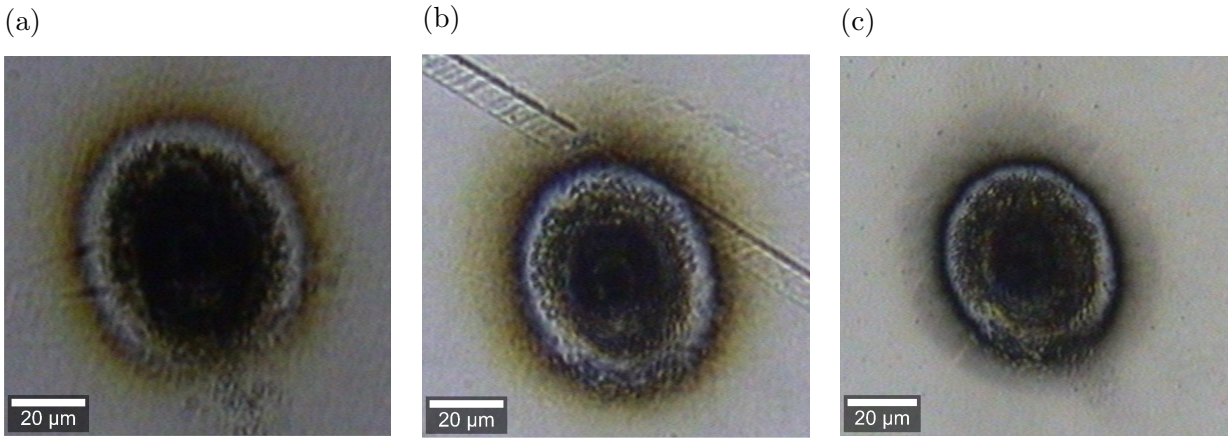

Figure 5.1: Brightfield images of laser machined dots with 10.5 µJ of pulse energy and 3000 pulses at (a) the same day as laser machining, (b) 1 day after laser machining and (c) 8 days after laser machining. The laser machined dots shown here are from different matrices.

The brightfield images show a few interesting phenomena from decomposition and contamination; while the size of the re-deposited material around the crater does not change much (which also confirms that the machining conditions such as focus do not change much), the color of the redeposited material changes. For the 3000 pulses case, it is obvious that the characteristic brow color from Ag_2O turns light grey after 8 days. It could be argued that even after 1 day the brown portion becomes less vibrant. The blue portions, however, do not change much. The 100 pulses case show similar results, but it is more obvious that the brown part loses its color after only one day. The 8-day case does not have any brown rede-

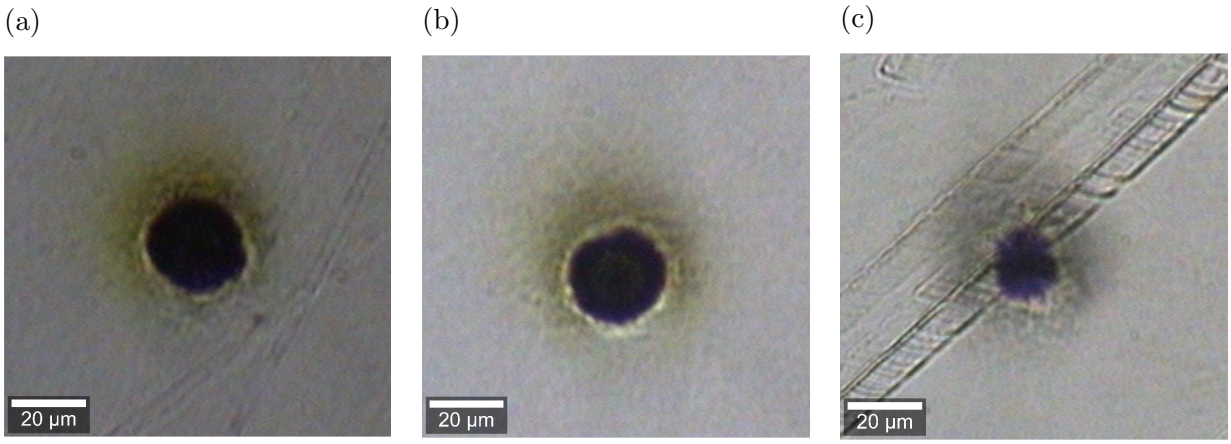

Figure 5.2: Brightfield images of laser machined dots with 10.5 µJ of pulse energy and 100 pulses at (a) the same day as laser machining, (b) 1 day after laser machining and (c) 8 days after laser machining. The laser machined dots shown here are from different matrices.

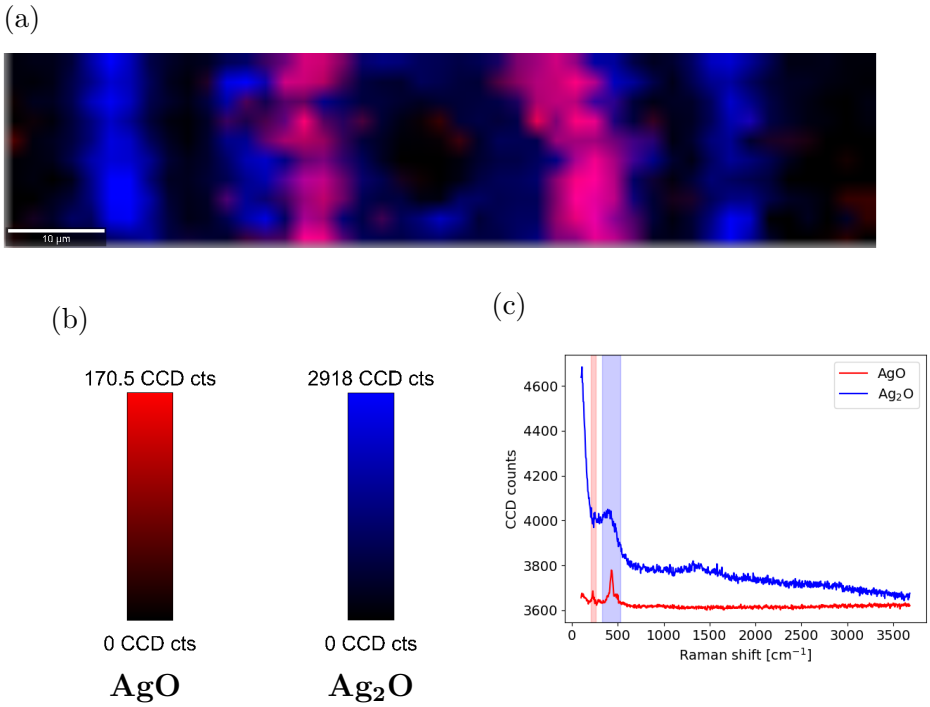

Figure 5.3: Raman scan of silver oxides, for 10.5 µJ pulse energy and 3000 pulses, machined the same day. (a) Raman scan, (b) scale bars, (c) example of Raman spectra found in the scan, along with integrated area shaded in the color respective to the spectra.

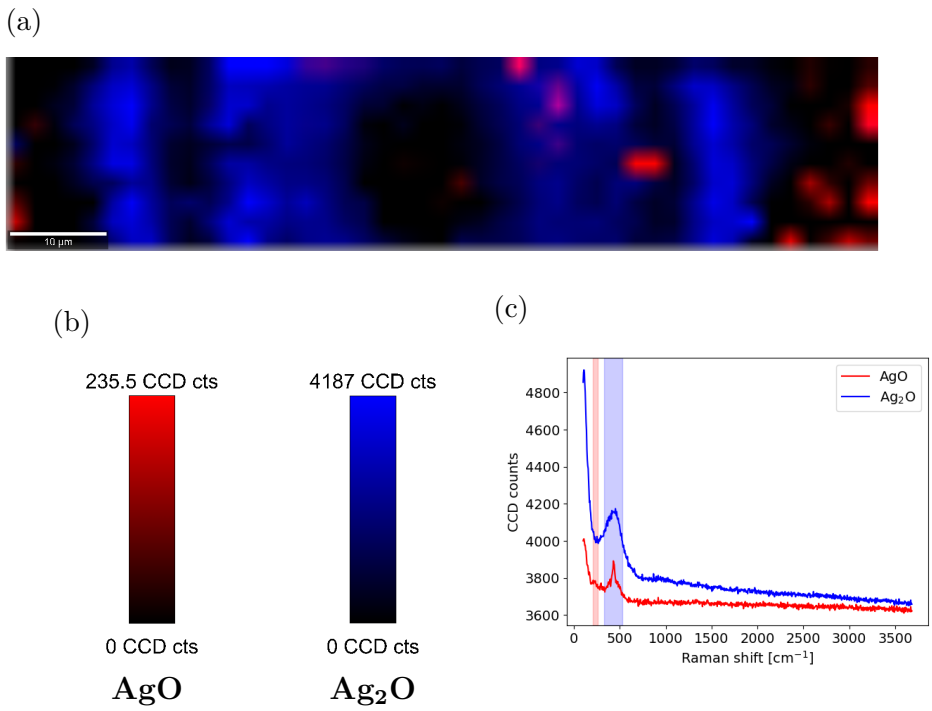

Figure 5.4: Raman scan of silver oxides, for 10.5 µJ pulse energy and 3000 pulses, machined the day before. (a) Raman scan, (b) scale bars, (c) example of Raman spectra found in the scan, along with integrated area shaded in the color respective to the spectra.

posited material. This may be due to the redeposited Ag_2O material decomposing or being contaminated. Nothing can be concluded regarding AgO from the brightfield images alone due to the difficulty in identifying AgO regions from the brightfield images, as discussed in section 4.2.2.

The Raman scans in figures (5.3 to 5.8) tell a similar story, except that AgO is also visible. In the 3000 pulses case, the amount of redeposited AgO on the surface quickly diminishes in 1 day; figure 5.3 shows a ring of AgO surrounding the crater, as would be expected, while figure 5.4 shows that there is almost no AgO remaining (only the equivalent of a few pixels remain), but the distribution of Ag_2O remains similar with some close to the crater and a second larger ring farther away, with an area of low Raman signal. This agrees with the brightfield images, in which the brown region coincides with the larger Ag_2O ring in the scans. After 8 days (figure 5.5), there is still some Ag_2O appearing in the scan, but only close to the crater where AgO used to be. There is also no AgO remaining. This also agrees

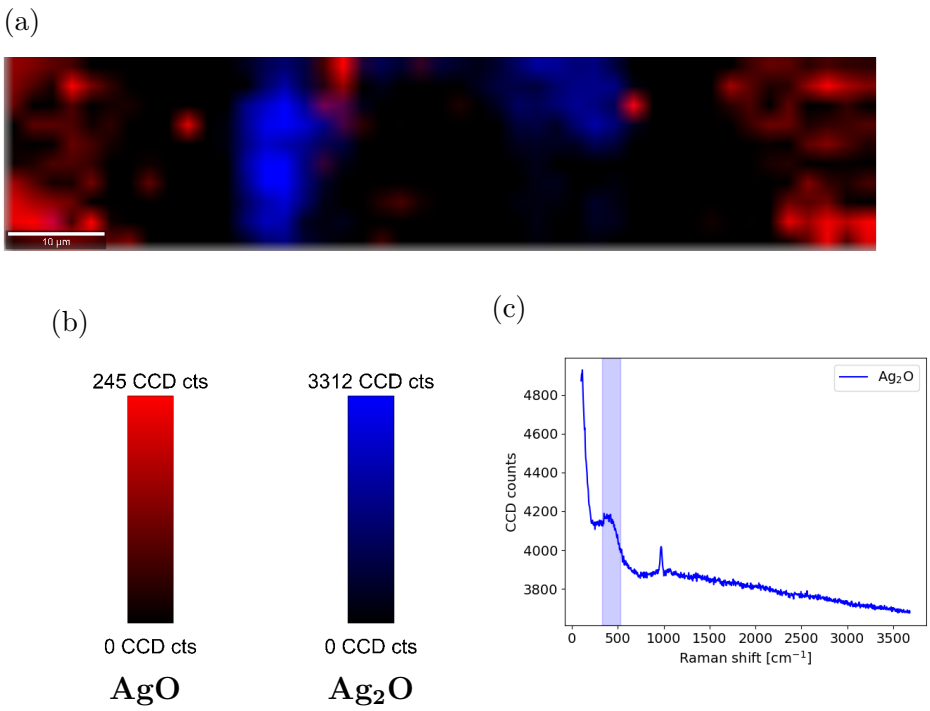

Figure 5.5: Raman scan of silver oxides, for 10.5 µJ pulse energy and 3000 pulses, machined 8 days before. (a) Raman scan, (b) scale bars, (c) example of a Raman spectrum found in the scan, along with the integrated area shaded.

with the brightfield image at the left of figure 5.1, where the brown section corresponding to the Ag_2O ring has turned light grey. This shows that the Ag_2O may have been contaminated or may also have decomposed, and the AgO may decompose into Ag_2O in a few days. For the 100 pulses case (figures 5.6 to 5.8), the Raman scans also agree with the brightfield images; the Ag_2O does not decompose or does not get contaminated in one day and the brown portion of the brightfield image does not turn grey. It is only for the 8-day scan that no Ag_2O regions remain (figure 5.8). Since there is no more silver oxide to show in figure 5.8, a spectrum of the D and G bands is shown instead. This type of spectrum shows up in a large region on the Raman scan.

The silver oxide parameter thresholds were also compared the same day of laser machining, one day after laser machining and five days after laser machining to better study their decomposition and contamination. Due to the overall similarities between the 1030 nm and 515 nm experiments discussed in section 4.3 and the larger parameter space offered by the

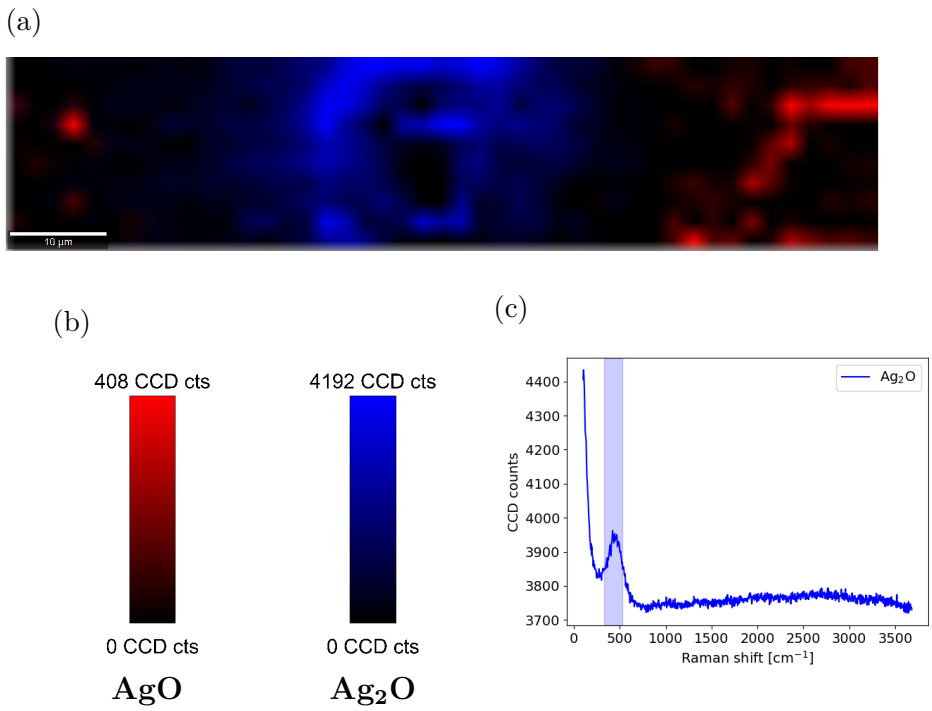

Figure 5.6: Raman scan of silver oxides, for 10.5 µJ pulse energy and 100 pulses, machined the same day. (a) Raman scan, (b) scale bars, (c) example of a Raman spectrum found in the scan, along with the integrated area shaded.

higher pulse energy, only the thresholds for the 1030 nm laser are shown. The repetition rate is 5 kHz. Figure 5.9 shows a comparison between the oxide thresholds 1 day after laser machining and 5 days after laser machining. This figure can also be compared with figure 4.11 to compare oxide thresholds from the same day as laser machining and 1 day after. It should be mentioned that the dot matrix machined the same day as the Raman scans were done is not the same as the matrix that was studied 1 or 5 days after laser machining. The Raman spectra were briefly looked at to determine oxide presence, without performing Raman mapping.

Comparing figures 4.11 and 5.9, Ag_2O created with low fluence do not get detected after a few days, and only the AgO created with highest pulse energy and number of pulses remains. This shows that both oxides gradually decompose at a certain rate and that there should eventually be no more oxide detected no matter the laser parameter used.

Figures 5.10 and 5.11 show Raman scans for a silver pellet that underwent oxygen plasma

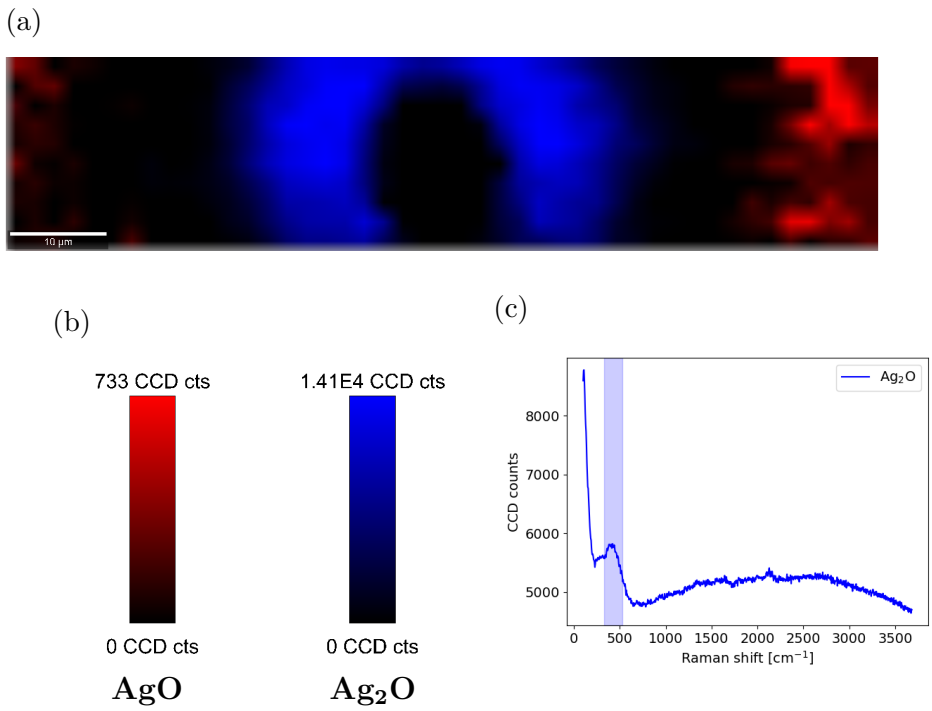

Figure 5.7: Raman scan of silver oxides, for 10.5 µJ pulse energy and 100 pulses, machined the day before. (a) Raman scan, (b) scale bars, (c) example of a Raman spectrum found in the scan, along with the integrated area shaded.

treatment to create an oxide layer. The Raman spectra and decomposition of this silver oxide sample are compared with the data gathered from laser machined dots to compare oxide contents as well as decomposition products. Raman spectroscopy detects the characteristic peaks from both silver oxides in this sample. The peaks are in fact similar to the ones reported in this thesis from laser machining.

The Ag_2O broad peak from the same-day scan is a bit sharper than what is shown from scans from laser machining. This may be explained by the fact that where there is Ag_2O detected, there may be trace amounts of AgO also detected, such that the 235 cm^{-1} peak is not highlighted on the scan, but the 435 cm^{-1} from AgO still constitutes a significant portion of the integrated area for Ag_2O highlighting. However, the peak is too broad to be purely from the Raman response of AgO, meaning it must represent a mix of Ag_2O and AgO.

Comparing scans from the same day as the treatment and 9 days after, there are no

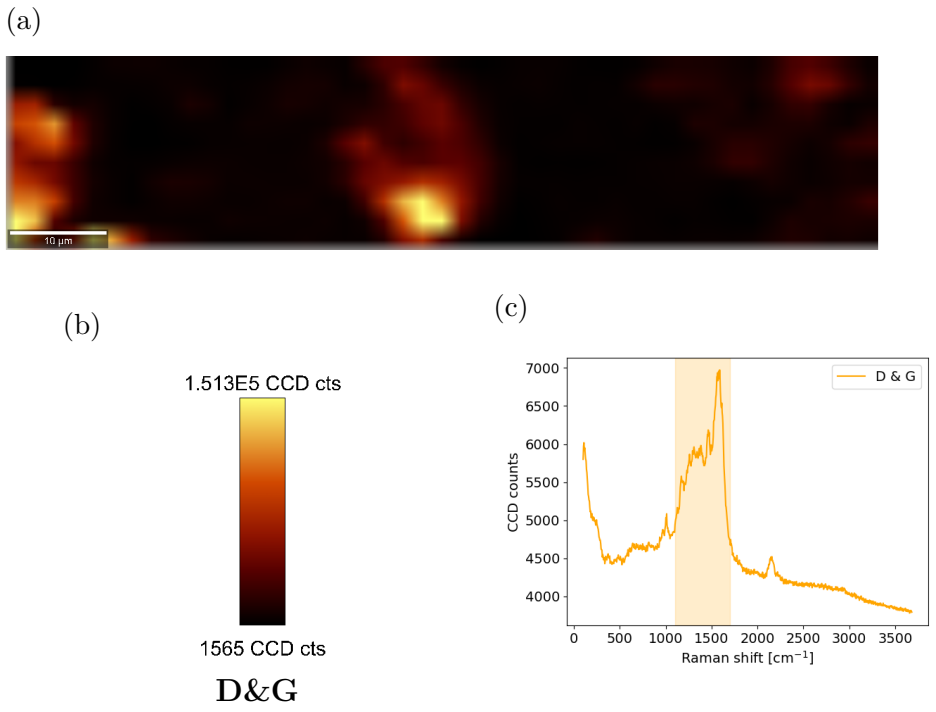

Figure 5.8: Raman scan of silver oxides, for 10.5 µJ pulse energy and 100 pulses, machined 8 days before. (a) Raman scan, (b) scale bar, (c) example of a Raman spectrum found in the scan, along with the integrated area shaded.

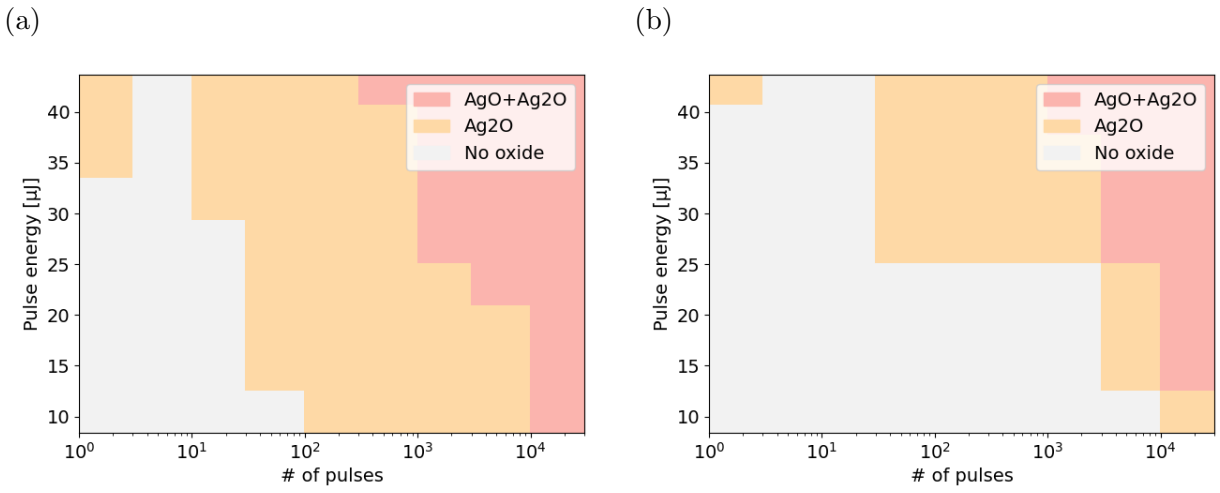

Figure 5.9: Silver oxides distribution for laser parameters tested (a) one day after laser machining and (b) five days after laser machining. As time passes, both oxides decomposes or get contaminated, meaning only higher total fluences, which make more oxide, will still have redeposited silver oxides remaining.

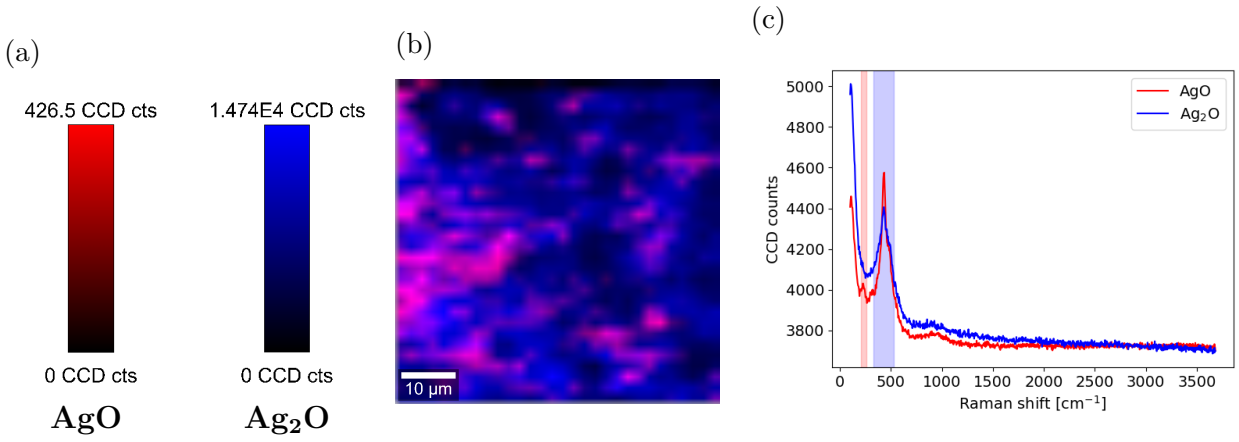

Figure 5.10: Raman scan of silver oxides from reaction with the O_2 plasma the same day as the treatment. (a) Raman scan, (b) scale bars, (c) example of Raman spectra found in the scan, along with integrated area shaded in the color respective to the spectra.

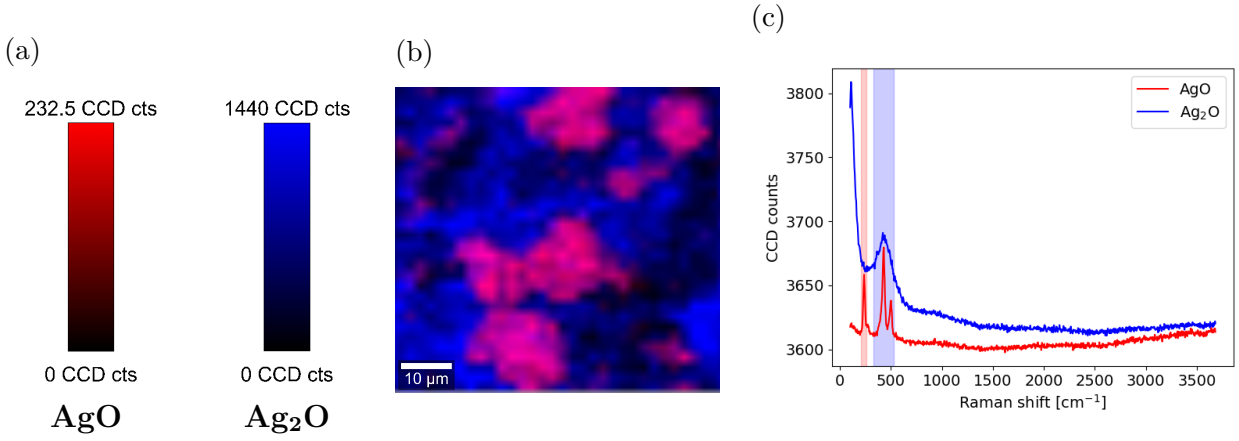

Figure 5.11: Raman scan of silver oxides from reaction with the O_2 plasma 9 days after the treatment. (a) Raman scan, (b) scale bars, (c) example of Raman spectra found in the scan, along with integrated area shaded in the color respective to the spectra.

significant changes in the amount and types of oxides detected by Raman spectroscopy, unlike the oxides created by laser machining. This could simply be due to the amount of oxide created from the start, and a longer time period might be needed before any significant changes can be detected. The distribution of oxides however has changed; while the AgO is a bit more uniformly distributed for the same day scan, the Raman scan taken 9 days after treatment show clear patches of AgO. This could be due to the flaking of surface AgO from plasma treatment: the silver oxides expanding in volume the further they are oxidised may induce stresses at the surface, and the AgO layer cracks and flakes off. External forces applied on the sample (either from walking around, going up and down the stairs, grabbing the sample with tweezers) could be removing AgO flakes that are weakly attached to the surface. It is worth mentioning that tiny dark grey particles started falling off the silver oxide sample into the petri dish holding it. These particles are most likely the silver oxide flakes mentioned. The removal of these AgO flakes may expose Ag_2O below the surface, which would explain the main Ag_2O Raman peak closely resembling the Ag_2O peak reported in this thesis and in literature. The AgO regions also show a significant peak near 500 cm^{-1}. While it is one of the characteristic peaks from AgO, prior AgO Raman spectra reported in this thesis did not have the aforementioned peak at such intensity. It often appears as a shoulder next to the 435 cm^{-1} peak, but it had never appeared at such intensity in past experiments. This could be due to a different crystal orientation.

5.1.2 Long Term Changes

To discuss long term changes on laser machined silver samples, Raman spectroscopy was performed on a few samples that were 56 days old. Figure 5.12 shows a brightfield image as well as a Raman scan, with the D and G band regions highlighted, which indicate the presence of carbon species on the sample surface, potentially from contamination. This laser machined dot is the same as the one presented on the left side of figure 5.1; it was made by using 3000 pulses with a pulse energy of 10.5 µJ at a repetition rate of 5 kHz.

(a)

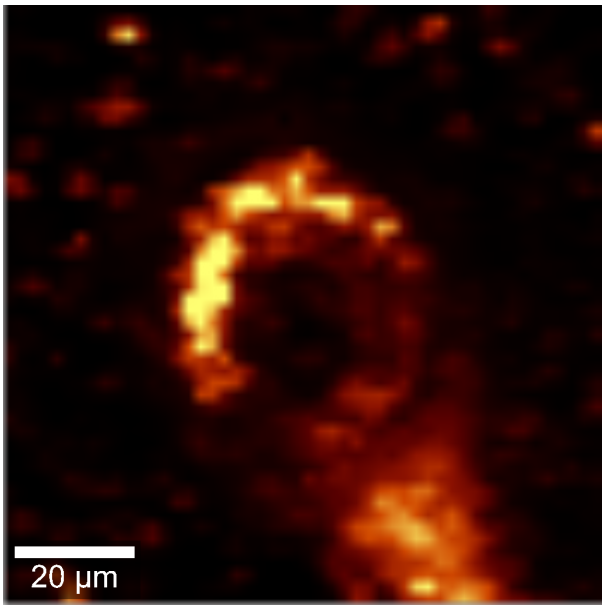

(b)

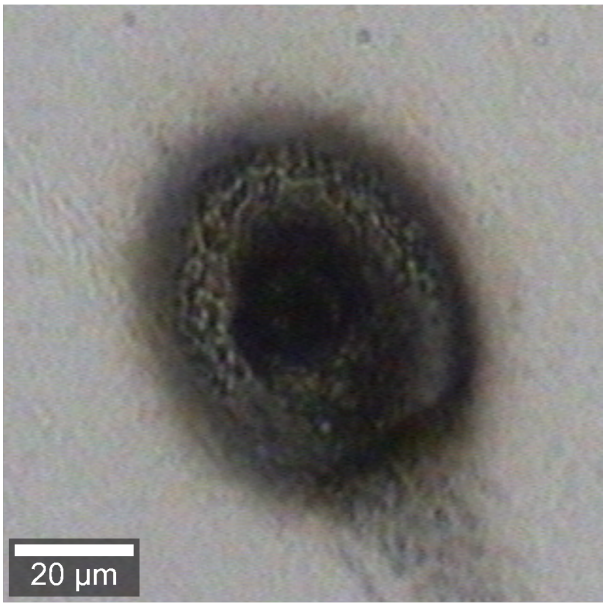

(c)

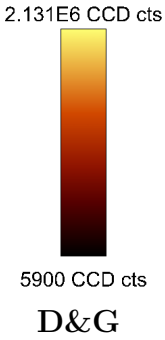

(d)

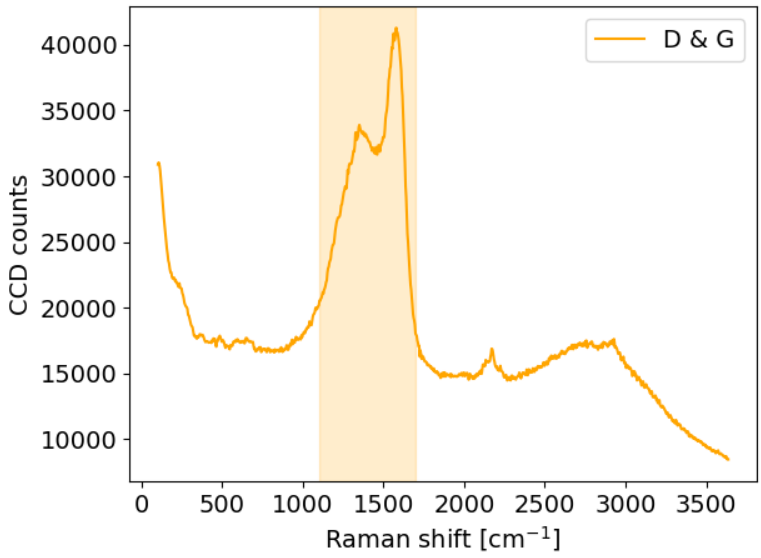

Figure 5.12: Raman scan of machined sample 54 days after laser machining. (a) Raman scan, (b) corresponding brightfield image, (c) scale bars, (d) example of a Raman spectrum found in the scan, along with the integrated area shaded. The sample shown here is the same as the one shown on the left image of figure 5.1.

The brightfield image clearly shows a difference in the colors of the redeposited material, as well as the color of the crater itself. The sample is mostly dark grey, including the parts that were blue when imaged 8 days after laser machining. Looking at the Raman spectra, the only significant peaks that are seen are the D and G band, indicating that the sample has been contaminated by carbon. As expected from the previous section (5.1.1), no more silver oxide remains on the surface.

5.1.3 Silver Carbonate Ag_2CO_3 Formation from Ag_2O

One of the potential chemical species detected by Raman spectroscopy scans of the laser machined dots is silver carbonate (Ag_2CO_3). Figure 5.13 shows a laser machined dot in which Ag_2CO_3 has formed very close to the crater. It is difficult to associate a color on the brightfield image with the presence of Ag_2CO_3 due to the proximity to the crater. It is also interesting that it has only formed close to the crater, and not farther away. Figure 4.13 also shows that small but well-defined Ag_2CO_3 peaks have formed in the Ag_2O spectrum. Ag_2CO_3 is formed via a chemical reaction between Ag_2O and CO_2 in ambient air (reaction 2.12). Since AgO decomposes into Ag_2O, this means that AgO may also contribute to the formation of Ag_2CO_3. The D and G bands also appear alongside the silver carbonate peaks, confirming the presence of carbon. The Raman scan was taken around 4 hours after laser machining, giving the sample some time to react with ambient carbon dioxide. Ag_2O reacts quickly with ambient carbon dioxide.

5.2 Decomposition from Raman Spectroscopy

The continuous wave laser illuminating the sample during Raman spectroscopy may damage the redeposited materials if the power is set too high. In this section, the effects of the continuous laser on laser machined samples is discussed for newly machined samples as well as aged silver oxide samples.

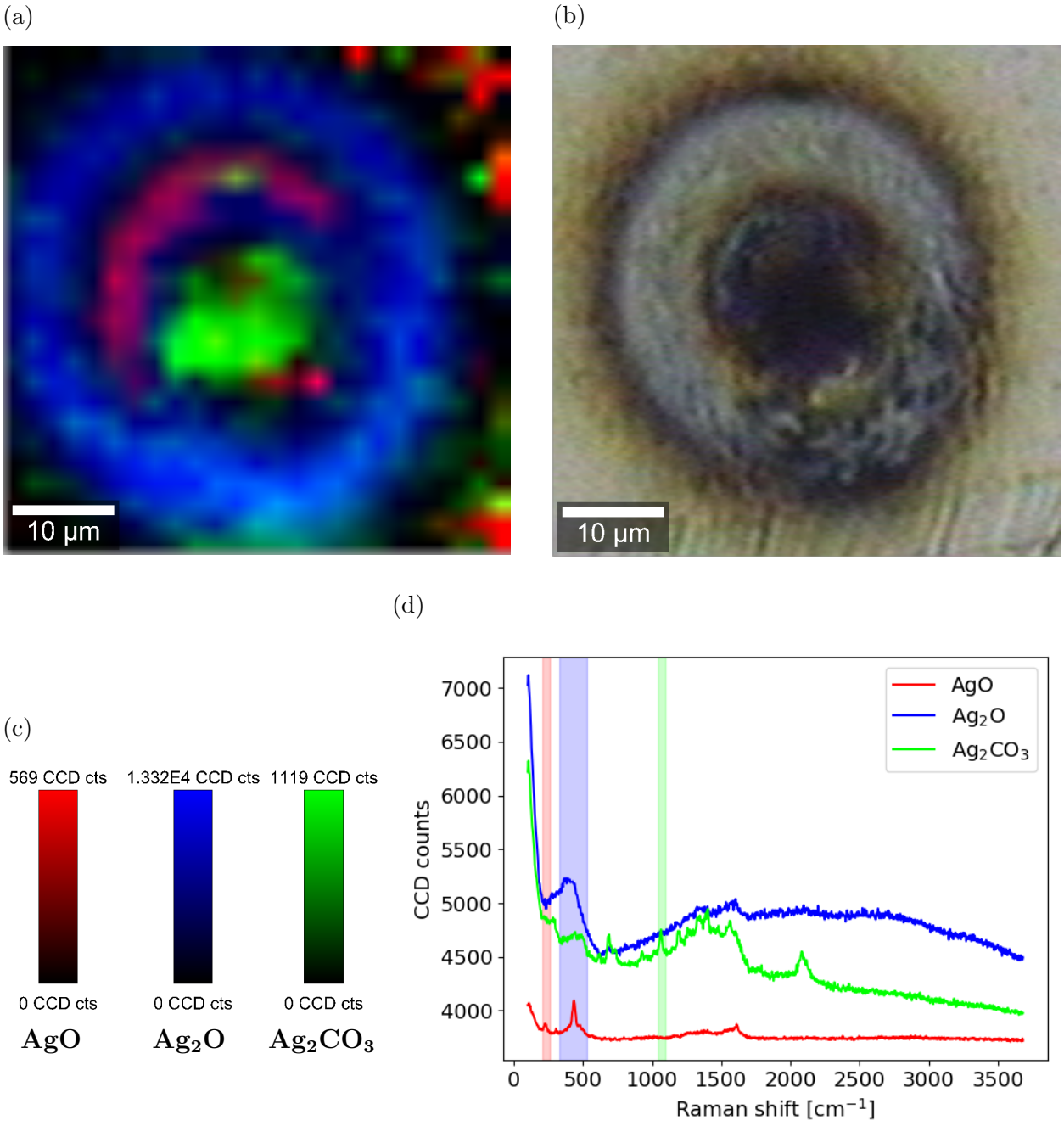

Figure 5.13: Example of a laser machined dot in which silver carbonate has formed. (a) Raman scan, (b) corresponding brightfield image, (c) scale bars, (d) example of Raman spectra found in the scan, along with integrated area shaded in the color respective to the spectra. The laser machining parameters used to make this dot were as follows: the repetition rate was set at 500 Hz, the pulse energy was 7.14 µJ, 1000 pulses were fired, and the laser wavelength was 515 nm.

5.2.1 Silver Oxides Decomposition from Continuous Wave Laser

To show the effects of the continuous wave laser on the sample, two Raman scans of a single machined dot were taken back-to-back. The results are shown in figure 5.14 and 5.15. It should be expected that both scans give exactly the same oxide distributions. It is shown that they are very similar, but one can notice differences by looking carefully. The brightfield images are also a bit different.

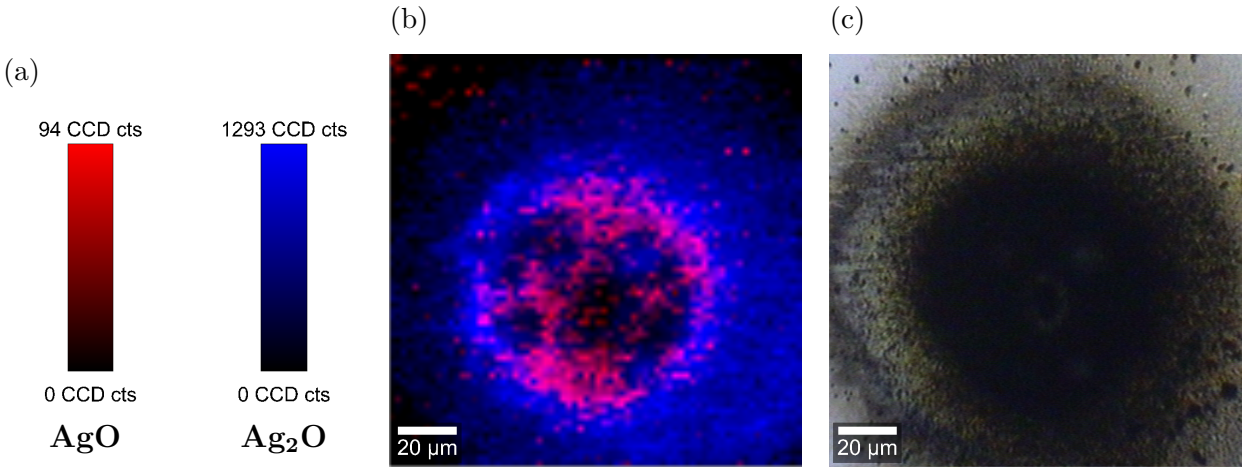

Figure 5.14: Oxide distribution for first Raman scan. This is from machining 10000 pulses twice (20000 pulses in total) at 8.4 µJ pulse energy. (a) Raman scan, (b) scale bars, (c) brightfield image corresponding to the scan.

The most obvious change is the amount of AgO highlighted on both scans; the one shown in figure 5.15 has less AgO based on the size of the highlighted area alone. Here the CCD counts are also useful since there should be no difference in laser power or surface morphology between both scans, meaning they should be the same. A decrease in CCD counts mean that there is less AgO signal so less AgO. Interestingly, the counts for Ag_2O have increased slightly. This may be attributed to the AgO decomposing into Ag_2O. The brightfield images show a difference in the color of the redeposited material, the second one being slightly darker.

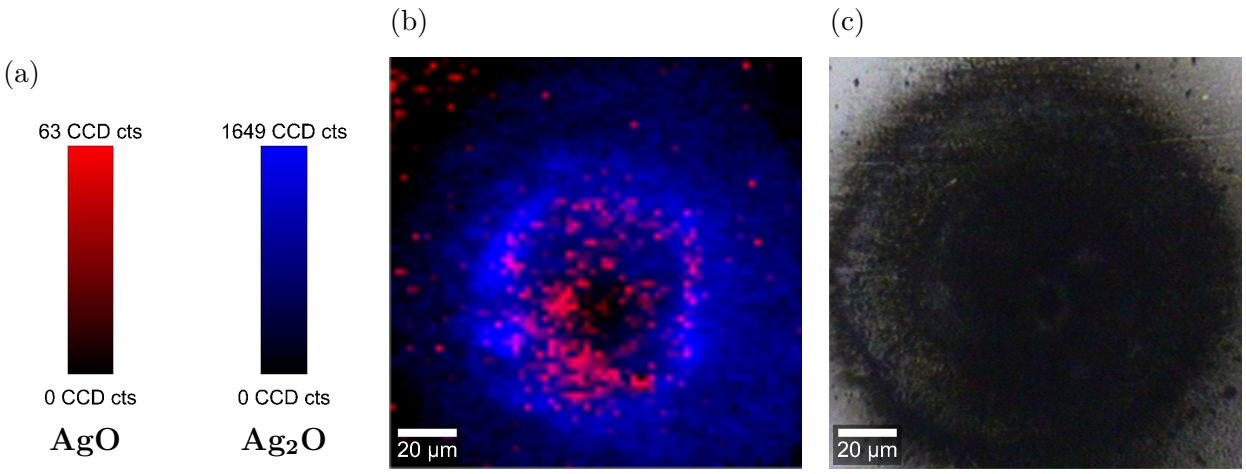

Figure 5.15: Oxide distribution for second Raman scan taken directly after the first one (figure 5.14). (a) Raman scan, (b) scale bars, (c) brightfield image corresponding to the scan.

5.2.2 971 cm^{-1} Raman Peak on Aged Laser Machined Silver Oxide Samples Via Irradiation from Continuous Wave Laser

Figure 5.16 shows a Raman scan taken 3 days after laser machining. There are many regions where a very sharp peak appears at 971 cm^{-1}. This peak only appears in very specific circumstances. First there must be Ag_2O for it to appear, then the sample must be left in ambient air for a few days. This 971 cm^{-1} peak will then appear, but only after illumination from the continuous wave laser for a few seconds.

This peak appears gradually when illuminating an Ag_2O region after leaving a sample in ambient air for a few days; it never appears by simply leaving the sample in ambient air, nor does it appear by illuminating an Ag_2O region directly after laser machining. The sample must both age a few days and be illuminated by a laser to show a peak at 971 cm^{-1}. At the same time as this peak grows, the broad Ag_2O peak diminishes, until it is barely visible. Figure 5.5 also shows such a peak in the Ag_2O spectrum. The sample has aged enough so that the 971 cm^{-1} peak appears after illumination but has not aged enough for all the Ag_2O to be decomposed or contaminated. Figure 5.12 shows more proof that Ag_2O needs to be present for this to happen, and that this is not just an effect of the surface being machined

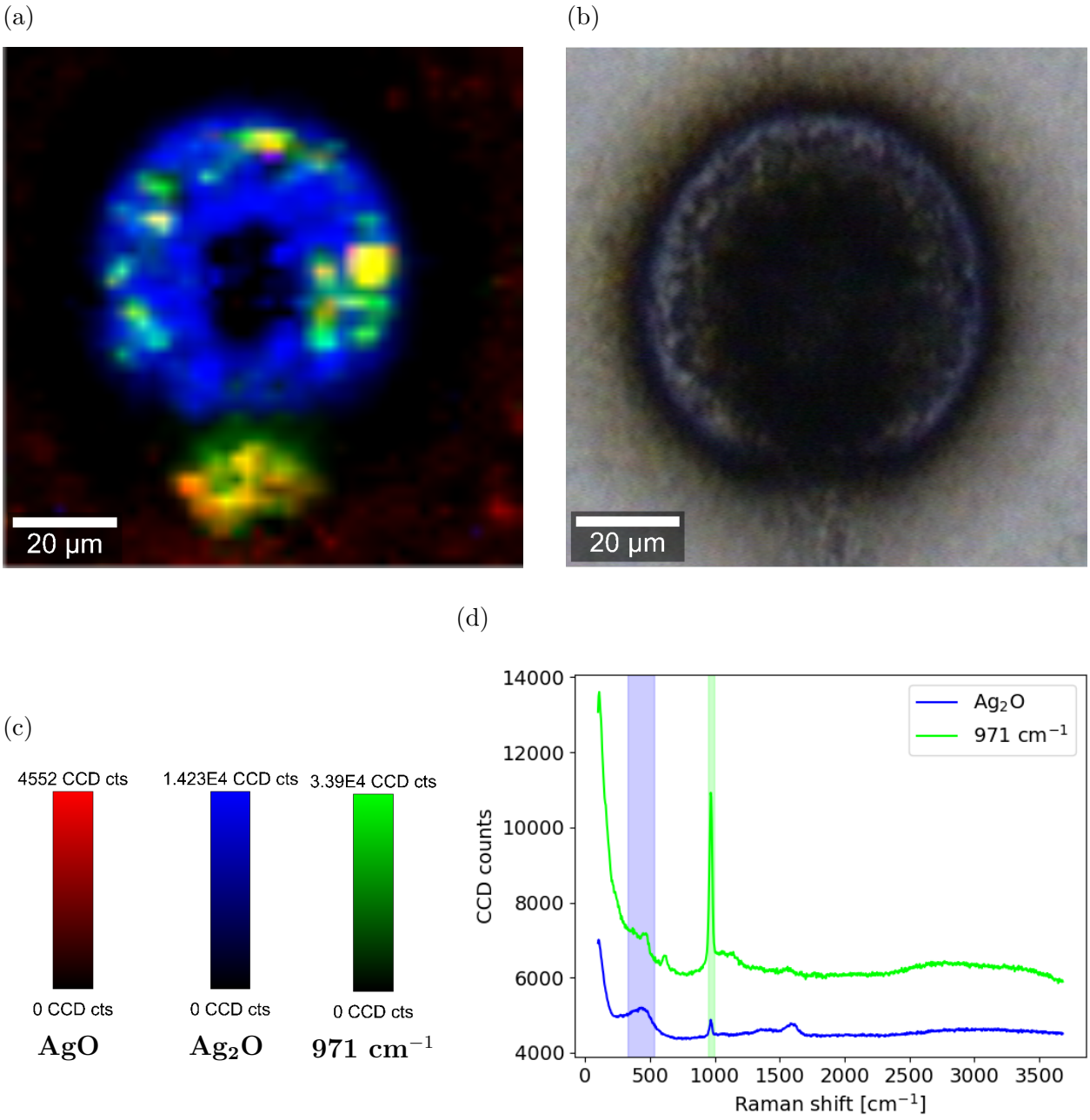

Figure 5.16: Example of a Raman scan where the 971 cm^{-1} appeared because of the continuous wave laser. (a) Raman scan, (b) corresponding brightfield image, (c) scale bars, (d) example of Raman spectra found in the scan, along with integrated area shaded in the color respective to the spectra. The laser machining parameters used to make this dot were as follows: the repetition rate was set at 5000 Hz, the pulse energy was 8.4 µJ, 10000 pulses were fired, and the laser wavelength was 515 nm. This scan was taken 3 days after laser machining.

(from nanotexturing, for example). The Raman spectrum shown is quite representative of what is seen at the location of the redeposited material, and no 971 cm^{-1} shows up. The 971 cm^{-1} peak does not show up after illuminating the silver oxide sample from O_2 plasma treatment even after it is left for 9 days in ambient air (figure 5.11). It is not clear what causes the 971 cm^{-1} peak to appear, although it may be from silver sulfite or silver sulfate based on the literature [73].

5.3 Summary and Discussion

The decomposition of silver oxide formed from femtosecond laser machining was studied. It was found that AgO decomposes in ambient conditions into Ag_2O in only one day, underlining the importance of taking the measurements the same day as laser machining. This decomposition in ambient conditions has been reported in literature [3, 13, 15]. Raman signals from Ag_2O vanished in 8 days. Brightfield images also show a slight discoloration of the surface after 8 days. After 54 days, the laser machined crater and the redeposited material were contaminated by carbon species.

Silver carbonate was detected near the laser-machined crater less than a day after laser machining. The silver carbonate quickly formed from Ag_2O and CO_2 from ambient air. There has been a report in literature of a rapid reaction of nanotextured silver oxide with atmospheric CO_2 to form Ag_2CO_3 [1]. Both experiments, which were done by femtosecond laser machining, agree with each other.

It was shown that the continuous wave laser used for Raman spectroscopy may have a substantial effect on the surface chemistry. Taking back-to-back Raman scans of a laser machined dot has shown a slight decrease of the AgO detected and brightfield images show some change in the color of the redeposited material.

There is often a peak appearing at 971 cm^{-1}. This peak exclusively appears when the sample has aged a few days and a continuous laser irradiates the redeposited material (where

there is Ag_2O). It appears as the Ag_2O decomposes from the continuous laser. Ravi Chandra Raju & Jagadeesh Kumar report a similar effect when illuminating Ag_2O deposited by PLD [37]. However, in this work, no other peak appears alongside this one. Martina *et al.* assign this peak to sulfite or sulfate (S-O symmetric stretching) [73]. There has been reports of silver sulfite and silver sulfate being formed as corrosion products in the literature. Sanders *et al.* have proposed a mechanism of formation of silver sulfite/sulfate in ambient air in which Ag_2O plays a role [81]. While sulfur is only present in the atmosphere at low concentration, it is well-known that it is the reason silver tarnishes in ambient air via formation of silver sulfide (Ag_2S) [82, 83]. The amount of sulfur in the atmosphere is significant enough to cause noticeable changes in the chemistry of silver. The absence of the 971 cm^{-1} peak before irradiation by the continuous wave laser may be because the amount of silver sulfite/sulfate molecules is low. The growth over time by irradiating the sample could be potentially due to the Ag_2O decomposing into silver nanoparticles, which induces a SERS effect amplifying the signal from silver sulfite/sulfate. The formation of silver nanoparticles from the decomposition of Ag_2O would explain the decrease in the Ag_2O peak. SERS effects from the photodecomposition of silver oxides have been reported in the literature [37].

Chapter 6

Conclusion

In this work, silver (I) oxide and silver (I, III) oxide were successfully fabricated with an ultrafast laser. Thresholds for the number of pulses and pulse energy to obtain AgO and Ag_2O were found. It was also demonstrated that neither the laser wavelength (in the visible-near-infrared range) nor the laser repetition rate (below 30kHz) significantly affect the oxide formation threshold. The non-dependency of repetition rate over the fabricated oxides suggest that the oxide formation is not affected by heat accumulation effects. It also appears that the formation of AgO by femtosecond laser machining happens in two steps, the formation of Ag_2O being an intermediate step. It was also found that the oxides formed by this method are not very stable, the AgO decomposing into Ag_2O in a few days, and the Ag_2O regions also seemingly losing Raman signal over time. The decomposition takes place both in ambient conditions and when illuminating the sample with a laser.

Future experiments for femtosecond laser-based silver oxide formation could include the laser machining of a pure silver oxide pellet to study and further confirm the formation of AgO from Ag_2O. The stability of the AgO formed this way could also be assessed. Furthermore, more measurements regarding the surface morphology of the oxides, including its change over time, could be made. The effect of oxygen concentration could also be assessed by laser machining silver in a high-oxygen concentration environment.

The instability of the oxides created by this method make it difficult to find applications, however the high precision of femtosecond laser machining along with the formation of silver oxides could present interesting applications in electrodes if there exists a way to attenuate this problem. An advantage of this method of silver oxide formation is the micron-scale resolution at which silver oxides can be fabricated. There could be applications regarding gas sensors or for forming silver nanoparticles in a highly controlled way by decomposing the redeposited silver oxide that is created from laser machining back into metallic silver. The colours obtained when machining silver may also be used for applications regarding display.

Appendices

A Carbon Contamination on Unmachined Silver

Figure A.1 shows a Raman scan of a clean silver surface is presented to show that the main contamination source is from carbon. The visibly clean surface does not show any Raman signal, and regions with black specs show obvious D and G bands.

B Unusual Raman Scans

Laser machined dots that do not follow the trend of figure 4.8b are shown in figures B.1 and B.2. While the brightfield image does not show anything unusual, the Raman scans show that the Ag_2O locations coincide well with the AgO location, which does not usually happen. There is also no outer Ag_2O ring in both of these cases. The regions with only Ag_2O are also very sparse and are not farther away from the center of the crater than AgO unlike every other scan reported in this thesis. It is important to keep in mind that the AgO peak at approximately 430 cm^{-1} also contributes to highlighting Ag_2O, so any overlap between red and blue regions may only show the presence of AgO.

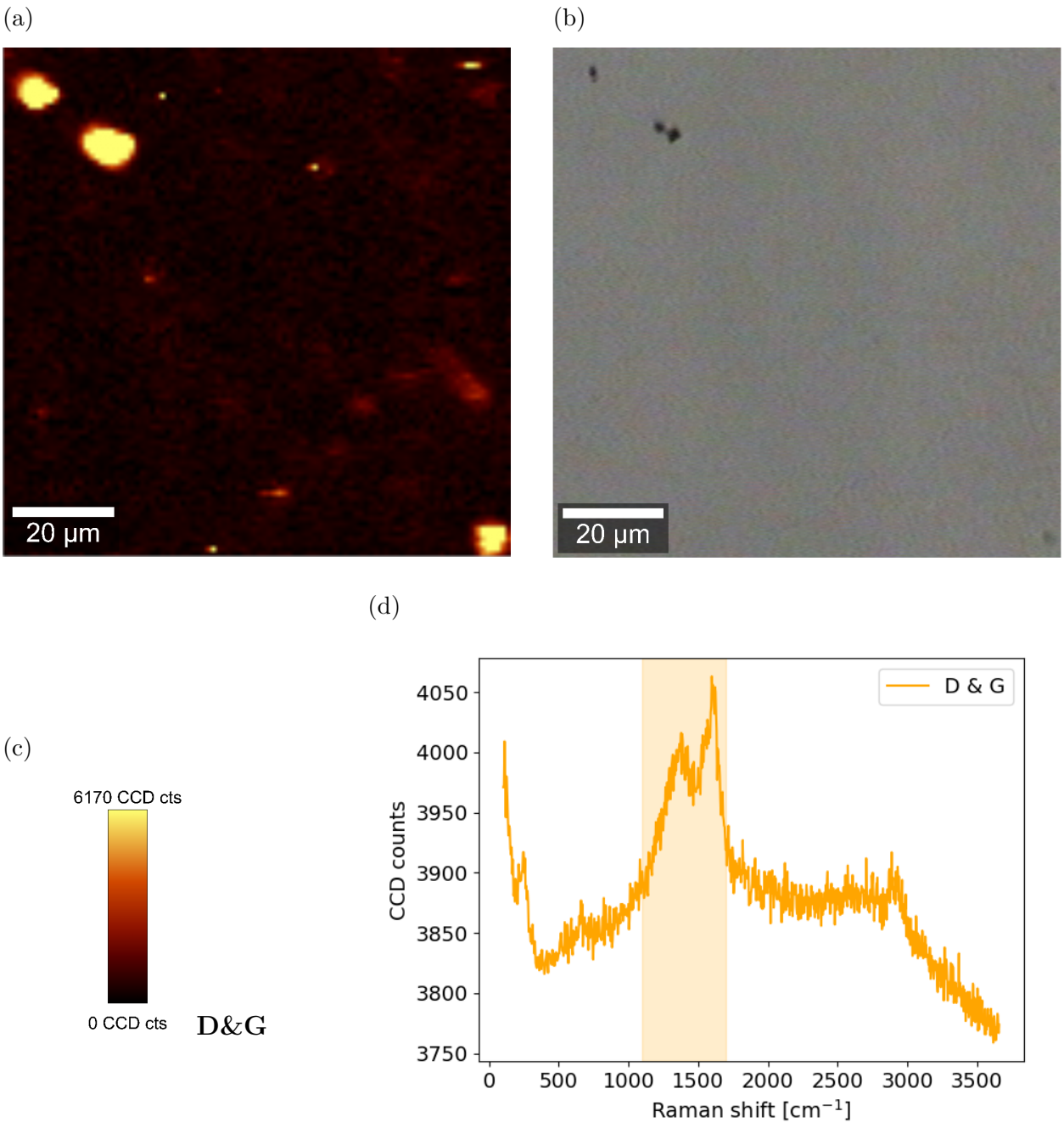

Figure A.1: Raman scan of a (mostly) clean silver surface. (a) Raman scan, (b) corresponding brightfield image, (c) scale bars, (d) example of a Raman spectrum found in the scan, along with integrated area shaded. Black specs coincide with regions with high Raman signals in the D and G bands.

(a)

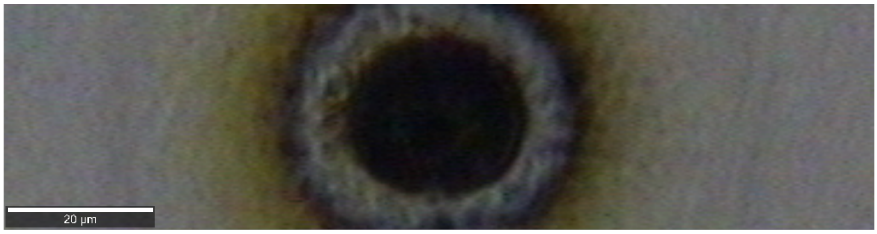

(b)

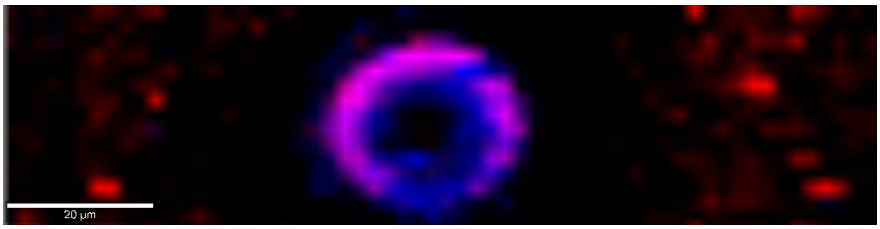

(c)

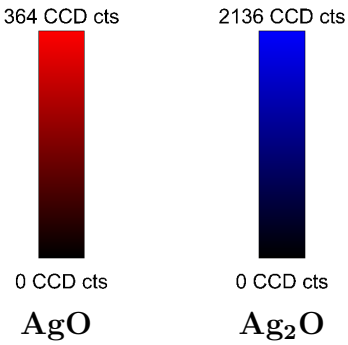

(d)

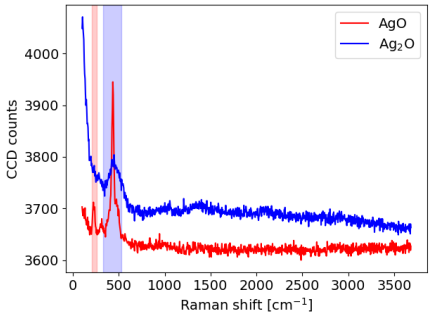

Figure B.1: Raman scan of silver oxides, for 3.15 µJ pulse energy and 10000 pulses. (a) Brightfield image, (b) Raman scan, (c) scale bars, (d) example of Raman spectra found in the scan, along with integrated area shaded in the color respective to the spectra.

(a)

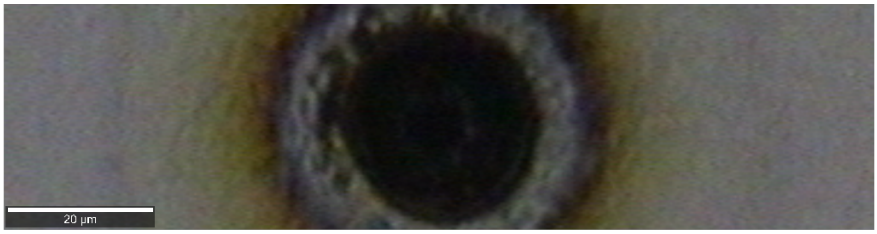

(b)

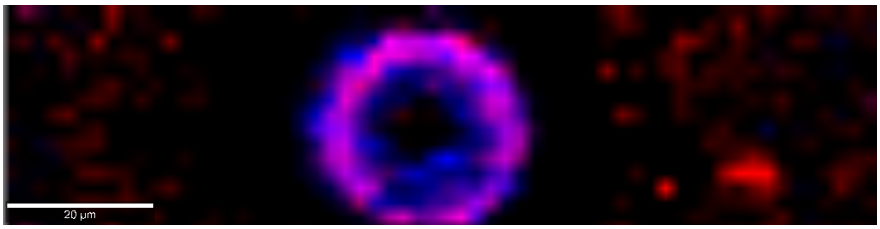

(c)

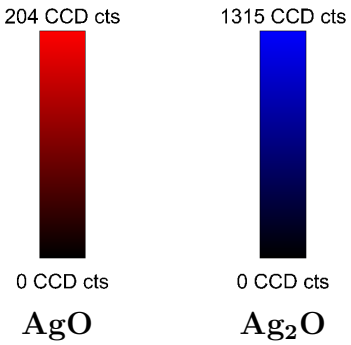

(d)

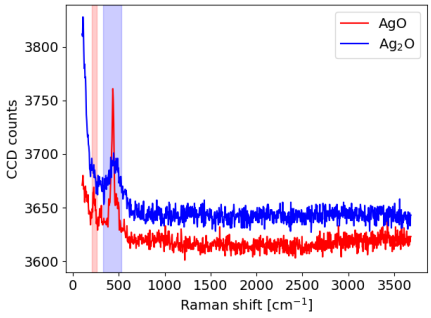

Figure B.2: Raman scan of silver oxides, for 4.2 µJ pulse energy and 10000 pulses. (a) Brightfield image, (b) Raman scan, (c) scale bars, (d) example of Raman spectra found in the scan, along with integrated area shaded in the color respective to the spectra.

C Differences Between Laser Machined Lines and Laser Machined Dots

A brief set of experiments where lines were machined by continuously pulsing the laser and moving the stage in one direction was conducted. Figure C.1 shows a Raman scan of one of these experiments, along with a brightfield image and an example spectrum. In this set of experiments, a laser fluence lower than what is required to get AgO was used, yet AgO was still detected. Ag_2O was also detected in a large quantity compared to comparable laser fluences for machined dots.

The laser machined line presented in figure C.1 is made by setting the pulse energy at 9.83 µJ, and moving the stage at a speed of 0.25 mm/s. This gives a laser fluence of 25 kJ/cm^2, which is much lower than the laser fluence that was needed to start detecting AgO in the machined dot case, according to figure 4.7. There is still some AgO that is detected close to the groove, at a distance that coincides with comparable dot sizes. There is also some Ag_2O detected in the groove itself, which is rarely the case when laser machining dots. This could be because of the shallower line depth.

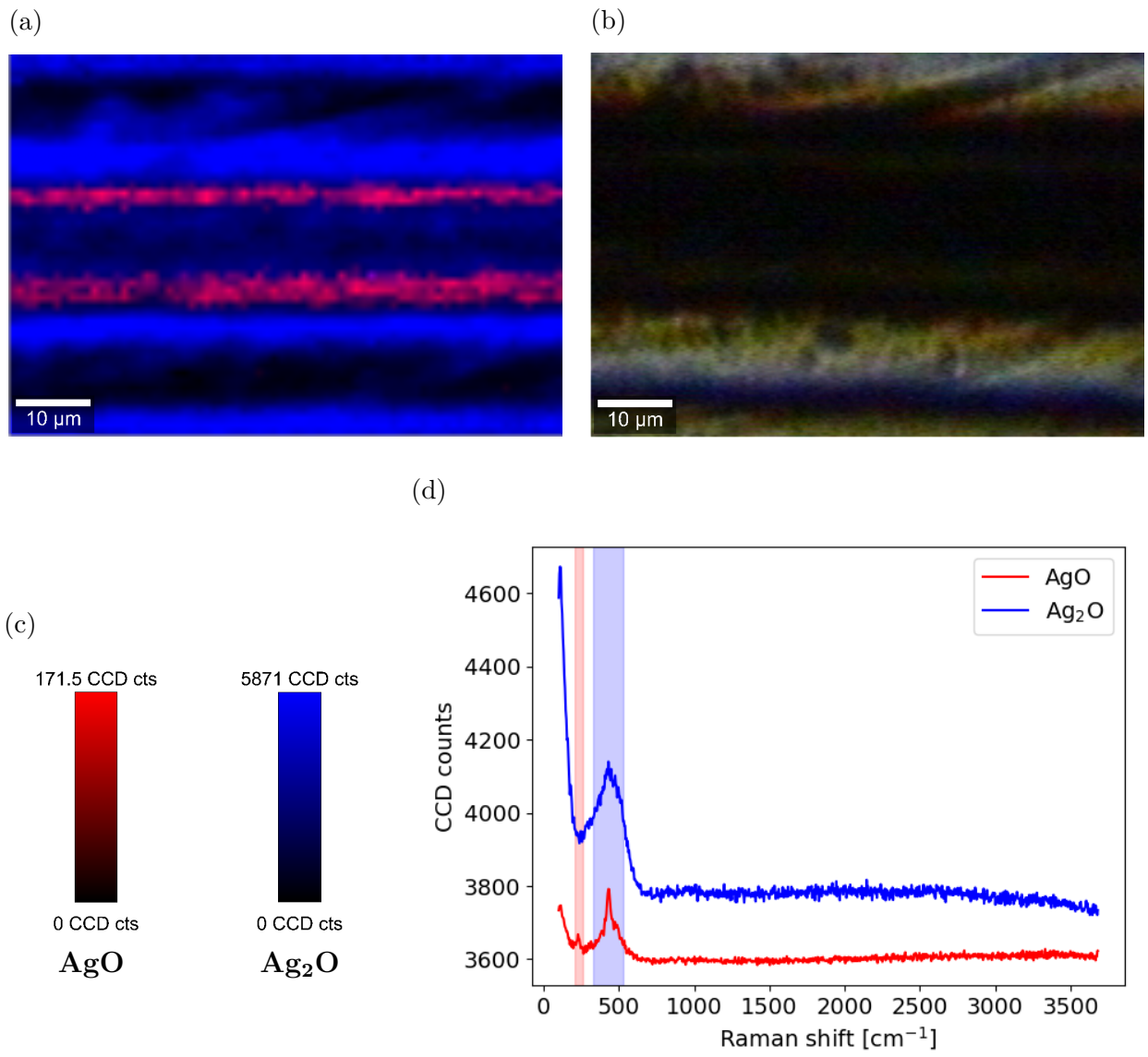

Figure C.1: Raman scan of silver oxides, for 9.83 µJ pulse energy, repetition rate of 10 kHz, stage moving at 0.25 mm/s, giving approximately 80 shots/2 µm (an effective number of pulses of 80). (a) Raman scan, (b) corresponding brightfield image, (c) scale bars for Raman scan, (d) example of Raman spectra found in the scan, along with integrated area shaded in the color respective to the spectra.

Bibliography

1. Walia, J. *et al.* Enhanced hydroxylation and carbon dioxide uptake on nanotextured silver oxide. *Applied Surface Science* **520,** 146300 (2020).

2. Schön, G. *et al.* ESCA studies of Ag, Ag2O and AgO. *Acta Chem. Scand* **27,** 2623 (1973).

3. Bielmann, M. *et al.* AgO investigated by photoelectron spectroscopy: evidence for mixed valence. *Physical Review B* **65,** 235431 (2002).

4. Tudela, D. Silver(II) Oxide or Silver(I,III) Oxide? eng. *Journal of chemical education* **85,** 863–. ISSN: 0021-9584 (2008).

5. Allen, J. P., Scanlon, D. O. & Watson, G. W. Electronic structure of mixed-valence silver oxide AgO from hybrid density-functional theory. eng. *Physical review. B, Condensed matter and materials physics* **81.** ISSN: 1098-0121 (2010).

6. Grzelak, A. *et al.* Persistence of mixed and non-intermediate valence in the high-pressure structure of silver(I,III) oxide, AgO a combined Raman, X-ray diffraction (XRD), and density functional theory (DFT) study. *Inorganic Chemistry* **56,** 5804–5812 (2017).

7. Al-Sarraj, A., Saoud, K. M., Elmel, A., Mansour, S. & Haik, Y. Optoelectronic properties of highly porous silver oxide thin film. eng. *SN applied sciences* **3,** 15–. ISSN: 2523-3963 (2021).

8. Allen, J. P., Scanlon, D. O. & Watson, G. W. Electronic structures of silver oxides. *Physical Review B* **84,** 115141 (2011).

9. Deb, A. & Chatterjee, A. K. The electronic structure and chemical bonding mechanism of silver oxide. *Journal of Physics: Condensed Matter* **10,** 11719 (1998).

10. De Rooij, A. The oxidation of silver by atomic oxygen. *ESA J* **13,** 363–382 (1989).

11. Waterhouse, G., Bowmaker, G. & Metson, J. Oxidation of a polycrystalline silver foil by reaction with ozone. *Applied Surface Science* **183,** 191–204 (2001).

12. Zheludkevich, M. *et al.* Oxidation of silver by atomic oxygen. *Oxidation of metals* **61,** 39–48 (2004).

13. Farhat, E. & Robin-Kandare, S. Phénomènes physiques au cours de la formation de couches minces de AgO. *Thin Solid Films* **23,** 315–322 (1974).

14. Farhat, E., Donnadieu, A. & Robin, J. Cinétique de la croissance de couches minces d'oxyde d'argent AgO. *Thin Solid Films* **29,** 319–324 (1975).

15. Bhan, M. K., Nag, P. K., Miller, G. P. & Gregory, J. C. Chemical and morphological changes on silver surfaces produced by microwave generated atomic oxygen. *Journal of Vacuum Science & Technology A: Vacuum, Surfaces, and Films* **12,** 699–706 (1994).

16. Waterhouse, G., Bowmaker, G. & Metson, J. Interaction of a polycrystalline silver powder with ozone. *Surface and Interface Analysis: An International Journal devoted to the development and application of techniques for the analysis of surfaces, interfaces and thin films* **33,** 401–409 (2002).

17. Pan, J. *et al.* Nano silver oxide (AgO) as a super high charge/discharge rate cathode material for rechargeable alkaline batteries. *Journal of Materials Chemistry* **17,** 4820–4825 (2007).

18. Dallek, S., West, W. & Larrick, B. Decomposition kinetics of AgO cathode material by thermogravimetry. *Journal of the Electrochemical Society* **133,** 2451 (1986).

19. Varkey, A. & Fort, A. Some optical properties of silver peroxide (AgO) and silver oxide (Ag2O) films produced by chemical-bath deposition. *Solar Energy Materials and Solar Cells* **29,** 253–259 (1993).

20. Büchel, D., Tominaga, J., Fukaya, T. & Atoda, N. Spectroscopic Investigation of AgOx Films for Super Resolution Near Field Structure Application. *Journal of the Magnetics Society of Japan* **25,** 240–243 (2001).

21. Büchel, D. *et al.* Sputtered silver oxide layers for surface-enhanced Raman spectroscopy. *Applied Physics Letters* **79,** 620–622 (2001).

22. Kim, J. *et al.* Magneto-optical characteristics enhanced by super resolution near field structure. *Japanese Journal of Applied Physics* **40,** 1634 (2001).

23. Chiu, Y. *et al.* Fabrication and nonlinear optical properties of nanoparticle silver oxide films. *Journal of Applied Physics* **94,** 1996–2001 (2003).

24. Shima, T. & Tominaga, J. Optical transmittance study of silver particles formed by AgO x thermal decomposition. *Journal of Vacuum Science & Technology A: Vacuum, Surfaces, and Films* **21,** 634–637 (2003).

25. Her, Y.-C., Lan, Y.-C., Hsu, W.-C. & Tsai, S.-Y. Effect of constituent phases of reactively sputtered AgOx film on recording and readout mechanisms of super-resolution near-field structure disk. *Journal of Applied Physics* **96,** 1283–1288 (2004).

26. Yoon, C. Photo-structuring of silver-oxide films by using femtosecond laser pulses. *Journal of the Korean Physical Society* **53** (2008).

27. Mirzaeian, M. *et al.* Surface characteristics of silver oxide thin film electrodes for supercapacitor applications. *Colloids and Surfaces A: Physicochemical and Engineering Aspects* **519,** 223–230 (2017).

28. Oje, A. I., Ogwu, A., Mirzaeian, M. & Tsendzughul, N. Electrochemical energy storage of silver and silver oxide thin films in an aqueous NaCl electrolyte. *Journal of Electroanalytical Chemistry* **829,** 59–68 (2018).

29. Oje, A. I., Ogwu, A., Mirzaeian, M., Tsendzughul, N. & Oje, A. Pseudo-capacitance of silver oxide thin film electrodes in ionic liquid for electrochemical energy applications. *Journal of Science: Advanced Materials and Devices* **4,** 213–222 (2019).

30. Asgary, S. & Esmaili, P. Effect of reactive gas flow on structural and optical properties of sputtered silver oxide thin films; Kramers-Kronig method. *Optical and Quantum Electronics* **55,** 118 (2023).

31. Suzuki, R. O., Ogawa, T. & Ono, K. Use of ozone to prepare silver oxides. *Journal of the American Ceramic Society* **82,** 2033–2038 (1999).

32. Farhat, E., Donnadieu, A. & Robin, J. Effet d'un plasma d'oxygène sur les propriétés électriques des couches minces de AgO. *Thin Solid Films* **30,** 83–90 (1975).

33. Oakes, D., Krech, R., Upschulte, B. & Caledonia, G. Oxidation of polycrystalline silver films by hyperthermal oxygen atoms. *Journal of Applied Physics* **77,** 2166–2172 (1995).

34. Dellasega, D. *et al.* Nanostructured Ag4O4 films with enhanced antibacterial activity. *Nanotechnology* **19,** 475602 (2008).

35. Dellasega, D. *et al.* Nanostructured high valence silver oxide produced by pulsed laser deposition. *Applied surface science* **255,** 5248–5251 (2009).

36. Raju, N. R. C., Kumar, K. J. & Subrahmanyam, A. Physical properties of silver oxide thin films by pulsed laser deposition: effect of oxygen pressure during growth. *Journal of Physics D: Applied Physics* **42,** 135411 (2009).

37. Ravi Chandra Raju, N. & Jagadeesh Kumar, K. Photodissociation effects on pulsed laser deposited silver oxide thin films: surface-enhanced resonance Raman scattering. *Journal of Raman Spectroscopy* **42,** 1505–1509 (2011).

38. Mohameed, Q. Q., Hattab, F. A. & Fakhry, M. A. Effect of substrate temperature on structural characteristics of nano silver oxide prepared by pulsed-laser deposition. *Iraqi Journal Of Applied Physics* **11** (2015).

39. Agasti, S., Dewasi, A. & Mitra, A. *Structural and optical properties of pulse laser deposited Ag2O thin films* in *AIP Conference Proceedings* **1953** (2018).

40. Irimiciuc, S. A. *et al.* Insight into the plasma oxidation process during pulsed laser deposition. *Plasma Processes and Polymers* **19,** 2100102 (2022).

41. Waterhouse, G. I., Bowmaker, G. A. & Metson, J. B. The thermal decomposition of silver (I, III) oxide: A combined XRD, FT-IR and Raman spectroscopic study. *Physical Chemistry Chemical Physics* **3,** 3838–3845 (2001).

42. Tissot, P. & Perrenot, B. Thermal decomposition of AgO to Ag2O. *Thermochimica Acta* **85,** 103–106 (1985).

43. Pettinger, B. *et al.* Thermal decomposition of silver oxide monitored by Raman spectroscopy: From AgO units to oxygen atoms chemisorbed on the silver surface. *Angewandte Chemie International Edition in English* **33,** 85–86 (1994).

44. L'vov, B. V. Kinetics and mechanism of thermal decomposition of silver oxide. *Thermochimica Acta* **333,** 13–19 (1999).

45. Gao, X.-Y. *et al.* Study of structure and optical properties of silver oxide films by ellipsometry, XRD and XPS methods. *Thin Solid Films* **455,** 438–442 (2004).

46. Zheludkevich, M. *et al. Studies of the surface oxidation of silver by atomic oxygen* in *Protection of Materials and Structures from Space Environment: ICPMSE-6* (2003), 351–358.

47. Smith, D. F. & Brown, C. Aging in chemically prepared divalent silver oxide electrodes for silver/zinc reserve batteries. *Journal of power sources* **96,** 121–127 (2001).

48. Slager, T., Lindgren, B., Mallmann, A. J. & Greenler, R. G. Infrared spectra of the oxides and carbonates of silver. *The Journal of Physical Chemistry* **76,** 940–943 (1972).

49. Smith, D. F., Graybill, G. R., Grubbs, R. K. & Gucinski, J. A. New developments in very high rate silver oxide electrodes. *Journal of power sources* **65,** 47–52 (1997).

50. Tominaga, J. The application of silver oxide thin films to plasmon photonic devices. *Journal of Physics: Condensed Matter* **15,** R1101 (2003).

51. Fujimaki, M., Awazu, K., Tominaga, J. & Iwanabe, Y. Surface-enhanced Raman scattering from Ag nanoparticles formed by visible laser irradiation of thermally annealed AgOx thin films. *Journal of applied physics* **100** (2006).

52. Naghilou, A., Armbruster, O. & Kautek, W. Laser-induced non-thermal processes. *Handbook of Laser Micro-and Nano-Engineering,* 1–23 (2020).

53. Balling, P. Laser coupling and relaxation of the absorbed energy: Metals, semiconductors, and dielectrics. *Handbook of Laser Micro-and Nano-Engineering,* 1–58 (2020).

54. Zhong, M. & Long, J. Laser Surface Structuring of Metals and Functionalization. *Handbook of Laser Micro-and Nano-Engineering,* 1–38 (2020).

55. Shugaev, M. V. *et al.* in *Handbook of Laser Micro-and Nano-Engineering* 83–163 (Springer, 2021).

56. Byskov-Nielsen, J., Savolainen, J.-M., Christensen, M. S. & Balling, P. Ultra-short pulse laser ablation of metals: threshold fluence, incubation coefficient and ablation rates. *Applied Physics A* **101,** 97–101 (2010).

57. Chichkov, B. N., Momma, C., Nolte, S., Von Alvensleben, F. & Tünnermann, A. Femtosecond, picosecond and nanosecond laser ablation of solids. *Applied physics A* **63,** 109–115 (1996).

58. Bonse, J., Kirner, S. V. & Krüger, J. Laser-induced periodic surface structures (LIPSS). *Handbook of laser micro-and nano-engineering,* 1–59 (2020).

59. Vorobyev, A. & Guo, C. Nanochemical effects in femtosecond laser ablation of metals. *Applied Physics Letters* **102** (2013).

60. Nánai, L., Vajtai, R. & George, T. F. Laser-induced oxidation of metals: state of the art. *Thin Solid Films* **298,** 160–164 (1997).

61. Chen, X., Xiong, S., Sha, Z. & Liu, Z. The interaction of ambient background gas with a plume formed in pulsed laser deposition. *Applied surface science* **115,** 279–284 (1997).

62. Camposeo, A., Cervelli, F., Fuso, F., Allegrini, M. & Arimondo, E. Mechanisms for O 2 dissociation during pulsed-laser ablation and deposition. *Applied Physics Letters* **78,** 2402–2404 (2001).

63. Stricker, J. & Parker, J. Experimental investigation of electrical breakdown in nitrogen and oxygen induced by focused laser radiation at 1.064 μ. *Journal of Applied Physics* **53,** 851–855 (1982).

64. Stricker, J. & Parker, J. Ozone formation behind pulsed-laser-generated blast waves in oxygen. *Journal of applied physics* **56,** 3151–3162 (1984).

65. Ngo, P. D. in *Failure analysis of integrated circuits: Tools and techniques* 205–215 (Springer, 1999).

66. Chastain, J. & King Jr, R. C. Handbook of X-ray photoelectron spectroscopy. *Perkin-Elmer Corporation* **40,** 221 (1992).

67. Bock, F., Christensen, T., Rivers, S., Doucette, L. & Lad, R. Growth and structure of silver and silver oxide thin films on sapphire. *Thin Solid Films* **468,** 57–64 (2004).

68. Gaffney, J. S., Marley, N. A. & Jones, D. E. Fourier transform infrared (FTIR) spectroscopy. *Characterization of materials,* 1–33 (2002).

69. Orlando, A. *et al.* A comprehensive review on Raman spectroscopy applications. *Chemosensors* **9,** 262 (2021).

70. Jones, R. R., Hooper, D. C., Zhang, L., Wolverson, D. & Valev, V. K. Raman techniques: fundamentals and frontiers. *Nanoscale research letters* **14,** 1–34 (2019).

71. Rostron, P., Gaber, S. & Gaber, D. Raman spectroscopy, review. *laser* **21** (2016).

72. Temperini, M. L., Lacconi, G. I. & Sala, O. Raman spectroscopy investigation of the silver oxide/silver electrode: influence of experimental conditions. *Journal of electroanalytical chemistry and interfacial electrochemistry* **227,** 21–28 (1987).

73. Martina, I., Wiesinger, R., Jembrih-Simbürger, D. & Schreiner, M. Micro-Raman characterisation of silver corrosion products: instrumental set up and reference database. *E-Preserv Sci* **9,** 1–8 (2012).

74. Roberts, D., Du Plessis, A. & Botha, L. Femtosecond laser ablation of silver foil with single and double pulses. *Applied Surface Science* **256,** 1784–1792 (2010).

75. Dai, Y. *et al.* Femtosecond laser nanostructuring of silver film. *Applied Physics A* **106,** 567–574 (2012).

76. Danilov, P. A. *et al.* Redistribution of a material at femtosecond laser ablation of a thin silver film. *JETP letters* **104,** 759–765 (2016).

77. Smirnov, N. *et al.* Femtosecond laser ablation of a thin silver film in air and water. *Optical and Quantum Electronics* **52,** 1–8 (2020).

78. Danilov, P. *et al.* Femtosecond laser ablation of thin silver films in air and water under tight focusing. *Optical Materials Express* **10,** 2717–2722 (2020).

79. Liu, J.-M. Simple technique for measurements of pulsed Gaussian-beam spot sizes. *Optics letters* **7,** 196–198 (1982).

80. Nivas, J. J. & Amoruso, S. Generation of supra-wavelength grooves in femtosecond laser surface structuring of silicon. *Nanomaterials* **11,** 174 (2021).

81. Sanders, C. E., Verreault, D., Frankel, G. & Allen, H. C. The role of sulfur in the atmospheric corrosion of silver. *Journal of the Electrochemical Society* **162,** C630 (2015).

82. Graedel, T. Corrosion mechanisms for silver exposed to the atmosphere. *Journal of the Electrochemical Society* **139,** 1963 (1992).

83. McMahon, M., Lopez, R., Meyer, H., Feldman, L. & Haglund, R. Rapid tarnishing of silver nanoparticles in ambient laboratory air. *Applied Physics B* **80,** 915–921 (2005).